

UCGE Reports
Number 20281

Department of Geomatics Engineering

**Object-based Integration of Photogrammetric and
LiDAR Data for Accurate Reconstruction and
Visualization of Building Models**

(URL: <http://www.geomatics.ucalgary.ca/research/publications>)

by

Changjae Kim

December 2008



UNIVERSITY OF CALGARY

Object-based Integration of Photogrammetric and LiDAR Data for Accurate
Reconstruction and Visualization of Building Models

by

Changjae Kim

A THESIS

SUBMITTED TO THE FACULTY OF GRADUATE STUDIES
IN PARTIAL FULFILMENT OF THE REQUIREMENTS FOR
THE DEGREE OF DOCTOR OF PHILOSOPHY

Department of Geomatics Engineering

CALGARY, ALBERTA

DECEMBER, 2008

© Changjae Kim 2008

Abstract

The complementary characteristics of photogrammetric and Light Detection And Ranging (LiDAR) data can lead to better surface description through their integration, when compared to that derived from either system alone, by supplying both accurate 3D positional information and descriptive information. This research is concerned with the integration of photogrammetric and LiDAR data to achieve a more complete surface description through the proposed true orthophoto generation, building hypothesis and primitive generation, and Digital Building Model (DBM) generation procedures. First, two alternative true orthophoto generation methodologies are proposed to overcome the limitations of existing methodologies. Even though improved true orthophoto generation methodologies are developed, it is hard to avoid the decrease in the quality of the true orthophoto products around breaklines, due to the irregular and sparse nature of LiDAR data. To improve the accuracy of the positional and descriptive information around breaklines, an accurate DBM generation procedure is needed. The building detection process is carried out first in order to generate building hypotheses and primitives from the LiDAR data alone. Then, the building reconstruction process is carried out using the derived building primitives. In order to produce precise boundary segments, the matching ambiguity problem is resolved by incorporating LiDAR data into the matching process, as a constraint. Then, colour information near the line segments derived through the matching process is utilized to find precise boundary segments. In addition, boundary segments in the occluded areas are reconstructed by hierarchically projecting the constructed segments of higher building primitives onto lower, neighbouring ones when these primitives share common vertical walls. All the derived boundary segments

contribute to DBM generation. At last, the accurately generated DBMs are used to produce improved true orthophotos and 3D visualizations. In summary, this research provides a new framework for the accurate reconstruction and visualization of urban environments, and the accuracy of the products is ensured by taking advantages of the synergic properties arising from the integration of photogrammetric and LiDAR data.

Acknowledgements

This thesis would not be possible without the support of many people whom I owe a great deal of gratitude for their help and support throughout my research. First and foremost, I would like to express my sincere appreciation to my supervisor, Dr. Ayman Habib, for his support and guidance throughout the span of my graduate studies. I owe him lots of my knowledge in photogrammetry, LiDAR, and more than that. He taught me the scientific way of thinking and how to resolve problems encountered with his creativeness, wealth of knowledge, and great patience.

I also wish to express my deep appreciation to Dr. Naser El-Sheimy, Dr. Derek Lichti, Dr. Steve Liang, Dr. John Yackel, and Dr. Jie Shan for carefully reviewing and providing comments concerning various aspects of this research.

Acknowledgements must also be given to the University of Calgary IT Department for providing datasets as well as the Korean Electronics and Telecommunications Research Institute (ETRI) and GEOmatics for Informaed DEcisions (GEOIDE – SII 43 and IV-17) for providing funding. Also, I would like to thank the American Society of Photogrammetry and Remote Sensing (ASPRS) and North West Group for providing awards and scholarships that helped me during my PhD study. Of course, I am also indebted to my colleagues at the Digital Photogrammetry Research Group and beyond. I would like to thank Ki-in Bang, Ruifang Zhai, David Chang, Anna Jarvis, Juliano and Ana Kersting, Jennifer Lay, Dcotors Simon Park, Eui Myoung Kim, Miao Wang, Edson Mitishita, and Michel Morgan for the help and fruitful discussions we had together.

Dedication

To God

And to my beloved parents

Eungsun Kim and Gilnam Ryu

Table of Contents

Abstract.....	ii
Acknowledgements.....	iv
Dedication.....	v
Table of Contents.....	vi
List of Tables.....	viii
List of Figures and Illustrations.....	ix
List of Abbreviations.....	xvii
CHAPTER 1 : INTRODUCTION.....	1
1.1 Motivation.....	1
1.2 Problem Statement.....	3
1.3 Research Objectives and Scope.....	7
1.4 Structure of the Dissertation.....	13
CHAPTER 2 : LITERATURE REVIEW.....	15
2.1 Introduction.....	15
2.2 Relating Spectral and Positional Information.....	15
2.3 Building Model Generation.....	29
2.3.1 Monocular imagery.....	31
2.3.2 Stereo and multiple imagery.....	32
2.3.3 LiDAR.....	34
2.3.4 Data integration.....	38
2.4 Summary.....	40
CHAPTER 3 : RELATING IMAGE SPECTRAL AND OBJECT POSITIONAL INFORMATION.....	43
3.1 Introduction.....	43
3.2 Quality Assurance and Control of Photogrammetric and LiDAR Data.....	43
3.3 Co-registration.....	45
3.3.1 Point-based incorporation of linear features.....	48
3.3.2 Point-based incorporation of areal features.....	51
3.4 Rectification and Visibility Analysis.....	55
3.5 Summary.....	74
CHAPTER 4 : BUILDING HYPOTHESIS AND PRIMITIVE GENERATION.....	75
4.1 Introduction.....	75
4.2 Terrain/Off-terrain Point Classification.....	76
4.2.1 DSM generation.....	78
4.2.2 Occlusion-based off-terrain point detection in the DSM.....	79
4.2.3 Statistical filtering for the refinement of the classified points.....	88
4.2.4 Classifying the original LiDAR point cloud.....	90
4.3 Building Hypothesis Generation.....	93
4.4 Building Primitive Generation.....	98
4.4.1 Segmentation.....	100
4.4.2 Initial boundary generation for building primitives.....	113

4.5 Summary	118
CHAPTER 5 : BUILDING RECONSTRUCTION AND VISUALIZATIONS	120
5.1 Introduction.....	120
5.2 Building Reconstruction	121
5.2.1 Precise boundary segment generation through the intersection of neighbouring planar patches	125
5.2.2 Precise boundary segment derivation through the integration of LiDAR and photogrammetric data.....	129
5.2.3 Precise boundary segment derivation through projection and regularization	150
5.2.4 Closed-polygon and 3D building model generation.....	153
5.3 DSM Enhancement and Visualizations	158
5.4 Summary	163
CHAPTER 6 : EXPERIMENTS AND RESULTS.....	165
6.1 Introduction.....	165
6.2 Dataset Description.....	166
6.3 Co-registration	167
6.4 Building Hypothesis and Primitive Generation	170
6.5 Building Reconstruction and Visualizations.....	177
6.6 Quantitative Analysis.....	192
6.7 Summary	196
CHAPTER 7 : CONCLUSIONS AND RECOMMENDATIONS FOR FUTURE WORK	199
7.1 Conclusions.....	199
7.2 Recommendations for Future Work	208
REFERENCES	211

List of Tables

Table 6.1 Estimated EOPs for the left and right images	169
Table 6.2 Variance-correlation matrix for the left image	169
Table 6.3 Variance-correlation matrix for the right image	169
Table 6.4 Descriptions, values, and justifications for the thresholds used for terrain and off-terrain point classification	172
Table 6.5 Descriptions, values, and justifications for the thresholds used for building hypothesis generation.....	173
Table 6.6 Descriptions, values, and justifications for the thresholds used for the generation of building primitives and their initial boundaries.....	176
Table 6.7 Descriptions, values, and justifications for the thresholds used for precise boundary generation through the intersection of neighbouring planar patches	179
Table 6.8 Descriptions, values, and justifications for the thresholds used for precise boundary generation through the processes of integration, projection, and regularization	180
Table 6.9 Statistics derived from the comparison of two manually generated sets of DBM vertices (second column) as well as the comparison of automatically and manually generated DBM vertices (third column)	195

List of Figures and Illustrations

Figure 1.1: The proposed framework for better surface description.	9
Figure 2.1: Principle of ortho-rectification for orthophoto generation.	16
Figure 2.2: Double mapped areas where sudden relief causes duplication of the projected grey values onto the orthophoto plane (datum).	17
Figure 2.3: Perspective image (a) and the corresponding orthophoto (b) with double mapped areas enclosed by solid black lines.	18
Figure 2.4: Principle of true orthophoto generation using the Z-buffer method.	21
Figure 2.5: Simulated data with nine buildings over a flat terrain.	22
Figure 2.6: False occlusions are reported whenever the DSM cell size is smaller than the GSD of the imaging sensor.	23
Figure 2.7: Visibility map corresponding to the DSM in Figure 2.5 where the DSM cell size is chosen to be smaller than GSD of the imaging sensor (black grids between buildings indicate false occlusions).	24
Figure 2.8: Optimal sampling of the DSM at the terrain level and tall vertical structures might lead to false visibility in occluded areas.	25
Figure 2.9: Detected occlusion areas with optimal sampling of the DSM at the terrain level for the DSM in Figure 2.5 (white lines within the detected occlusions indicate false visibility).	25
Figure 2.10: M-portion problem leads to false visibility (a), which can be minimized by the introduction of pseudo groundels (b).	26
Figure 2.11: The M-portion problem leads to false visibility as indicated by the dashed triangles in (a) and can be mitigated by the introduction of pseudo groundels (b).	27
Figure 2.12: LiDAR DSM corresponding to the area in Figure 2.3(a), true orthophoto generated using the Z-buffer method (b) with a closer look at the building within the white circle (c).	28
Figure 2.13: Sources of data used for DBM generation.	31
Figure 3.1: Perspective image (a), and orthoimage using the geo-referencing parameters using GCPs (b), LiDAR patches (c), and LiDAR lines (d), as the source of control (Habib et al., 2008c).	46

Figure 3.2: LiDAR point cloud extracted for the area of interest selection (a), segmented planar patches (b), and linear features extracted by intersecting two neighbouring planar patches (c) (Habib et al., 2008c).....	48
Figure 3.3: Representation of image and object space lines for the point-based incorporation of linear features (Habib et al., 2008c).....	49
Figure 3.4: Image and line coordinate systems.....	50
Figure 3.5: Representation of corresponding patches in the image and object spaces (Habib et al., 2008c).....	52
Figure 3.6: Object and plane coordinate systems.	53
Figure 3.7: Perspective image (a) and corresponding orthophoto with double mapped areas around buildings (b).....	55
Figure 3.8: Using the off-nadir angle to the line of sight as a means of detecting occlusions.....	58
Figure 3.9: Conceptual basis of the radial sweep method of occlusion detection.	59
Figure 3.10: DSM partitioning for the adaptive radial sweep method (the azimuth increment value decreases as one moves away from the nadir point).	60
Figure 3.11: The R- θ array that corresponds to the partitioned DSM in Figure 3.10.....	61
Figure 3.12: Conceptual procedural flow of the adaptive radial sweep method of occlusion detection.....	63
Figure 3.13: Conceptual procedural flow of the spiral sweep method of occlusion detection.....	64
Figure 3.14: Visibility maps created using Z-buffer method (a) and angle-based approach (b) when the DSM cell size is less than the GSD of the imaging sensor. .	65
Figure 3.15: Visibility maps created using Z-buffer method (a) and angle-based approach (b) when the DSM size is chosen to be equivalent to the GSD at the terrain surface.....	66
Figure 3.16: Visibility maps created using Z-buffer method (a) and angle-based approach (b) when a DSM includes narrow vertical structures.....	67
Figure 3.17: Detected occlusions from the adaptive radial sweep (a) and spiral sweep (b) methods using the simulated DSM in Figure 2.5.....	68
Figure 3.18: A true orthophoto generated using adaptive radial sweep method (a) and a true orthophoto generation using Z-buffer method (b).	69

Figure 3.19: Enlarged areas in the true orthophotos created using adaptive radial sweep method (a) and using Z-buffer method (b).	70
Figure 3.20: A true orthophoto (based on the adaptive radial sweep method) after filling the occlusions using overlapping images (a) and 3D perspective view after draping the generated true orthophoto on top of the DSM (b).	71
Figure 3.21: Jagged building boundaries due to the incompleteness of the DSM.....	73
Figure 3.22: Low quality of the produced true orthophoto around small features (e.g., cars, sculptures, and trees) due to the incompleteness of the DSM.	73
Figure 4.1: Flow chart for the terrain/off-terrain classification of the LiDAR points.	78
Figure 4.2: Occluding point detection using multiple projection centers (PCs).....	80
Figure 4.3: The impact of the vertical (a) and planimetric (b) location of the synthesized projection center on the extent of detected off-terrain objects.....	83
Figure 4.4: The different impact of the synthesized projection center on the close and distant buildings.	84
Figure 4.5: Optimal number of projection centers for two DSM cells (A and B).	85
Figure 4.6: Checking all possible occluding directions for the DSM cells one profile at a time.	86
Figure 4.7: Chain of synthesized projection centers for a given DSM.....	86
Figure 4.8: Simulated DSM (a), hypothesized off-terrain points (in white) before statistical filtering (b), and detected off-terrain points after statistical filtering (c)..	87
Figure 4.9: A dataset with high frequency components in the terrain surface (e.g., tunnels): resampled DSM (a), identified occluding points (b), and resulting off-terrain points after statistical filtering (c).....	92
Figure 4.10: A dataset with complex and connected structures: aerial photo over the area of interest (a), LiDAR data that covers the same area (colors are assigned according to point elevations) (b), and classified terrain and off-terrain points (in blue and red, respectively).	93
Figure 4.11: Flow chart of building hypothesis generation using off-terrain points.	94
Figure 4.12: The first fitted plane for a spherical neighbourhood centered at an off-terrain point in question (a), and the final fitted plane derived through the iterative procedure using the inverses of the normal distances as weights (b).	95

Figure 4.13: Majority of the points are within the plane buffer in case that the points belong to planar surface (a) and a few points are within the buffer in case that the points belong to rough surface (b) (side view).	96
Figure 4.14: An example of building hypotheses generated through the proposed procedure.....	97
Figure 4.15: LiDAR points with the closeness less than a proximity threshold (a) and points on a structure formed by connected planes (b).	98
Figure 4.16: Flow chart of building primitive generation.....	99
Figure 4.17: Different neighbourhood definition methods (side view): TIN (a), spherical (b), and adaptive cylinder (c).....	102
Figure 4.18: Vector defined from the origin to the computed plane for a given point, using its neighbouring points.....	103
Figure 4.19: Situation that one origin is located at an equal distance from the planes and the other origin is not (a) and the recorded votes in two-dimensional accumulator array (b).	106
Figure 4.20: Ambiguity from two origins (side view) (a), and the positioning of two origins that minimizes the possibility of such ambiguity (side view) (b).....	107
Figure 4.21: Flow chart of the clustering procedure.....	109
Figure 4.22: Aggregation of points with similar attributes: the digital image (a), the Digital Surface Models over the area of interest (b), the accumulator array (c), and the segmented patches (d).	110
Figure 4.23: Steps of the modified convex hull algorithm (Sampath and Shan, 2007)..	114
Figure 4.24: Boundary detection: clustered points from attribute space (a), and detected boundary (b).	114
Figure 4.25: Neighbourhood analysis via boundary detection: multiple coplanar patches detected from the attribute space (a), and patches separated through boundary detection (b).	115
Figure 4.26: Building primitives (a), and boundaries of the building primitives (b).....	116
Figure 4.27: Projected initial boundary onto the imagery for a given building primitive.....	117
Figure 5.1: Flow chart of the building reconstruction procedure.	121

Figure 5.2: A ridge line on a gable roof (a) and a building primitive hidden by another higher one in left (b) and right (c) images, in the areas enclosed by the red dashed ellipses.	124
Figure 5.3: Portions of a building primitive, which are hidden by a higher one either in left (a) and right (b) images or in both of the images, in the areas enclosed by the red dashed ellipses.	124
Figure 5.4: Locations of building primitives (a) and the relevant 3D adjacency table (b).	126
Figure 5.5: Segmented points in the neighbouring primitives and their projections onto the intersection line (top view).	127
Figure 5.6: Boundary segment generation through the detection of significant gaps between adjacent projected points.	128
Figure 5.7: Boundary segment generated through the intersection of two neighbouring primitives (a) and the segment projected onto the corresponding image (b).	128
Figure 5.8: Flow chart of the precise boundary segment generation method based on the integration of LiDAR and photogrammetric data.	131
Figure 5.9: Concept of warped imagery.	133
Figure 5.10: Produced left (a) and right (b) warped images and a similarity map (c) derived from these images.	134
Figure 5.11: Visibility map along one profile (a), and top view of the visibility map (b).	135
Figure 5.12: Straight line segments detected in the left (a) and right (b) warped images.	137
Figure 5.13: Matching straight line segments in warped images using angle and normal distance constraints (a) and the presence of overlap between straight line segments, and 3D matched lines (b).	139
Figure 5.14: Matched 3D lines for the straight line segments in Figure 5.12(a) and (b).	140
Figure 5.15: A matched 3D line that follows the trend of the initial boundary of the building primitive (a), and one that does not (b).	141
Figure 5.16: Filtered matched 3D lines which are obtained after the filtering process is applied to the matched 3D lines in Figure 5.14.	142
Figure 5.17: Establishing reference lines (a) and defining group members (b).	143
Figure 5.18: Established reference lines (a) and grouped matched 3D lines (b).	144

Figure 5.19: The members of an established group on the left (a) and right (b) warped images.	145
Figure 5.20: Similarity measures for different locations along the LiDAR plane.....	146
Figure 5.21: Configuration of the regions around the matched 3D line segments in one group (a), regions on either side of the line segments L1 (b), L2 (c), and L3 (d).....	148
Figure 5.22: Established precise boundary segments for the groups in Figure 5.18(b)..	149
Figure 5.23: Projection of the constructed boundary segments of the higher/neighbouring building primitive onto the lower primitive under investigation.....	151
Figure 5.24: Constructed boundary segments of the higher and neighbouring building primitive (a) and precise boundary segments for the current primitive after projection process (b).....	152
Figure 5.25: Constructed boundary segments after regularization process.	153
Figure 5.26: Establishing the proper sequence for the identified boundary segments. ..	154
Figure 5.27: Closed-polygon generated from the established precise boundary segments in Figure 5.22.	154
Figure 5.28: Closed-polygons for three building primitives at different elevations (a); boundary segments projected onto a horizontal plane (b); and co-aligned boundary segments (c).	156
Figure 5.29: A generated DBM wire frame (using the polygon in Figure 5.27) (a) is imported to Google Earth (b).....	157
Figure 5.30: An example of closed-polygon with erroneous segments.....	158
Figure 5.31: A true orthophoto created using the original DSM (a) and the enlarged area enclosed by red box (b).	159
Figure 5.32: A true orthophoto created using a DSM obtained by adding the DBM to the original DSM (a) and the enlarged area enclosed by red box (b).	160
Figure 5.33: A true orthophoto created using a DSM obtained by adding the DBM to the DTM (a) and the enlarged area enclosed by red box (b).....	160
Figure 5.34: Small features in the true orthophotos created using the original DSM (a) and using a DSM obtained by adding the DBM to the DTM (b).	161
Figure 5.35: A 3D visualizations produced using the original DSM (a) and a DSM obtained by adding the DBM to the DTM (b).	162

Figure 6.1: Nine overlapping aerial photos overlaid on the LiDAR data.....	167
Figure 6.2: Locations of the control lines in the LiDAR dataset.....	168
Figure 6.3: Aerial photo over the area of interest (a), and LiDAR points over the same area (b).	170
Figure 6.4: Classified off-terrain points in red (a), and generated building hypotheses (b).....	171
Figure 6.5: Clustered building primitives (a), and the initial boundaries of the building primitives (b).....	174
Figure 6.6: Examples illustrating the deviation and closeness between the initial boundary of the building primitives and the actual building boundaries.....	175
Figure 6.7: An example of a simple building primitive: initial boundary projected onto the left (a) and right (b) warped images; refined boundary projected onto the left (c) and right (d) warped images.....	183
Figure 6.8: An example of a building primitive with low complexity: derived line segments for the higher and neighbouring building primitive (a); initial boundary projected onto the left (b) and right (c) warped images; and refined boundary projected onto the left (d) and right (e) warped images.....	184
Figure 6.9: An example of a building primitive with medium complexity: derived line segments for the higher and neighbouring building primitives (a); initial boundary projected onto the left (b) and right (c) warped images; and refined boundary projected onto the left (d) and right (e) warped images.....	185
Figure 6.10: An example of a building primitive with high complexity: derived line segments for the higher and neighbouring building primitives (a); initial boundary projected onto the left (b) and right (c) warped images; and refined boundary projected onto the left (d) and right (e) warped images.....	186
Figure 6.11: Initial DBM (in KML format) produced through the automated building reconstruction process.....	187
Figure 6.12: Erroneous boundary segments produced through the refinement process due to shadow (a) and a weak similarity transition in the left (b) and right (c) warped images.	188
Figure 6.13: Final DBM (in KML format) after manual editing of the initial DBM, which is produced through the automated process.	189
Figure 6.14: The enhanced DSM produced by combining the DTM and the final DBM.	190

Figure 6.15: A true orthophoto produced using the enhanced DSM and the imagery involved.....	190
Figure 6.16: A 3D visualization produced by draping the true orthophoto over the enhanced DSM.....	191
Figure 6.17: Enlarged areas from true orthophotos before (a & c) and after DSM enhancement (b & d).....	191
Figure 6.18: Enlarged areas from 3D visualizations before (a & c) and after DSM enhancement (b & d).....	192
Figure 6.19: A building with protruding fences with manually selected corner points..	195
Figure 7.1: The concept of roof region detection based on region growing using colour segmentation.	210
Figure 7.2: Samples of the street furniture available in ArcGIS.....	210

List of Abbreviations

2D	Two Dimensional
3D	Three Dimensional
CSG	Constructive Solid Geometry
DBM	Digital Building Model
DEM	Digital Elevation Model
DSM	Digital Surface Model
DTM	Digital Terrain Model
EOP	Exterior Orientation Parameters
GCP	Ground Control Point
GIS	Geographic Information System
GPS	Global Positioning System
GSD	Ground Sampling Distance
INS	Inertial Navigation System
IOP	Interior Orientation Parameters
LiDAR	Light Detection And Ranging
RGB	Red Green Blue
RMSE	Root Mean Squared Error
TIN	Triangulated Irregular Network
UAV	Unmanned Aerial Vehicle

Chapter 1 : Introduction

1.1 Motivation

The United Nations predicts that the number of dwellers in urban areas will rise to almost 5 billion inhabitants by 2030 in the report entitled ‘State of the World Cities 2006/7’. Such a population will constitute roughly 62% of the global population at that time. To successfully control social and environmental situations that might arise from this rapid urbanization, decision makers in various fields must have access to accurate and up-to-date geo-spatial information in a timely manner and at a reasonable cost. It has been, hence, recognized that the research and academic communities should develop practical and accurate tools for assisting these decision makers in exploiting the influx of geo-spatial datasets from multi-sensory systems. Basically, human understanding of urban environments can be fully assisted through the use of both spectral and positional information. Hence, the tools must be designed based on a system that uses both types of information. Well-known tools, such as Google Earth, NASA’s World Wind, and Microsoft’s Virtual Earth, are now available through the internet, allowing anyone to access satellite imagery and aerial photos covering most of the world, while providing positional information as well. People are using these applications to find directions to, and rough locations of, their destinations. It is, however, important to note that although the 3D visualizations available using the applications mentioned above may seem realistic, their level of accuracy is not sufficient for urban planning, urban management, and other applications, such as sidewalk construction, enforcement of right to light, visibility analysis for military operations, and line of sight analysis for

telecommunication. Moreover, the accurate geo-spatial information can be used as control information for the geo-referencing of images from various data sources (e.g., for a camera mounted on a Unmanned Aerial Vehicle (UAV), cell phone camera, surveillance camera, etc). For this reason, there has been an increasing need to develop a new system to be able to provide and manipulate accurate and realistic geo-spatial information in an automatic manner, while reducing the incurred costs. In other words, a system that is able to provide a better surface description (or reconstruction) with accurate positional and spectral information needs to be developed at a reasonable cost.

Traditionally, photogrammetry has been used as the primary approach for deriving geo-spatial information through the use of multiple analog and digital images. The 3D information derived from photogrammetric measurements consists of accurate metric and rich descriptive object information (Mikhail et al., 2001). The critical step in surface reconstruction in photogrammetry is the identification of the same features in multiple images, a process referred to as the matching problem. The photogrammetric and computer vision communities have been making great efforts toward the automation of this procedure. However, it still remains a difficult and unreliable task, especially when dealing with large scale images over urban areas (Schenk and Csatho, 2002).

Since it was introduced in the 1980s, Light Detection And Ranging (LiDAR) technology has emerged as a promising method for acquiring digital elevation data effectively and accurately. Since LiDAR technology is fully automated for generating digital elevation data, many researchers have paid attention to the technology and its applications (Ackermann, 1999). However, LiDAR data has a couple of disadvantages in terms of surface description. Basically, the system scans over surfaces and acquires

sample points reflected from these surfaces. Since these points are irregularly spaced, they do not divulge accurate information regarding breaklines such as building boundaries. Moreover, LiDAR data lacks the descriptive information, especially the spectral information that is essential to describe surfaces more completely.

Although a variety of research has been conducted using these data sources, there are still many unsolved problems with the procedures used to achieve better surface descriptions. Hence, this research aims to introduce a new framework for generating accurate and realistic surface information for urban environments by using both photogrammetric and LiDAR datasets. The proposed procedures within this framework will overcome the problems mentioned above and provide accurate and robust solutions. In the remaining parts of this chapter, the problem statement, research objectives and scope, and structure of the dissertation will be discussed.

1.2 Problem Statement

Recall that spectral and positional information are the main components of surface description from the point of view of the photogrammetric community. It is known that there are many challenges in the journey to achieve better surface description using spectral and positional information from multi-sensory datasets in an automatic manner. Although a great deal of academic research has been conducted, there are still many unsolved problems. Hence, some of the fundamental issues and critical problems in the surface description process are addressed and categorized according to the following main subjects:

- Limitations of surface description using photogrammetric data: Basically, photogrammetric procedures can provide both positional and spectral surface information. These characteristics of photogrammetry provide great benefits in terms of surface description. For this reason, diverse research has been conducted on surface reconstruction using a monocular image, stereo images, and multiple images. Since building is one of the main components in urban environment, most of the research has focused on building reconstruction. There are still several problems that are critical and as yet unsolved. The first one is the limitations of the methods using a monocular image. Usually these methods employ some assumptions regarding the internal building characteristics (e.g., orthogonality, parallelism, and symmetry). These assumptions are not valid for complex buildings. The second is the automated identification of conjugate features in stereo or multiple images. Because of the geometric distortions that arise due to the nature of the perspective projection, this is still a difficult and unreliable task. The third problem is that occlusions around complex and connected buildings make it impossible to detect conjugate features in stereo or multiple images. The incorporation of multiple images with high overlap and sidelap has been proposed as a means of overcoming the occlusion problem (Wang et al., 2008). However, this method increases the costs of data acquisition and processing.
- Limitations of surface description using LiDAR data: The main benefit of using LiDAR data is the high degree of automation it provides for deriving surface elevations. For this reason, LiDAR data has been widely utilized in automated surface

reconstruction procedures. However, the LiDAR system provides weak information along breaklines due to the irregular and sparse nature of the data acquisition process. To resolve this problem, various research studies have been conducted using high density LiDAR data (Vosselman, 1999; Rottensteiner and Briese, 2002). The use of high density data, however, increases data acquisition and processing costs. Moreover, LiDAR systems usually do not provide spectral information, which is essential for surface description. Even though the data includes intensity information, this does not generate sufficient surface description.

- Synergy between photogrammetric and LiDAR data: Photogrammetry and LiDAR have their own advantages and disadvantages in terms of surface description. Photogrammetric data has higher planimetric accuracy than vertical accuracy. Conversely, LiDAR data has better vertical accuracy than planimetric accuracy. Photogrammetric data provides dense positional information along object space breaklines, whereas the information provided by LiDAR data is weak in this respect. Conversely, photogrammetric data contains almost no positional information along homogeneous surfaces, but LiDAR data provides dense information for such surfaces (Baltsavias 1999). The complementary nature of such characteristics gives enough reason for the integration of the two types of data. Such integration would enable the utilization of synergistic properties and lead to accurate and realistic surface descriptions, while overcoming the limitations of each dataset type. To fully utilize the synergistic properties, both datasets should be registered with respect to a common reference frame through a co-registration process. Afterwards, the

procedures to correctly relate spectral and positional surface information derived from these datasets can be performed. Since the positional information is derived from LiDAR points, there is a lack of representation of features, especially, breaklines (e.g., building boundaries in urban environments) due to the irregular and sparse nature of LiDAR data. Hence, the surface models should be enhanced by proper manipulation of the original LiDAR points. More detailed explanations of these problems are addressed as follows.

- Co-registration: The synergistic characteristics of different types of datasets can be fully utilized only after both datasets are co-registered relative to a common reference frame (Habib and Schenk 1999, Chen et al. 2004). As long as the one-to-one point correspondence between photogrammetric and LiDAR data remains almost impossible, a well-designed co-registration procedure considering registration primitives, transformation functions, and similarity measures should be incorporated into the framework.
- Relating spectral and positional information: Once the co-registration has been accomplished, the proper procedures to relate the spectral and positional surface information can be carried out. Differential rectification has traditionally been used to relate image spectral and LiDAR positional information. However, for large scale imagery over urban areas, differential rectification produces serious artefacts, in the form of double mapped areas, at any object space locations with sudden variations in relief (e.g., in the vicinity

of buildings) (Skarlatos, 1999). This phenomenon can be avoided by incorporating visibility analysis into the differential rectification procedures. Effective visibility analysis techniques should be introduced into the framework.

- Enhancement of surface models: Since LiDAR data consists of points irregularly sampled over surfaces, the LiDAR points might not sufficiently represent breaklines. The insufficient representation of these features leads to the degradation of the surface description when the procedures of relating spectral and positional information are implemented. This problem can be overcome by upgrading surface models and utilizing them for refined surface descriptions. Effective methodologies for enhancing surface models should be introduced into the framework.

1.3 Research Objectives and Scope

The objective of this research is to introduce a new framework for accurate and realistic surface description of urban environments in an automated manner. The framework will be constructed based on the utilization of both photogrammetric and LiDAR data. Furthermore, the complementary properties of the two datasets will be fully exploited in the system to accomplish the objective of this research.

Some research has been conducted utilizing either high overlap/sidelap photogrammetric data or high point density LiDAR data in order to cater specifically to surface reconstruction over urban areas with complex structures (Wang et al., 2008;

Vosselman, 1999; Rottensteiner and Briese, 2002). In contrast, the proposed research is designed to exploit imagery and LiDAR data acquired through conventional mapping missions (20% sidelap and 60% overlap for photogrammetric data, and around 1.0 point per square meters for LiDAR data), while providing performance that is equal to or better than that achieved through intensive data acquisition.

A summary of the procedures in the framework proposed in this research is depicted in Figure 1.1. The procedures introduced can be categorized into three stages: 1) prerequisites; 2) those used for relating image spectral information to the object positional information; and 3) those used for enhancing object space positional information/description.

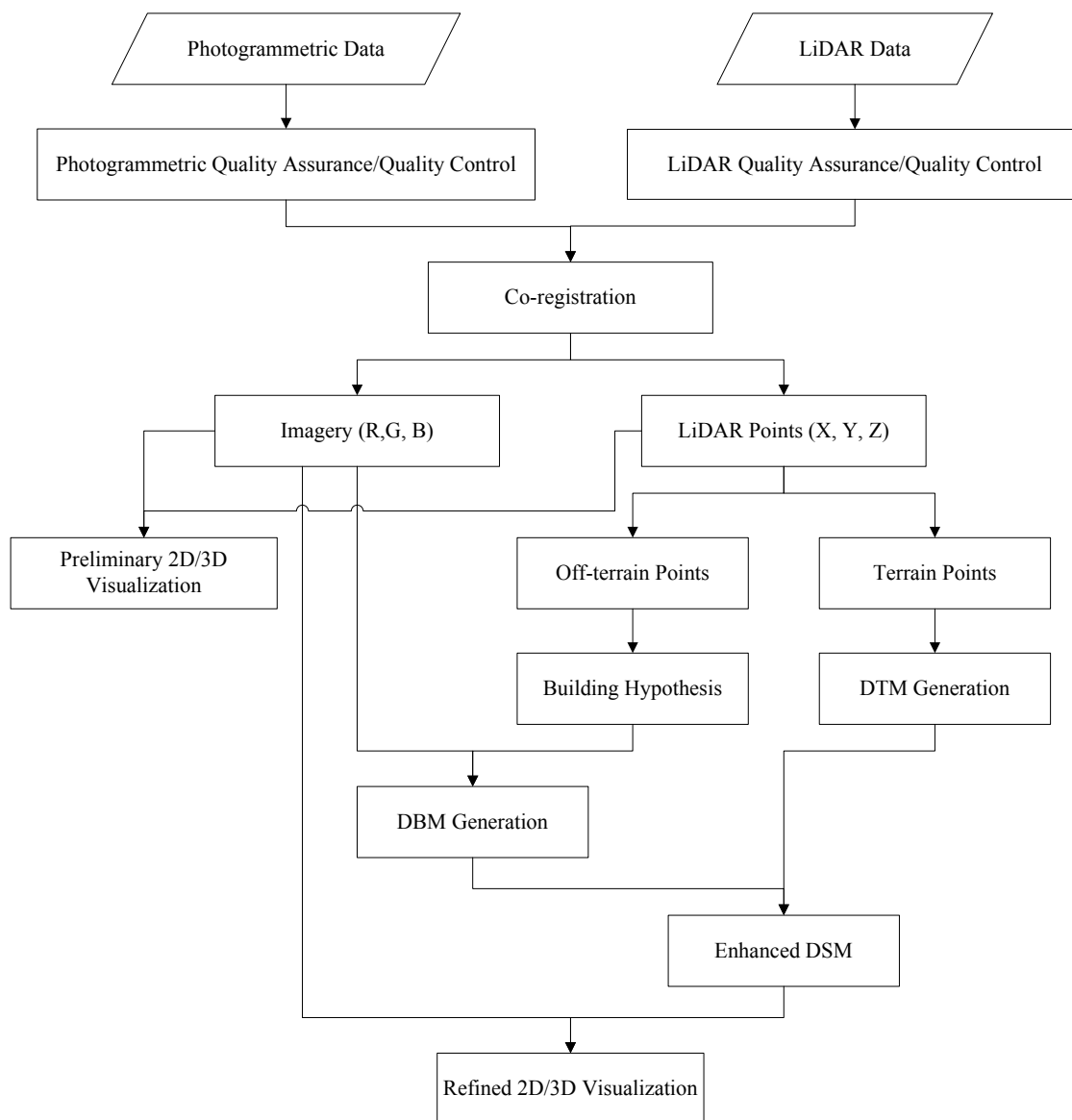


Figure 1.1: The proposed framework for better surface description.

Prerequisites

Since both photogrammetric and LiDAR datasets are considered in this research, several prerequisite procedures are necessary to process the different dataset types and to integrate them. The procedures involve 1) Photogrammetric and LiDAR quality assurance; 2) Photogrammetric and LiDAR quality control; and 3) Co-registration.

Quality assurance comprises management activities to ensure that a process, item, or service is of the quality needed by the user. It deals with creating management controls that cover mission planning, implementation, and review of data collection activities. The key activity in the quality assurance is the system calibration procedure. In order for the final output to be as accurate as possible, all the system components should be accurately calibrated. Internal camera characteristics, which are usually known as the Interior Orientation Parameters (IOP), are derived through the process of camera calibration. In addition, the biases in the bore-sighting parameters relating LiDAR components should be derived.

On the other hand, quality control provides routines and consistent checks to ensure data integrity, correctness, and completeness. In other words, quality control is to check whether the desired quality has been achieved. Photogrammetric quality control is implemented by the check point analysis and the precision evaluation of the derived data. Internal and external LiDAR quality control can be implemented by evaluating the degree of consistency among the LiDAR footprints in overlapping strips and by utilizing LiDAR control targets, respectively. This research will adopt the camera and LiDAR system calibration processes and LiDAR quality control methods recommended by Habib et al. (2006a), Habib et al. (2008a), and Al-Durgham (2007), respectively. Once the quality of

the photogrammetric and LiDAR data has been verified, the data can be used with confidence to produce various products for many different applications. Since this research utilizes two datasets from different sources, the datasets must be registered with respect to a common reference frame. Photogrammetric geo-referencing is a process to define the camera's position and orientation relative to the object space coordinate system at the moment of exposure. This process will be performed by using two types of registration primitives: areal and linear control features acquired from LiDAR data. This research will adopt the georeferencing techniques recommended by Habib et al., (2008c). The adopted techniques will use the LiDAR data as the source of control for the image geo-referencing. The results from the adopted techniques are highly compatible with those by using GCPs for the image geo-referencing (Ghanma, 2006).

Relating positional and spectral information

After the photogrammetric dataset has been aligned to the LiDAR data reference frame, the data are ready to be used for surface description, which is done by relating the spectral and positional surface information from both datasets. Orthophoto production aims to correctly relate the image spectral and LiDAR positional information. Differential rectification has traditionally been used for orthophoto generation (Konecny, 1979; Novak, 1992). However, for large scale imagery over urban areas, differential rectification produces serious artefacts in the form of double mapped areas at object space locations with sudden relief variations (Skarlatos, 1999). Such artefacts are removed through the use of true orthophoto generation methodologies, which are based on visibility analyses. Angle-based true orthophoto generation techniques are introduced

in this research to overcome the problems associated with current true orthophoto generation techniques. One should note that the quality of the visualization in 2D (which is true orthophotos) and 3D (which is produced by draping the true orthophotos on top of the surface model) will be affected by two factors: 1) the performance of the true orthophoto generation techniques; and 2) the quality of the surface models. Since new true orthophoto generation techniques will be proposed in this research, the only remaining factor is the quality of the surface models. Usually, surface models generated by LiDAR points cannot show breaklines (especially, building boundaries in urban environments) precisely. Hence, the procedures that follow will incorporate new methodologies for enhancing surface models.

Enhancing surface models

To improve the quality of the 2D and 3D visualizations, the building boundary information should be added to the surface models. Since Digital Building Model (DBM) has precise building boundary information, this research will propose a new DBM generation method while overcoming the limitations of the current techniques which will be discussed in Chapter 2. One should note that planar rooftops bounded by straight lines will be the target of the DBM generation method which will be proposed in this research. Brief explanation of the method is addressed in the following paragraphs. First, terrain/off-terrain point classification will be carried out using LiDAR data only. This research will adopt the techniques introduced by Habib et al., (2008b) for this classification. The angle-based occlusion detection technique, which has already been proposed for true orthophoto generation, is extended and applied to terrain/off-terrain

point classification. DBM will be generated through further processing of the off-terrain points and imagery. In order to do this, building hypotheses will be generated using the off-terrain LiDAR points. Then, building primitives (i.e., planar patches constituting rooftops) with their initial boundaries will be derived from building hypotheses using segmentation and boundary detection methodologies. One should note that all the procedures to acquire building primitives and their initial boundaries are based on LiDAR data only. Since the derived initial boundaries do not accurately represent building primitives, the integration of LiDAR and photogrammetric data will be involved in the digital building model generation procedure. The integration of the two datasets will open the possibility of resolving ambiguities in the matching of conjugate features. Rich information along breaklines and surfaces, obtained from photogrammetric and LiDAR data, respectively, will enable the successful DBM generation in this research. Afterwards, the surface models will be improved by incorporating the produced DBM. Then, 2D and 3D visualizations with the improved quality will be realized by using the improved surface models and corresponding imagery.

1.4 Structure of the Dissertation

The proposed framework for accurate reconstruction and visualization of urban environments is documented in this dissertation. Brief explanations of the chapters constituting this dissertation are addressed as follows.

- Chapter 2 addresses previous research related to the necessary components of the framework for surface description. Literatures on the previous approaches for relating image spectral and LiDAR positional information and DBM generation are reviewed.
- Chapter 3 includes the methodologies used to fulfill the prerequisites of this research. Afterwards, this chapter focuses more upon methodologies for relating image spectral and LiDAR positional information correctly by introducing the improved visibility analysis. Two methodologies developed for true orthophoto generation are introduced.
- Chapters 4 and 5 explain how surface models are enhanced. First, Chapter 4 describes the methodology for building detection and primitive generation using LiDAR data only. The principle of the developed true orthophoto generation method is extended for terrain and off-terrain separation. Also, robust segmentation algorithm based on the voting scheme is proposed.
- Afterwards, Chapter 5 explains the methodologies for building reconstruction, followed by the refined 2D and 3D visualizations. Object-based integration of photogrammetric and LiDAR data is introduced and utilized for feature matching and precise building boundary segment selection.
- Chapter 6 describes experiments and evaluations carried out using real datasets to demonstrate and validate the performance of the proposed methodologies. Qualitative and quantitative evaluations are conducted to prove that the proposed research provides accurate and reliable results.
- Chapter 7 summarizes the conclusions drawn from this research. Moreover, contributions and recommendations for future work are addressed.

Chapter 2 : Literature Review

2.1 Introduction

Recall that the objective of this research is to provide a new framework for better surface description with accurate positional and spectral information. Since this research is dealing with surface description, relevant research activities for relating image spectral information and LiDAR positional information will be reviewed first (in Section 2.2). Rectification and visibility analysis used in orthophoto and/or true orthophoto generations will be addressed in the section. One should note that the LiDAR positional information does not sufficiently represent breaklines (which are mostly coming from buildings in urban environments) due to the irregular and sparse nature of the data acquisition process. In this regard, various research studies have focused on building model generation which can provide precise building boundary information. Hence, Section 2.3 will review previous research work discussing building model generation.

2.2 Relating Spectral and Positional Information

Remote sensing imagery are usually acquired through perspective projection, where reflected light rays from the object space pass through the perspective center of the imaging sensor. Such a projection results in scale variation and relief displacement in the acquired imagery. Orthophoto generation aims at eliminating relief displacement from perspective imagery. As a result, orthophotos are characterized by having a uniform scale and showing objects in their true geographical locations. In other words, orthophotos have the same characteristics of a map. Orthophotos are generated through a rectification

process, which might be direct or indirect (Konecny, 1979; and Novak, 1992). Direct rectification utilizes the internal and external characteristics of the imaging sensor to directly project the image contents onto the Digital Surface Model (DSM) cells. Direct orthophoto generation is carried out through an iterative process. The mechanics of the direct orthophoto generation might leave some of the cells in the DSM with unassigned grey values. Therefore, empty cells have to be interpolated from neighboring ones. In contrast to the direct rectification, indirect orthophoto generation starts by projecting the DSM cell vertices onto the image plane using the internal and external sensor characteristics. The grey value at the projected image location is interpolated using the ones at neighboring cells/pixels. Finally, the interpolated grey value is assigned to the corresponding DSM vertex. Differential rectification is the commonly used term to denote indirect rectification of perspective imagery (Konecny, 1979; and Novak, 1992). The conceptual procedure for ortho-rectification is illustrated in Figure 2.1.

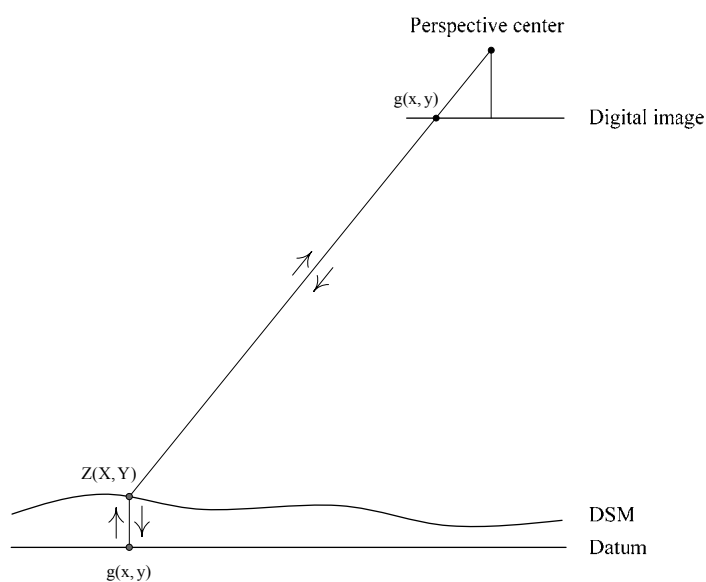


Figure 2.1: Principle of ortho-rectification for orthophoto generation.

When dealing with large scale imagery over urban areas, differential rectification produces a significant artifact, which is double mapped areas at the vicinity of abrupt surface changes (Skarlatos, 1999). Figure 2.2 is a schematic diagram illustrating the double mapping problem. In this figure, points D , E , and F along the DSM are projected onto the image plane at the locations d , e , and f , respectively. The interpolated grey values $g(d)$, $g(e)$, and $g(f)$ are assigned to the corresponding DSM cells. On the other hand, due to the relief displacement caused by the vertical structure, the grey values $g(d)$, $g(e)$, and $g(f)$ will be also assigned to the DSM at the locations A , B , and C , respectively.

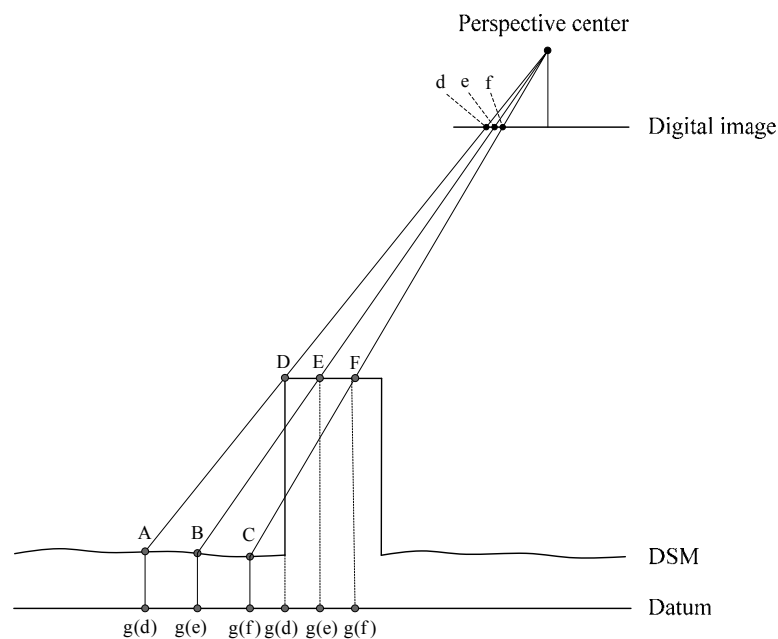


Figure 2.2: Double mapped areas where sudden relief causes duplication of the projected grey values onto the orthophoto plane (datum).

Therefore, these grey values will be incorrectly duplicated in the orthophoto plane (datum) causing double mapping of the same area. A real example of the double mapping problem is illustrated in Figure 2.3, where the perspective image and the generated orthophoto are shown. As it can be seen in Figure 2.3(a), the vertical structures have significant relief displacements that cause considerable occlusions in the object space. The generated orthophoto in Figure 2.3(b) shows that the relief effects along the building facades have been removed. However, double mapped areas, which are enclosed by solid black lines, occupy occluded portions of the object space. Double mapped areas constitute a severe degradation and are a major obstacle to the interpretability of the generated orthophoto. Therefore, true orthophoto generation methods focus on the elimination of the double mapped areas. The basic principle of these methods is the identification of occluded areas, which are caused by relief displacements associated with vertical structures in the object space.



(a)

(b)

Figure 2.3: Perspective image (a) and the corresponding orthophoto (b) with double mapped areas enclosed by solid black lines.

True orthophoto generation is mainly concerned with visibility analysis, which has been studied in computer graphics, computer vision, photogrammetry, remote sensing, and telecommunications. The classical visibility algorithms were developed in the early days of computer graphics – late sixties and early seventies (Sutherland et al., 1974). Amhar et al. (1996) proposed a method, which is based on photogrammetric principles, for making true orthophotos using Digital Terrain Models (DTM) and DBM. In this method, two orthophotos, one corresponding to the terrain while the other corresponds to the buildings, are independently generated. The DBM is first used to mask portions of the input image that are covered by man-made structures. The masked image is then used in conjunction with the DTM to generate the terrain orthophoto. In the mean time, the DBM together with the original image is used to generate the building orthophoto. The final true orthophoto is created by combining the terrain and building orthophotos. Therefore, the proposed method by Amhar et al. does not explicitly detect occluded areas. However, occlusions are implicitly considered by utilizing the masked image for the generation of the terrain orthophoto. Kuzmin et al. (2004) proposed a polygon-based approach for the detection of obscured areas for true orthophoto generation. In this method, conventional differential rectification is first applied. Afterwards, hidden areas are detected by using polygonal surfaces, which are generated from a DBM. A common prerequisite for the above methods for true orthophoto generation is the need for a DBM. In other words, the mentioned methods do not work properly without DBM. Other than the proposed method by Kuzmin et al., the majority of existing true orthophoto generation techniques is based on the Z-buffer algorithm (Catmull, 1974; Amhar et al., 1998; Rau et al., 2000; Rau et al., 2002; Sheng et al., 2003; and Zhou, 2005). As it can be seen in Figure 2.2, double

mapped areas arise from the fact that two object space points (e.g., A and D , B and E , or C and F) are competing for the same image location (e.g., d , e , or f , respectively). The Z-buffer method resolves the ambiguity of which object point should be assigned to the image location by considering the distances between the perspective center and the object points in question. Amongst the competing object points, the closest point to the perspective center is considered visible while the other points are judged to be invisible in that image. Since the Z-buffer method has been utilized by many researchers, following paragraphs describe its principle and limitations in detail.

As it was mentioned earlier, the Z-buffer method for true orthophoto generation identifies occluded areas by resolving the ambiguity arising from having more than one object point competing for the same image pixel (Figure 2.2). As it was proposed by Amhar et al. (1998), the implementation of the Z-buffer starts by establishing three 2D arrays with the same dimensions of the input image, which will be referred to hereforth as the Z-buffer arrays, and a visibility map with the same dimensions of the input DSM (Figure 2.4). Two out of the three Z-buffer arrays are used to record the X and Y coordinates of the DSM cell that is projected onto the corresponding image pixel. The third array stores the distances between the perspective center and the respective DSM cells. The visibility map, on the other hand, indicates whether the corresponding DSM cell is visible in the involved image or not.

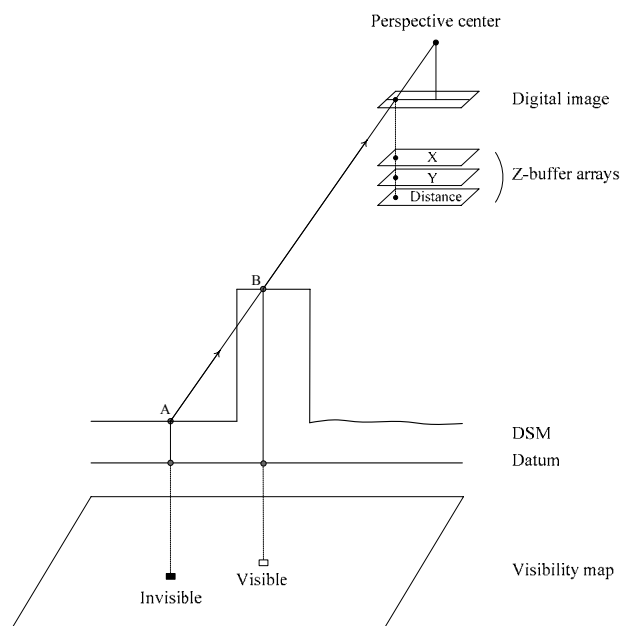


Figure 2.4: Principle of true orthophoto generation using the Z-buffer method.

To illustrate the conceptual basis of the Z-buffer method, one can start by considering the DSM cell A in Figure 2.4. After being projected onto the image plane, the corresponding pixels in the Z-buffer arrays are assigned the coordinates X_A and Y_A as well as the distance between the perspective center and the object point A , d_A . In the mean time, the corresponding cell in the visibility map is initialized to indicate a visible DSM cell. Such a process is repeated while considering other cells within the DSM. When dealing with the DSM cell B , the algorithm determines that the corresponding image pixel has already been linked to the DSM cell A . To resolve which of the two DSM cells should be assigned to that image pixel, the distances from the perspective center to A and B (d_A and d_B , respectively) are computed and compared. Since d_A is greater than d_B , the DSM cell B is declared visible while A is deemed invisible. Therefore, the Z-buffer arrays

are updated where X_A , Y_A , and d_A are replaced with X_B , Y_B , and d_B , respectively. In addition, the visibility map is modified to indicate that the DSM cell A is invisible, while B is visible. After considering all the cells within the DSM, the Z-buffer arrays are used to transfer the grey values from the input image to the corresponding locations in the orthophoto plane. In the mean time, the visibility map can be used to indicate occluded areas in the object space due to relief displacement effects.

The following paragraphs will briefly discuss the drawbacks of the Z-buffer method as well as possible solutions to mitigate the effects of these problems. To illustrate the manifestations of these drawbacks, a synthetic DSM consisting of 9 buildings, 50m high, over a flat terrain is generated (Figure 2.5). The perspective center of the simulated image over the DSM is located above the centroid of the central building. The performance of the Z-buffer method will be evaluated through the quality of detected occlusions.

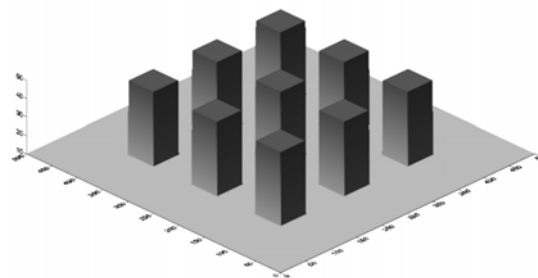


Figure 2.5: Simulated data with nine buildings over a flat terrain.

Detected occlusions by the Z-buffer method depend on the relative relationship between the DSM cell size and the Ground Sampling Distance (GSD) of the imaging

sensor. If the DSM cell size is less than the GSD of the imaging sensor, false occlusions in flat areas will be reported. Figure 2.6 illustrates such an instance, where several DSM cells not occluding each other are projected onto the same image pixel. As a result, the DSM cell, which is closest to the projection center, will be deemed visible, while the others are incorrectly considered to be occluded. Another illustration of such a phenomenon is depicted in Figure 2.7, which shows the visibility map associated with the DSM in Figure 2.5. Black portions in this map indicate occluded areas. As it can be seen in this figure, the over sampling of the DSM would lead to false occlusions, as represented by the black grid between the buildings.

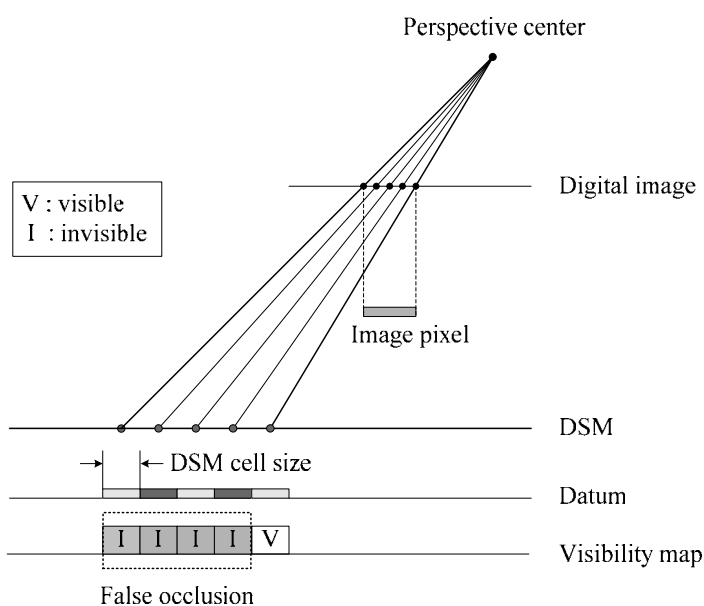


Figure 2.6: False occlusions are reported whenever the DSM cell size is smaller than the GSD of the imaging sensor.

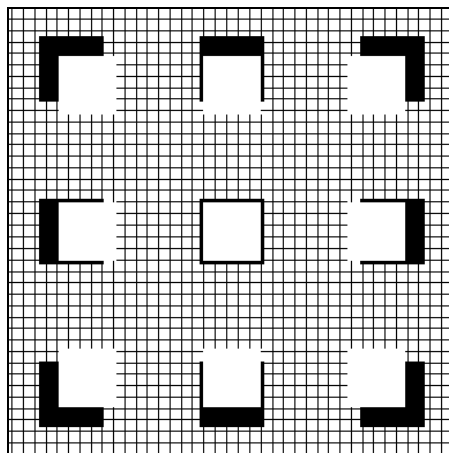


Figure 2.7: Visibility map corresponding to the DSM in Figure 2.5 where the DSM cell size is chosen to be smaller than GSD of the imaging sensor (black grids between buildings indicate false occlusions).

To avoid these false occlusions, the DSM cell size should be made equivalent to the GSD of the imaging sensor. However, the GSD is uniquely defined if and only if one is dealing with an ideal dataset with a vertical image over flat and horizontal terrain. In other words, the GSD cannot be uniquely defined when one is dealing with a dataset including terrain and vertical structures. Therefore, choosing the DSM cell size to be equivalent to the nominal GSD (e.g., GSD at the terrain surface) will not guarantee the absence of incorrectly detected occlusion. A problem to the DSM cell size is shown in Figure 2.8. In this case, the DSM cell size is chosen to be equivalent to the GSD at the terrain surface. However, such a choice will lead to having non-compatible resolutions at the building roofs. As a result, false visibility will be reported in the occluded areas by vertical structures. A further illustration of this problem is depicted in Figure 2.9, where false visibility, as represented by a white grid, is detected within the occlusions associated with the vertical structures in Figure 2.5. The false visibility problem will

escalate as the height of the vertical structures becomes significant in relation to the flying height of the imaging sensor.

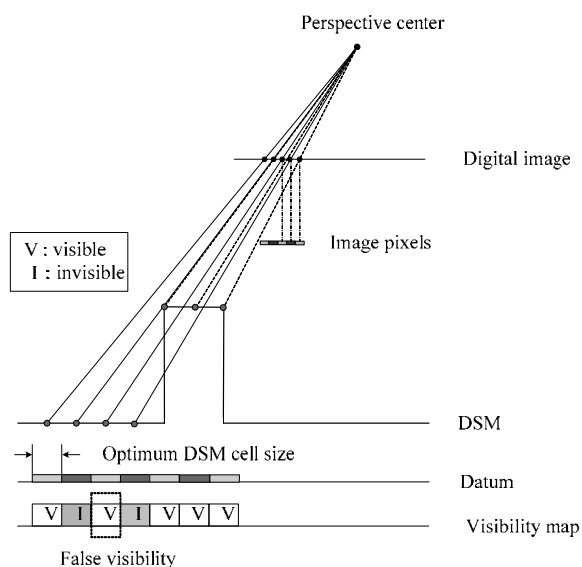


Figure 2.8: Optimal sampling of the DSM at the terrain level and tall vertical structures might lead to false visibility in occluded areas.

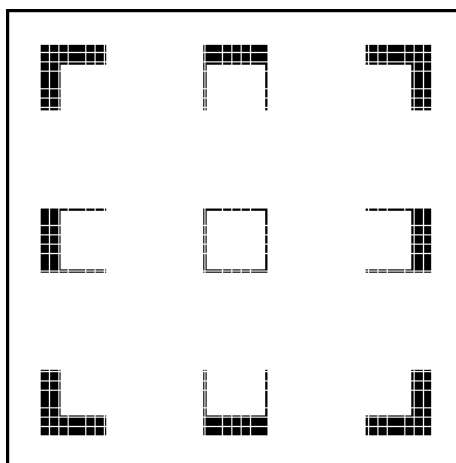


Figure 2.9: Detected occlusion areas with optimal sampling of the DSM at the terrain level for the DSM in Figure 2.5 (white lines within the detected occlusions indicate false visibility).

Another significant defect of the Z-buffer method is the false visibility associated with narrow vertical structures. This problem is commonly known in the photogrammetric literature as the M-portion problem (Rau et al., 2000, 2002). The M-portion problem is shown in Figure 2.10. In this case, some of the pixels in the occluded area do not have any competition from points on the building roof (as represented by the two terrain points close to the vertical structure in Figure 2.10). In such a case, terrain points in the occluded area will be incorrectly deemed visible as seen in Figure 2.10(a). To minimize this problem, additional pseudo groundels are introduced along the facades of vertical structures (Figure 2.10(b)). In such a case, a DBM should be available. False visibility caused by the M-portion problem as well as improved occlusion detection after the introduction of pseudo groundels for one of the buildings in Figure 2.5 are shown in Figure 2.11(a) and Figure 2.11(b), respectively. It should be noted that the pseudo groundels also reduce the false visibilities that have been reported in the previous section, which have been shown in Figure 2.9.

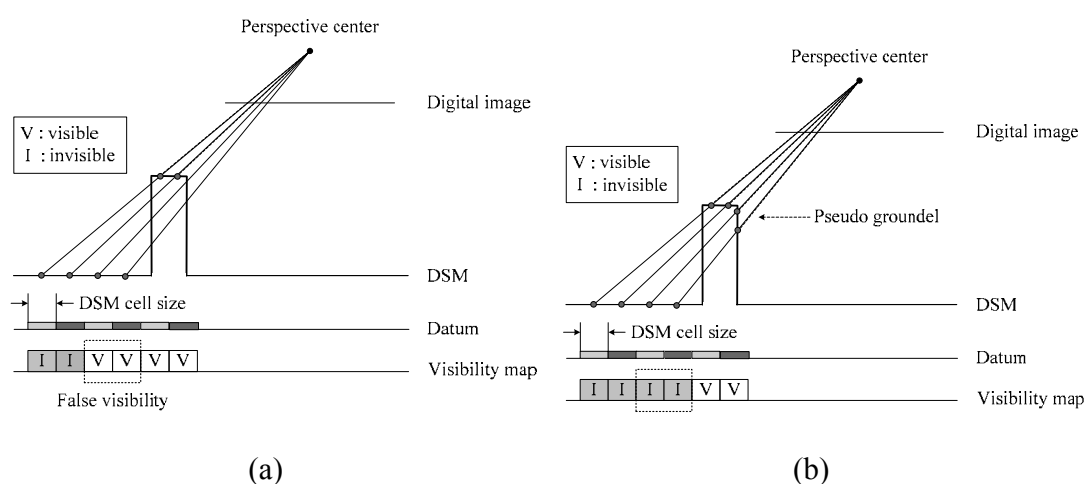


Figure 2.10: M-portion problem leads to false visibility (a), which can be minimized by the introduction of pseudo groundels (b).

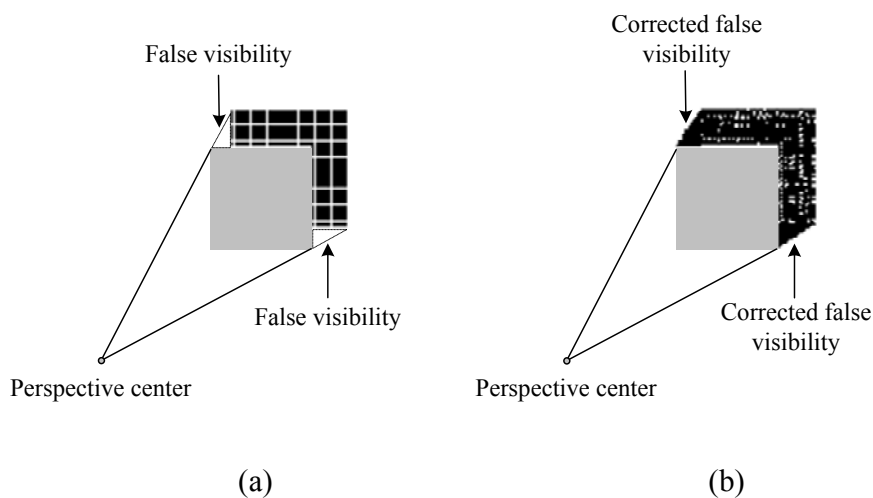


Figure 2.11: The M-portion problem leads to false visibility as indicated by the dashed triangles in (a) and can be mitigated by the introduction of pseudo groundels (b).

For the verification of the limitations of the Z-buffer method mentioned above, a true orthophoto (Figure 2.12(b)) is generated by using DSM (Figure 2.12(a)) and aerial image in Figure 2.3(a). Also, Figure 2.12(c) shows a closer look at the vicinity of one building enclosed by white circle in Figure 2.12(b). Black portions in Figure 2.12(b) and Figure 2.12(c) indicate occluded areas due to relief displacement at the building's locations. In spite of the fact that the DSM cell size has been adjusted to be compatible with the GSD of the digital image as well as numerous pseudo groundels have been introduced along the building facades, the Z-buffer methodology is still showing false visibilities and occlusions. Also, the produced true orthophoto does not have sharp (or crisp) building boundaries as can be seen in Figure 2.12(c). One should note that the DSM produced from LiDAR data does not sufficiently represent breaklines (e.g.,

building boundaries) due to the irregular and sparse nature of the LiDAR data. Hence, the incompleteness of DSM leads to negative effects on the quality of the true orthophoto (especially, around the building boundaries) regardless of the used true orthophoto generation methods (as long as the methods are using DSM for true orthophoto generation).

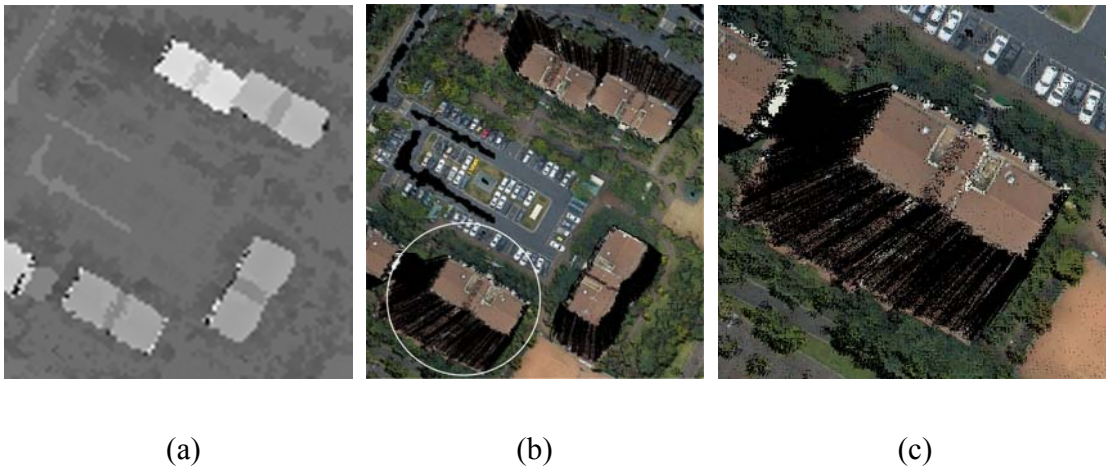


Figure 2.12: LiDAR DSM corresponding to the area in Figure 2.3(a), true orthophoto generated using the Z-buffer method (b) with a closer look at the building within the white circle (c).

In summary, to minimize the problems associated with the Z-buffer method, it should be preceded by interpolating the DSM to a resolution that is equivalent to the nominal GSD of the imaging sensor. Moreover, a DBM should be available to allow for the introduction of pseudo groundels along the facades of vertical structures. However, these precautions would not guarantee the absence of false occlusions or visibilities in the

resulting true orthophoto. Therefore, generated orthophotos from the Z-buffer method are post-processed using a majority filter to eliminate sporadic false visibilities or occlusions. Also, the incompleteness of the DSM negatively affects the quality of true orthophotos. To resolve the problem caused by the incompleteness of the DSM, there is a need for building boundary information which can be provided by a DBM. Hence, many researchers who are interested in surface description have focused on the development of DBM generation methods. The literature on the DBM generation is reviewed in the next section.

2.3 Building Model Generation

In the past few years, much research effort in computer vision and photogrammetry has been directed at DBM generation. The main goal of the implementation of building modeling procedures is to promote automated generation of 3D urban models. A 3D urban model also requires the modeling of trees and other elements of the urban furniture; however, buildings are the most important and complex features.

Several approaches have been proposed in recent years. DBM generation is usually performed in two steps: building detection and building reconstruction. Building detection is the process of generating building hypotheses by differentiating buildings from other objects within the data. Building reconstruction, on the other hand, utilizes the hypothesized building regions in the data to derive its 3D representation (Ma, 2004). The reconstruction of the buildings in previously detected regions of interest can be carried out using two different approaches: model driven or data driven methods (Förstner 1999;

and Faig and Widmer, 2000). Model driven methods are based on parametric building models, where each model is treated as a hypothesis that is verified from information derived from the data. The parametric primitives are usually stored in a model database, which can be instantiated and fit to the data. The model achieving the best fit is the selected one. Data driven approaches, on the other hand, involve the use of generic models. Since generic models do not make any assumptions regarding the building shape, its implementation can be a very complex task. For that reason, the most commonly adopted model – in data driven approaches – is the polyhedral model. The polyhedral model, which is considered a sub-model of the generic model, assumes that a building is bounded by planar surfaces. Constructive Solid Geometry (CSG) model – an alternative approach – is a fusion of the model driven and the data driven methods (Ma, 2004). In this approach, it is assumed that a complex building can be subdivided into several simple building model primitives (parametric models) which are then combined using boolean operators (Haala et al., 1998; Vosselman and Dijkman, 2001; and Suveg and Vosselman, 2004).

Regarding the sources of data used for DBM generation in previous studies, they can be categorized into approaches using only imagery (monocular, stereo, or multiple images), approaches using only LiDAR, and approaches using data integration (Figure 2.13). The classification criterion in the figure is used in the following subsections to review previous research work.

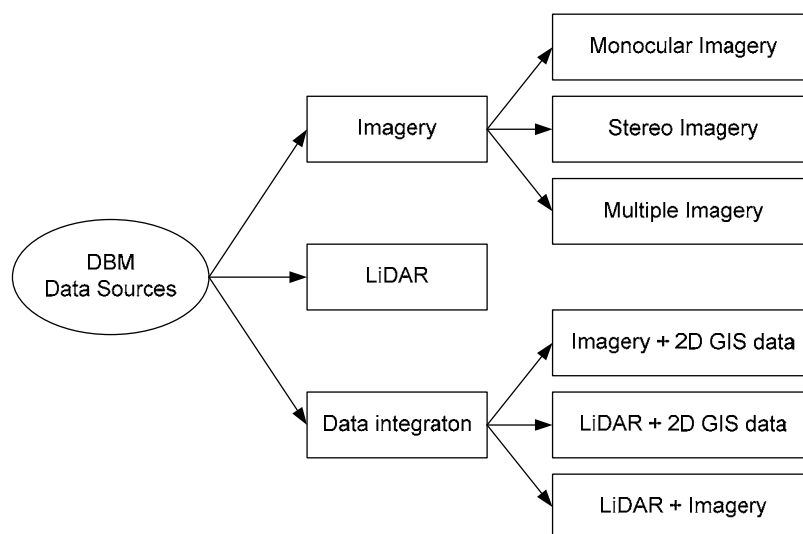


Figure 2.13: Sources of data used for DBM generation.

2.3.1 Monocular imagery

Some of the first approaches in previous work were based on the use of monocular imagery (Huertas and Nevatia, 1988; and McGlone and Shufelt, 1994). Since these approaches do not make use of 3D information in the reconstruction process, they are also referred to as 2D approaches. The process usually starts by detecting the building features/primitives (e.g., edges of the building) followed by the reconstruction process. The third dimension (i.e., the building height) is usually estimated using shadows and vertical walls. Shadows and vertical walls are also used for building hypothesis verification (Lin et al., 1995). The algorithms are mostly based on grouping the detected building primitives. Some assumptions regarding the internal building characteristics (e.g., orthogonality, parallelism, and symmetry) are usually employed to find building features/primitives. Building region detection is usually performed after the analysis of the building primitive topology. The main problem of this approach is that it is strongly

dependent on the quality of the detected edges/corners as well as the grouping procedure. Poor edge detection can be caused by several factors: (i) low image contrast or variation in contrast along the building edges, (ii) presence of trees close to the building boundaries, (iii) presence of structures on top of the roof, and finally (iv) the presence of a huge amount of detected edges from different objects rather than buildings, where most are noisy edges. The poor quality of the edge detection makes the process of identifying and grouping building edges quite complex (Wang, 1999). In addition to this, the use of shadow to infer the height of the building is not a reliable procedure since in most of the cases it does not appear completely in the image (Lin et al., 1995).

2.3.2 Stereo and multiple imagery

Differently from the approaches mentioned in the previous section, numerous authors have proposed DBM generation procedures based on the use of stereo and multiple imagery. These approaches make use of three-dimensional information in the modeling process (building detection and reconstruction) which is determined by the matching of conjugate features in overlapping imagery. According to Suveg and Vosselman (2004), the approaches that make use of stereo imagery can be classified into two groups: (i) Methods that use monoscopic techniques for building recognition and reconstruction and use stereoscopic techniques for validating the reconstruction and inferring the third dimension (Roux and McKeown, 1994; Nevatia et al., 1997; and Noronha and Nevatia, 2001). (ii) Methods that use stereoscopic techniques during the building modeling (Baltasavias et al., 1995; Henricsson et al., 1996; Haala and Hahn, 1995; and Weidner, 1996).

The most obvious advantage of deriving the 3D information to be used in the building detection and reconstruction process is that real-world geometric constraints can be utilized (Wang, 1999). The process usually starts by deriving a DSM by image matching. The generated DSM is then used for building detection (building hypothesis generation). Usually, the DSM generated from image matching is very noisy. For this reason, several authors proposed some sort of post-processing to smooth it down (Baltasavias et al., 1995; and Weidner, 1996). Also, other researchers (Baillard and Zisserman, 1999; Kim et al., 2001; and Wang, 2008) proposed building reconstruction approaches using multiple images. They mostly focused on the improvement of matching quality and solution for occlusion problems. Although some satisfactory results can be achieved in some cases, feature matching in large-scale imagery over urban areas still remains to be an ill-posed problem.

Due to the complexity of the building modeling using imagery, the majority of existing literatures is based on model driven approaches. In this type of approach, more prior knowledge about the building model is utilized in the modeling process. Therefore, deficiencies in the feature extraction procedure (due to low image contrast, occlusion, and trees close to the building boundaries) can be more easily compensated for. Although this type of approach provides satisfactory results, its use is limited to simple building models such as flat-roof and gable buildings. When more complex building types need to be handled, data driven approaches must be employed.

One should note that fully automatic systems, which can handle any type of building, are still in the research stage. Automation in building modeling using only imagery is a very complex task. For that reason, semi-automatic approaches were

proposed by several authors (Grün and Dan, 1997; and Grün and Wang, 1998). In a semi-automated system, processes that are difficult or less efficient for a computer to complete are performed by the user (Wang, 1999). In other words, human ways of perception, which are difficult to model, such as the recognition and interpretation embedded in a specific context, will be more efficient and reliable if realized by the system operator. Overall, in operational conditions, user interaction can solve or circumvent problems that cannot be reliably solved by a software program alone.

In summary, the building reconstruction methods utilizing either stereo or multiple images still suffer from the quality of image matching; therefore, they have low degree of automation of DBM generation (Brenner, 2005). Still, extensive human intervention is needed to acquire accurate results.

2.3.3 LiDAR

LiDAR has emerged as an important source of data for the generation of 3D city models. The main advantage is the direct acquisition of a reliable and dense 3D point cloud in contrast to the error-prone matching techniques when using stereo or multiple images. The LiDAR research community has been very active in the development of algorithms for the post-processing of LiDAR data, especially for DBM generation (Alharthy, 2003; Charaniya, 2005; Maas and Vosselman, 1999; and Vosselman, 1999).

A classification procedure to separate terrain and off-terrain points is usually performed to help with the building detection. A substantial portion of existing techniques is based on mathematical morphology and includes the methods presented by Kilian et al. (1996), Vosselman (2000), Roggero (2001), and Zhang et al. (2003). In the

proposed method by Vosselman (2000), the classification of LiDAR data is based on two operations: morphological erosion using a pre-defined discriminant function and comparison between the eroded and original surfaces. A point is classified as a terrain point if its original height does not exceed the height of the eroded surface at the same location. A variation of this method was proposed by Roggero (2001), where the terrain is extracted using a local morphological operator. The shape of this operator is designed according to the slope of the bare earth. Since the shape of the bare earth is not known, a local linear regression procedure is used to derive an estimate of its shape. The main limitation of morphological filters is their sensitivity to the utilized window size as it relates to the size of off-terrain objects such as buildings and forest canopy. For example, a small window will wrongly classify large buildings as terrain. A larger window, on the other hand, might classify portions of a steep terrain as non-ground. To overcome such a limitation, multiple window sizes have been proposed by Kilian et al. (1996) and Zhang et al. (2003). Other than the window size, the performance of morphological filters depends on the designed discriminant function.

Another group of LiDAR point classification techniques is based on the manipulation of a Triangulated Irregular Network (TIN). In Axelsson (2000), ground points are classified through progressive densification of a TIN model. The process starts with a coarse TIN, whose vertices are derived from the lowest points in local areas with a predefined size. The performance of this procedure depends on the local area size and the angle that a new point makes with the facet being densified. The algorithm proposed by Sohn and Dowman (2002) fragments a LiDAR Digital Elevation Model (DEM), which has been convolved with heterogeneous terrain slopes, into a set of homogeneous sub-

regions. The terrain is defined by sub-regions, which can be characterized by a single slope. The main problem with this method, as reported by Sithole and Vosselman (2004), is unreliable classification of low and complex objects. LiDAR classification using linear prediction and hierarchic robust interpolation has been proposed by Kraus and Pfeifer (1998), Kraus and Pfeifer (2001), Pfeifer et al. (2001) and Briese et al. (2002). In this approach, one starts with a rough approximation of the terrain surface model. The defined surface model is iteratively reduced to the terrain surface using linear prediction with the help of a pre-defined weighting function. The quality of the derived DTM depends on the design of the weighting function. Sithole and Vosselman (2004) reported that linear prediction procedures might lead to unreliable classification of low and complex objects. The last group of LiDAR point classification is based on segmentation techniques. Jacobsen and Lohmann (2003) developed a classification procedure, which starts by segmenting the point cloud. The segments are then categorized into terrain and off-terrain regions using the height difference between neighbouring segments. Segmentation techniques are computationally expensive especially when dealing with large areas. Other filtering algorithms are also introduced by many researchers (Elmqvist et al., 2001; Haugerud and Harding, 2001; Brovelli et al., 2002; Wack and Wimmer, 2002; Masaharu and Ohtsubo, 2002; and Akel et al., 2007). A detailed comparison of some of these filters is provided by Sithole and Vosselman (2004).

The off-terrain points usually include points that belong to trees and buildings. By using attributes, such as surface roughness, buildings can be distinguished from trees. In the reconstruction process, planar roof patches are segmented in the detected building regions. Segmentation techniques can be roughly divided into two categories (Vosselman,

2004). The first category includes the techniques that segment point clouds based on the proximity of points and the similarity of the locally estimated attributes from the surface. The techniques belonging to the second category aggregate points with similar attributes into clusters in a parameter space (or attribute space).

Several researchers (Hoover et al., 1996; and Lee and Schenk, 2001) utilized the region growing method proposed by Besl and Jain (1998), which extends seed regions to adjacent points while considering the proximity and attribute similarity of points for segmenting LiDAR points. In comparison to the region growing method built in the spatial domain, there are some techniques which segment points in the parameter space (or attribute space). Vosselman and Dijkman (2001) extended Hough transform (Hough, 1962) to deal with planar surfaces in 3D. Instead of focusing on extracting planar surfaces, some researcher developed clustering methods offering generality and flexibility in accomodating spatial relation and attributes to distinguish different types of surfaces such as vegetation, smooth surfaces, and planar surfaces (Axelsson, 1999; Mass, 1999; Filin, 2002; Vosselman et al., 2004; and Filin and Pfeifer, 2006). These methods are based on an attribute vector (which consists of the proximity of points, the parameters of the tangent plane, and relative height different between the points) defined by a point and its neighbouring points (Axelsson, 1999; Mass, 1999; Filin, 2002; Vosselman et al., 2004; and Filin and Pfeifer, 2006). In this research's point of view, the above segmentation techniques suffer from the following problems: 1) Region growing based segmentation depends heavily on the selection of seed points (or seed regions); the segmentation performance might be sensitive to the choice of seed points (Besl and Jain, 1998). 2) Moreover, region growing methods utilize similarities while locally comparing

the values among neighbouring points without globally considering the local similarities of the points. 3) The segmentation techniques based on parameter space do not consider the connectivity of points. This limitation causes the segmentation results to contain many spurious surfaces which do not exist in reality (Vosselman and Dijkman, 2001; and Filin, 2002). 4) The clustering techniques based on the attribute vector do not involve seed points; however, efficiency issue arises. With the increase in the number of attributes that are utilized in the clustering procedure, the amount of memory required increases tremendously.

After the planar patches are acquired from the segmentation process, building boundaries can then be modeled. Intersection of surface patches and regularization of the patch boundaries are utilized by Vosselman (1999), Mass and Vosselman (1999), and Sampath and Shan (2007). The problem associated with building reconstruction using only LiDAR is that building outlines are not determined precisely. This can be explained by the irregular and sparse nature of the LiDAR data. In other words, there is no guarantee that the LiDAR footprints will capture surface discontinuities such as building boundaries. Hence, the accuracy of the generated building boundaries will be highly dependent on the LiDAR point density (Wang et al., 2008).

2.3.4 Data integration

Several authors have proposed the integration of different data sources for 3D building reconstruction. The integration of imagery and 2D Geographic Information System (GIS) data (i.e., building ground plans) has been proposed by Suveg and Vosselman (2004). The use of the ground plans helps in the building hypothesis

generation and provides clues about the structure of the building. This is particularly useful in the process of partitioning the building into simple parts when using the CSG model. The integrated use of LiDAR and 2D GIS data for DBM generation has been exploited by Haala et al. (1998) and Vosselman and Dijkman (2001). 2D GIS data provided an improved quality of building boundaries in their research. They also employ the CSG model in the reconstruction process. The ground plans are subdivided into rectangular primitives and the selection of the parametric primitive for each 2D rectangle is based on the analysis of the LiDAR DSM. Although existing ground plans can be useful information in the sense that they reduce the search space in the reconstruction procedure, they might be out-of-date, incomplete, or improperly co-aligned with LiDAR or imagery data.

Based on the discussion mentioned in Section 2.3.2 and Section 2.3.3, it is obvious that overlapping imagery provides the necessary geometric and spectral information for accurate and detailed DBM generation. Feature matching, however, leads to a low level of automation (especially, when dealing with large scale imagery over urban areas with complex building models). LiDAR systems, on the other hand, directly provide 3D positional information, which leads to a more reliable building detection and reconstruction (Brenner, 2005). Nevertheless, the irregular and sparse nature of the LiDAR data will negatively affect the quality of the building boundaries. Therefore, the integration of LiDAR data and aerial imagery for DBM generation has gained a significant attention by the research community (Rottensteiner and Jansa, 2002; McIntosh and Krupnik, 2002; Schenk and Csatho, 2002; Seo, 2003; Hu et al., 2004; Ma, 2004; Brenner, 2005; Chen et al., 2005; and Lee et al., 2008).

For example, satisfactory results were demonstrated by Ma (2004) and Hu et al. (2004), where LiDAR data was utilized to detect building regions and reconstruct initial 3D building models. The initial building models are then refined by integrating LiDAR data and imagery. Chen et al. (2005) integrated a region-based segmentation and knowledge-based classification procedures to detect building regions by investigating the surface roughness and texture data in LiDAR and imagery, respectively. Then, identified planar patches in the LiDAR data and extracted edges from imagery are integrated to determine 3D boundaries of the building models through a split-merge-shape technique. The main limitation of this approach is that small and thin objects are filtered out during the building detection procedure. Lee et al. (2008) extracted initial building regions and coarse building boundaries from LiDAR data with the assistance of colour segmentation in aerial imagery. Then, precise building boundaries are defined by replacing the coarse building boundaries with matched line segments from imagery. Reliable results were shown in this research. However, the quality of the results strongly depends on successful derivation of the coarse building boundaries. Most of the previous work has been mainly focusing on buildings with a regular shape. DBM generation of complex structures still remains to be a challenging issue.

2.4 Summary

This chapter first reviewed relevant research activities for relating image spectral and LiDAR positional information. Rectification and visibility analysis used in the current orthophoto and/or true orthophoto generation techniques were discussed. The review has shown that the most popular true orthophoto generation technique (i.e., Z-

buffer method) is sensitive to the relative relationship between the DSM cell size and the GSD of the imaging sensor. If the DSM cell size is less than the GSD of the imaging sensor, false occlusions in the terrain surfaces will be produced. To avoid this problem, one should make the DSM cell size equivalent to the GSD of the imaging sensor. However, such a choice will lead to having non-compatible resolutions at the building roofs and false visibility will be produced in the occluded areas by buildings. Moreover, the Z-buffer method requires the availability of a DBM to resolve the false visibility problem associated with narrow vertical structures, where artificial points along building facades are introduced. Also, it is discussed that the incompleteness of the DSM negatively affects the quality of true orthophotos especially around the building boundaries. Hence, DBM consisting of building boundary information is necessary to resolve the problem caused by the incompleteness of the DSM.

Since the surface model derived from the original LiDAR data does not sufficiently represent breaklines along the building boundaries in urban environments, many studies have paid attention to building model generation (which include precise building boundaries). Hence, previous research studies focusing on building model generation were also discussed. The previous studies are categorized into three types of approaches according to the sources of data used for DBM generation, which are 1) using only imagery (single, stereo, and multiple images), 2) using only LiDAR, and 3) using data integration. DBM generation methods using monocular imagery usually employed some assumptions regarding the internal building characteristics (e.g., orthogonality, parallelism, and symmetry). These assumptions are not valid for more complex buildings.

These methods can only work for simple building models. Compared to the methods based on single image, other approaches using stereo or multiple images usually provide more reliable results. However, feature matching in large-scale imagery over urban areas still remains to be an ill-posed problem. This problem leads to a low degree of automation in the DBM generation. On the other hand, manipulation of LiDAR data is becoming a popular tool for DBM generation since elevation data is directly acquired from LiDAR system. The degree of automation in building detection and reconstruction procedures is relatively higher when compared to that using imagery. However, the defined boundaries of the generated DBM are of lower quality due to the irregular and sparse nature of LiDAR data. The discussion has also shown that different types of data sources have their own advantages and disadvantages in terms of DBM generation. Hence, some researchers integrated different types of data sources such as 1) imagery and 2D GIS, 2) LiDAR and 2D GIS, and 3) LiDAR and imagery. 2D GIS information either helped in building hypothesis generation or provided the improved quality of building boundaries. However, it might be out-of-date, incomplete, or improperly co-aligned with LiDAR or imagery data. On the other hand, many researchers have proposed DBM generation methods based on the integration of LiDAR and imagery. Some limitations of the studies based on this approach are explained. After reviewing the current true orthophoto and DBM generation techniques and their limitations, this research will propose new methods for more accurate reconstruction and visualization of urban environments while overcoming the mentioned limitations.

Chapter 3 : Relating Image Spectral and Object Positional Information

3.1 Introduction

In Chapter 2, previous studies related to the necessary components of the proposed framework, and their advantages and disadvantages, were addressed. This chapter will, first, address prerequisite procedures, which are 1) photogrammetric and LiDAR quality assurance; 2) photogrammetric and LiDAR quality control; and 3) co-registration of LiDAR and imagery. These procedures will be explained in Sections 3.2 and 3.3. Once the prerequisite procedures have been conducted, spectral and positional information can be derived from photogrammetric and LiDAR data, respectively. Hence, the methodologies used to correctly relate image spectral information and object positional information are discussed in Section 3.4. For this purpose, two methods are introduced to overcome the problems that have arisen in previous research.

3.2 Quality Assurance and Control of Photogrammetric and LiDAR Data

Quality assurance and control of photogrammetric and LiDAR data are considered to be the necessary components of the proposed framework for better surface description in this research. Quality assurance encompasses management activities to ensure that a process, item, or service is of the quality needed by the user. It deals with creating management controls that cover mission planning, implementation, and review of data collection activities. The key activity in the quality assurance is the system calibration procedure. Internal camera characteristics, which are usually known as IOP, are derived through the process of camera calibration. A typical LiDAR system, on the

other hand, consists of three main components: a Global Positioning System (GPS) system to provide position information, an Inertial Navigation System (INS) unit for attitude determination, and a LASER system to provide range (distance) information between each LASER firing point and corresponding ground point. The quality of the surface derived using a LiDAR system depends on the accuracy of the data derived from the three components mentioned above and the calibration parameters relating these components (i.e., bore-sighting parameters). The camera and LiDAR system calibration methodologies adopted in this research are recommended by Habib et al. (2006a) and Habib et al. (2008a), respectively.

After the calibration of both systems, quality control procedures determine whether the desired quality has been achieved. Photogrammetric quality control is investigated through check point analysis and the precision of the derived data. Internal and external LiDAR quality control can be implemented by evaluating the degree of consistency among the LiDAR footprints in overlapping strips and by utilizing LiDAR control targets, respectively. This research adopts the quality control methods recommended by Al-Durgham (2007). He suggested four different methods for LiDAR quality control analysis. The first two methods utilize the derived conjugate linear features and patches from overlapping strips, respectively. The basic concept of these methods is that conjugate linear features and patches from different strips should be collinear and coplanar in the absence of biases, respectively. The third method called the ICPatch method uses a TIN generated from a strip and raw LiDAR points from the other strip while assuming a point-to-patch correspondence. The last method called the ICPPoint method assumes a point-to-point correspondence between raw LiDAR points from two

different strips. Once the quality assurance and control of photogrammetric and LiDAR data have been conducted, photogrammetric and LiDAR data can be used with confidence to produce surface models for various applications. Since this research deals with two different data types, they must be registered to a common reference frame. Hence, Section 3.3 briefly explains the co-registration techniques to be used, which incorporate both linear and areal features.

3.3 Co-registration

Only after ensuring that the photogrammetric and LiDAR datasets are geo-referenced with respect to a common reference frame, can the synergic properties of the two datasets be fully utilized (Habib and Schenk, 1999). Traditionally, photogrammetric geo-referencing is either done indirectly using Ground Control Points (GCP), or directly using GPS/INS units onboard the imaging platform (Cramer et al., 2000). LiDAR geo-referencing, on the other hand, is done directly using the GPS and INS components of the LiDAR system. When GCP-based or GPS/INS-based photogrammetric geo-referencing is conducted, there might be biases between two reference frames for photogrammetric and LiDAR data. The biases can be caused by utilizing different GPS base stations for photogrammetric and LiDAR data acquisition. In addition, utilization of GCP for photogrammetric geo-referencing is expensive. One should note that LiDAR can be utilized as a source of photogrammetric geo-referencing. Habib et al. (2008c) generated three true orthophotos using a perspective image (Figure 3.1 (a)), a digital surface model, and three sets of EOPs resulting from using GCPs, patches derived from LiDAR, and lines derived from LiDAR as sources of control. They compared the qualities of true

orthophotos generated by using different sources of control. By examining these true orthophotos, it is clear that two of the generated true orthophotos using LiDAR patches and LiDAR lines are compatible (Figure 3.1 (c) and Figure 3.1 (d)). Moreover, the true orthophotos generated using LiDAR patches or lines appear to be more accurate than the one generated using GCPs. This can be observed in the orthophotos, where there are more traces of building boundaries in the latter true orthophoto (Figure 3.1 (b)). For this reason, the features derived from LiDAR data can be utilized as a source of control for photogrammetric geo-referencing.

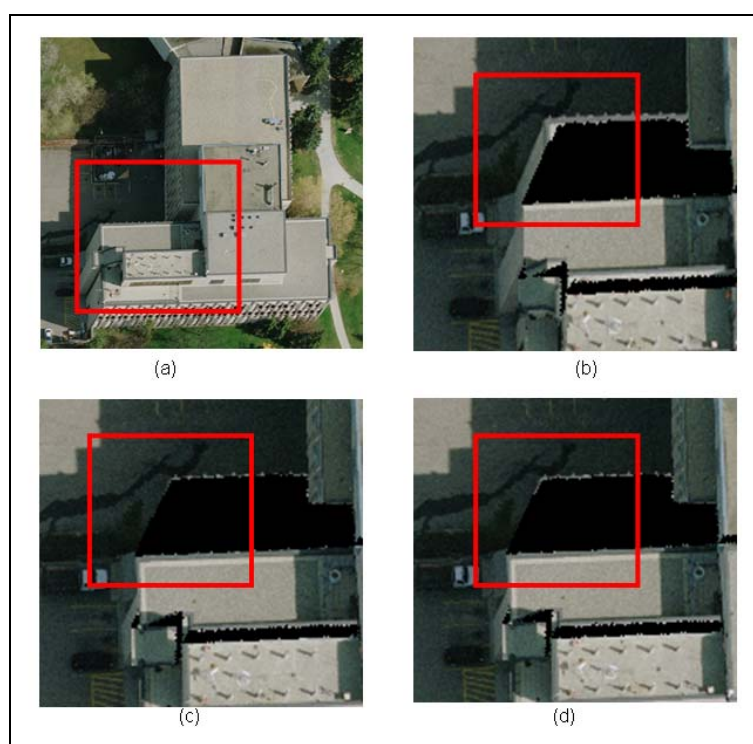


Figure 3.1: Perspective image (a), and orthoimage using the geo-referencing parameters using GCPs (b), LiDAR patches (c), and LiDAR lines (d), as the source of control (Habib et al., 2008c).

Since LiDAR footprints are irregularly distributed, it is almost impossible to assume point-to-point correspondence between photogrammetric and LiDAR data. Geo-referencing techniques that involve a coplanarity constraint while utilizing LiDAR linear and areal features were proposed by Habib et al. (2006b). In their research, the coplanarity constraint was added to existing bundle adjustment procedures. Alternative geo-referencing techniques that use existing point-based bundle adjustment procedures and incorporate linear and areal features were introduced by Habib et al. (2008c). These techniques simply manipulate the weight matrices associated with the points belonging to these features without modifying the bundle adjustment procedures, compared to Habib et al. (2006b). The extraction of linear and areal features from irregular LiDAR points is done through a semi-automatic process. First, an operator selects areas in which areal and linear features might be present, by looking at the LiDAR intensity images (which are used for visualization purposes only). Then, a segmentation technique (Kim et al., 2007) is used to cluster LiDAR points belonging to planar patches. For linear feature extraction, adjacent planar patches are identified and intersected to produce straight line segments. Figure 3.2 shows examples of LiDAR point cloud extracted for the areas selected by an operator (a), segmented planar patches (b), and a straight line segment derived through the intersection of two neighbouring planar patches (c).

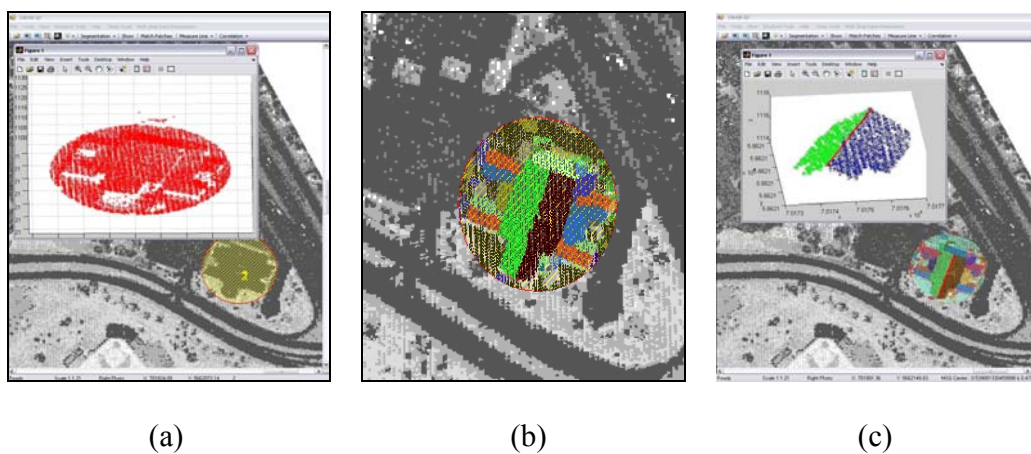


Figure 3.2: LiDAR point cloud extracted for the area of interest selection (a), segmented planar patches (b), and linear features extracted by intersecting two neighbouring planar patches (c) (Habib et al., 2008c).

Once the linear and areal features are extracted from the LiDAR data, the focus will be shifted towards the incorporation of these features in photogrammetric geo-referencing. The techniques for this incorporation are designed to restrict the weight matrices for the points representing lines and planar patches. As a mathematical model, the well-known collinearity equations are used in these techniques. More detailed explanations follow in Sections 3.3.1 and 3.3.2.

3.3.1 Point-based incorporation of linear features

Here, geo-referencing is carried out by incorporating linear features in photogrammetric triangulation. Image and object space lines are each defined by two end points, extracted from the image and object space, respectively. There is no need for

correspondence between the image and object space points along the linear features, as shown in Figure 3.3. This is because the weight matrix of each image point involved is restricted in this approach. Only useful information along normal direction to the image space line is utilized. In other words, the point is free to move only along the image space line.

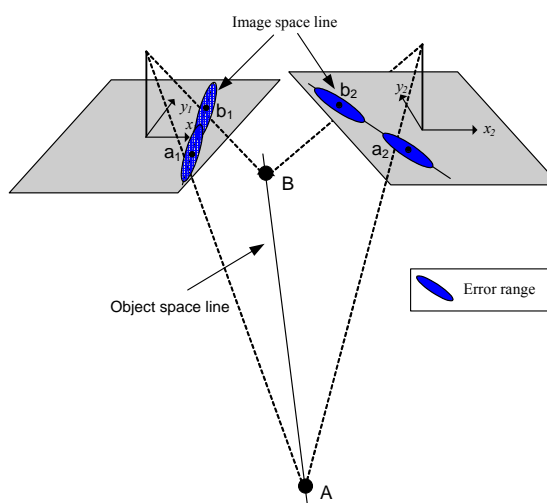


Figure 3.3: Representation of image and object space lines for the point-based incorporation of linear features (Habib et al., 2008c).

A matrix, R is a rotation matrix between the original (XY) coordinate system and the line (UV) coordinate system, in which the U axis is along the line (Figure 3.4 and Equation 3.1). Weight matrices with dimensions 2×2 can be used for weight restriction in the image space.

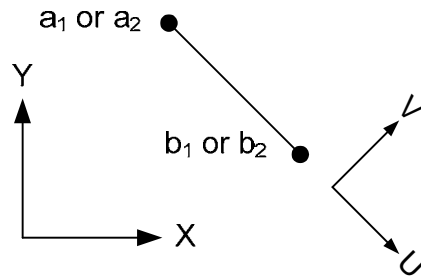


Figure 3.4: Image and line coordinate systems.

$$\begin{bmatrix} U \\ V \end{bmatrix} = R \begin{bmatrix} X \\ Y \end{bmatrix} \quad (3.1)$$

Where:

$\begin{bmatrix} U \\ V \end{bmatrix}$ is point coordinates in the line coordinate system;

R is the rotation matrix between the image and line coordinate systems; and

$\begin{bmatrix} X \\ Y \end{bmatrix}$ is point coordinates in the image coordinate system.

An explanation of the weight matrix restriction in the image space is as follows. The original weight matrix, P_{XY} , of a point is defined as the inverse of its variance-covariance matrix, Σ_{XY} , which depends on the image measurement accuracy. After applying the law of error propagation to Equation 3.1, the weight matrix of a point in the line coordinate system, P_{UV} , can be derived according to Equation 3.2.

$$P_{UV} = RP_{XY}R^T \quad (3.2)$$

Where:

P_{UV} is the weight matrix of the point in the line coordinate system and

P_{XY} is the weight matrix of the point in the image coordinate system.

Modification of the values in the computed P_{UV} matrix is done along the line direction. In other words, zero values are assigned to the weights along the line direction, as shown in Equation 3.3.

$$P'_{UV} = \begin{bmatrix} 0 & 0 \\ 0 & P_v \end{bmatrix} \quad (3.3)$$

Afterwards, the modified weight matrix, P'_{UV} , is propagated back to the image coordinate system, according to Equation 3.4.

$$P'_{XY} = R^T P'_{UV} R \quad (3.4)$$

Finally, the new weight matrix, P'_{XY} , can be applied in the point-based solution using the collinearity equation. The minimum requirement for linear control features to establish the geo-referencing parameters for the involved imagery is to have two non-coplanar lines (Ghanma, 2006).

3.3.2 Point-based incorporation of areal features

As another alternative for geo-referencing, an approach that incorporates areal features extracted from LiDAR data is introduced here. The vertices of conjugate patches should be observed in at least two overlapping images. The number of points selected in the corresponding LiDAR patch should be equivalent to the number of vertices defined in

the imagery. One should note that there is no need for correspondence between image and object space points, as shown in Figure 3.5. The weight matrix of each patch vertex in the object space is restricted in this approach. Only useful information along normal direction to the object plane is utilized. In other words, the point is free to move only along the object plane.

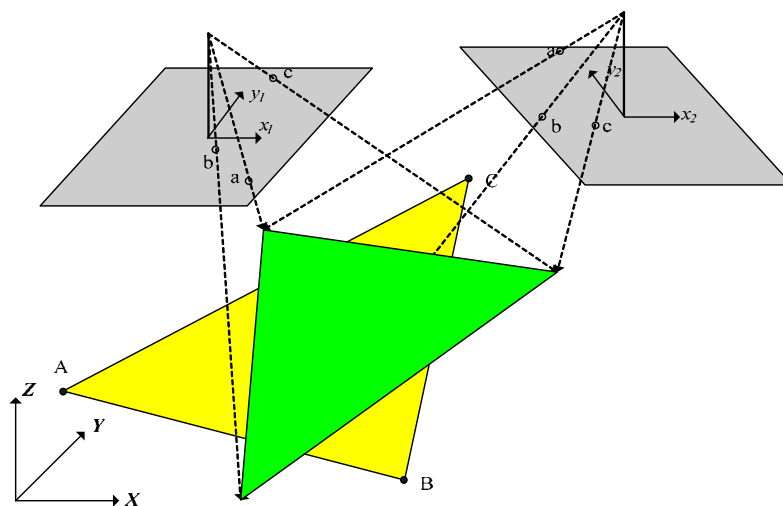


Figure 3.5: Representation of corresponding patches in the image and object spaces

(Habib et al., 2008c).

A matrix, R is a rotation matrix between the original (XYZ) coordinate system and the local plane (UVW) coordinate system, in which the U and V axes are aligned along the plane (Figure 3.6 and Equation 3.5).

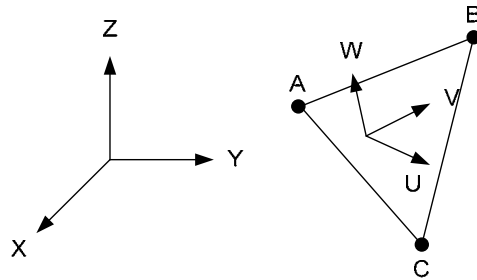


Figure 3.6: Object and plane coordinate systems.

$$\begin{bmatrix} U \\ V \\ W \end{bmatrix} = R \begin{bmatrix} X \\ Y \\ Z \end{bmatrix} \quad (3.5)$$

Where:

$\begin{bmatrix} U \\ V \\ W \end{bmatrix}$ is point coordinates in the plane coordinate system;

R is the rotation matrix between the object and plane coordinate systems; and

$\begin{bmatrix} X \\ Y \\ Z \end{bmatrix}$ is point coordinates in the object coordinate system.

The original weight matrix, P_{XYZ} , of a point is defined as the inverse of its variance-covariance matrix, Σ_{XYZ} , which depends on the specified accuracy of the LiDAR data.

After applying the law of error propagation to Equation 3.5, the weight matrix of the point in the local coordinate system, P_{UVW} , can be derived according to Equation 3.6.

$$P_{UVW} = RP_{XYZ}R^T \quad (3.6)$$

Where:

P_{UVW} is the weight matrix of the point in the plane coordinate system and

P_{XYZ} is the weight matrix of the point in the object coordinate system.

Modification of the values in the computed P_{UVW} matrix is then done. Specifically, zero values are assigned to the weights along the planar patch, as shown in Equation 3.7.

$$P'_{UVW} = \begin{bmatrix} 0 & 0 & 0 \\ 0 & 0 & 0 \\ 0 & 0 & P_w \end{bmatrix} \quad (3.7)$$

Afterwards, the modified weight matrix, P'_{UVW} , is propagated back to the object coordinate system, according to Equation 3.8.

$$P'_{XYZ} = R^T P'_{UVW} R \quad (3.8)$$

Finally, the new weight matrix, P'_{XYZ} , can be applied in the point-based solution using the collinearity equations. The minimum requirement for areal control features to establish the geo-referencing parameters for the involved imagery is to have four planar patches (three patches parallel to the planes XY, YZ, and ZX, respectively and an opposite patch in one of the planes XY, YZ, or ZX). However, the probability of having vertical patches in airborne LIDAR data is not high. Therefore, instead of working with vertical patches, one can use tilted patches with different orientations (Ghanma, 2006).

3.4 Rectification and Visibility Analysis

Once the photogrammetric dataset has been aligned to the reference frame of the LiDAR data, the image spectral and LiDAR positional information from the two datasets are ready to be linked to one another in the orthophoto generation process. One should note that orthophoto production aims to relate the image spectral and LiDAR positional information correctly through the elimination of sensor tilt and terrain relief effects from the captured perspective imagery. Differential rectification has been widely used for orthophoto generation (Konecny, 1979; and Novak, 1992). When dealing with large scale imagery over urban areas, however, differential rectification produces significant artifacts in the form of double mapped areas at the vicinity of abrupt surface changes (Skarlatos, 1999). A real example of the double mapping problem is illustrated in Figure 3.7, in which a perspective image and the corresponding generated orthophoto are shown.

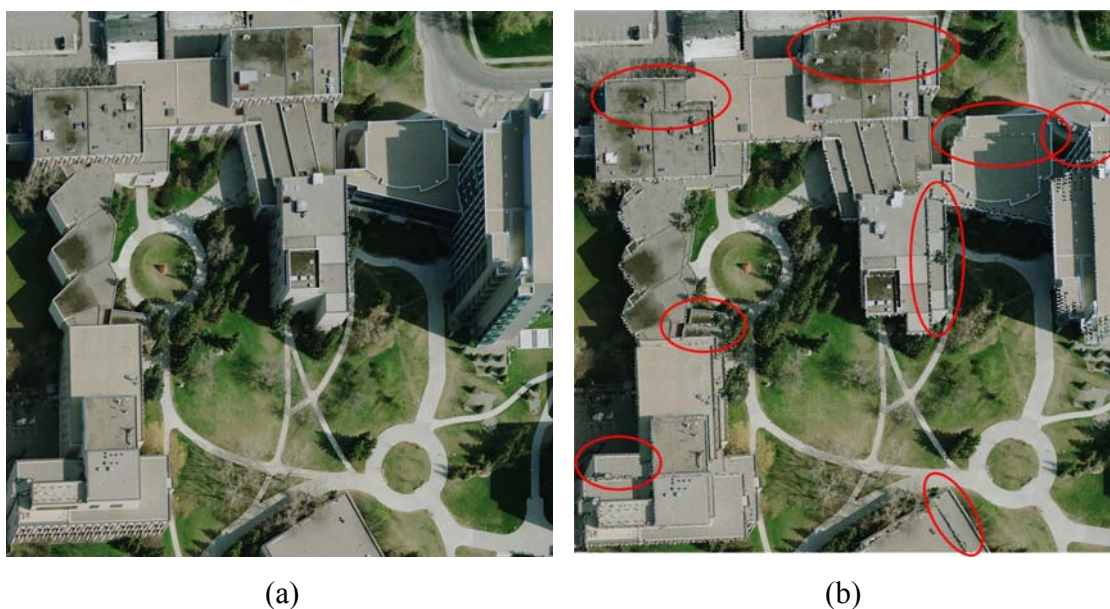


Figure 3.7: Perspective image (a) and corresponding orthophoto with double mapped areas around buildings (b).

As can be seen in Figure 3.7(a), the vertical structures have significant relief displacements that cause considerable occlusions in the object space. The generated orthophoto in Figure 3.7(b) shows that the relief effects along the building facades have been removed. However, double mapped areas (enclosed by red ellipses) occupy occluded portions of the object space. Double mapped areas constitute a severe degradation and are a major obstacle to the interpretability of the generated orthophoto. Therefore, true orthophoto generation methodologies focus on the elimination of the double mapped areas. The basic principle of these methodologies is the identification of occluded areas, which are caused by relief displacements associated with vertical structures in the object space.

True orthophoto generation is mainly concerned with visibility analysis, which has been studied in computer graphics, computer vision, photogrammetry, remote sensing, and telecommunications, as discussed in Chapter 2. To overcome false visibility and false occlusion problems associated with current true orthophoto generation techniques mentioned in the chapter, two alternative methods, which can be categorized as angle-based true orthophoto generation methods, are introduced in this research.

In an orthogonal projection, points are vertically dropped onto the datum. Therefore, when considering a vertical structure, its top and bottom are projected onto the same location without any relief displacement. However, in a perspective projection, the top and bottom of that structure will be projected as two points, which are spatially separated by the relief displacement. This displacement is expected to take place along a radial direction emanating from the image space nadir point (Mikhail, 2001). The radial

extent of the relief displacement is the source of occlusions/invisibilities in the perspective imagery. The presence of occlusions can be discerned by sequentially checking the off-nadir angles to the lines of sight connecting the perspective center to the DSM points along a radial direction starting from the object space nadir point. In the remainder of this section, the off-nadir angle to the line of sight will be denoted as the α angle (Figure 3.8).

Since there is no relief displacement associated with the object space nadir point, one can assure that this point will be always visible in the acquired image. As one moves away from the object space nadir point, it is expected that the α angle will increase gradually. As long as there is an increase in the α angle as one moves away from the nadir point, the DSM cells along the radial direction will be visible in the image in question. On the other hand, occlusions will take place whenever there is an apparent decrease in the α angle while proceeding away from the nadir point. This occlusion will persist until the α angle exceeds the angle associated with the last visible point. Figure 3.8 illustrates the mechanics of using the off-nadir angle to the line of sight in detecting occluded areas by considering a vertical profile through the perspective center. As can be seen in this figure, moving away from the nadir point will be accompanied by an increase in the α angle until one reaches the object point A , thus indicating that there is no occlusion up to this point. However, when considering the object point B , one would notice that α_B is smaller than α_A , which indicates that point B is occluded by A . For the object point C , it is obvious that α_C is greater than α_A , which indicates that C is visible.

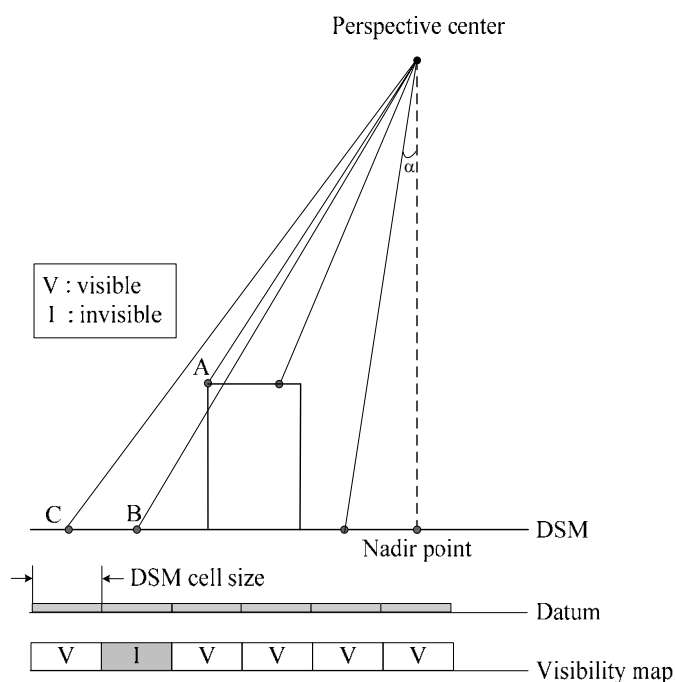


Figure 3.8: Using the off-nadir angle to the line of sight as a means of detecting occlusions.

In summary, the method of checking the α angle along a radial direction while moving away from the nadir point can be used for occlusion detection. Because such a method of occlusion detection does not incorporate the internal characteristics and attitude of the imaging sensor, its performance does not depend on the relative relationship between the DSM cell size and the GSD of the imaging sensor.

Adaptive Radial Sweep Method

As was mentioned before, the method of checking the α angle along radial directions from the nadir point can be used to identify occluded cells in the DSM. Radial sweep method considers individual cells in the DSM by scanning through the radial

directions from the object space nadir point. For example, one can start by considering the radial direction with zero azimuth (i.e., $\theta_0 = 0$ in Figure 3.9). After classifying the DSM cells along that direction, one would move to the next radial direction by incrementing the azimuth by a given value $\Delta\theta$. This process is repeated until the whole range of azimuth values has been considered. Occlusions detected along the radial directions can be stored in a visibility map with the same dimensions as the DSM. This map is initially set by switching off all the cells to indicate occlusion. During the radial sweep search, the visibility map cells corresponding to non-occluded DSM cells are switched on. Finally, the corresponding grey values for visible DSM cells are imported from the original image using traditional differential rectification. In this way, occluded areas will be left blank, thus producing a true orthophoto.

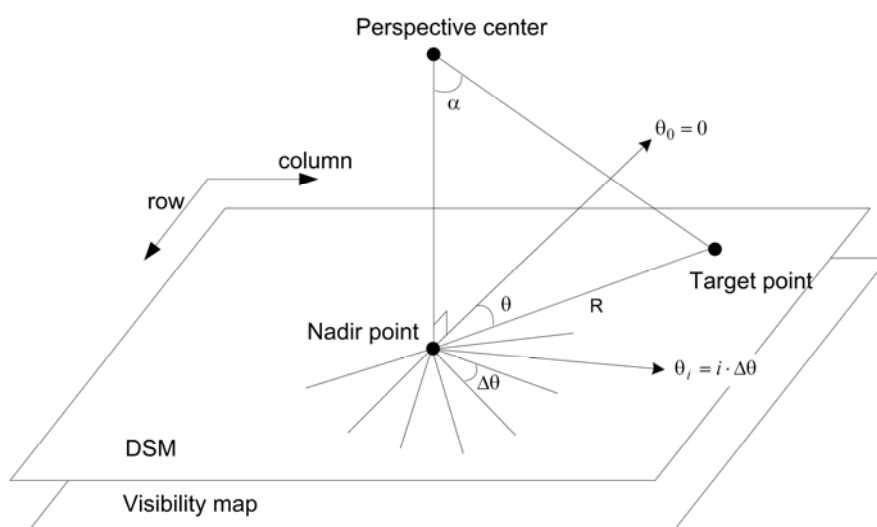


Figure 3.9: Conceptual basis of the radial sweep method of occlusion detection.

A critical decision in the implementation of the radial sweep method is the choice of the azimuth increment value ($\Delta\theta$). A small value will make the process time consuming and inefficient since the DSM cells close to the nadir point will be revisited repeatedly. On the other hand, coarse selection of the azimuth increment value will lead to non-visited cells at the DSM boundaries. To avoid this problem, an adaptive radial sweep method is proposed, in which the azimuth increment value is decreased gradually while moving away from the nadir point (Figure 3.10 and Figure 3.11).

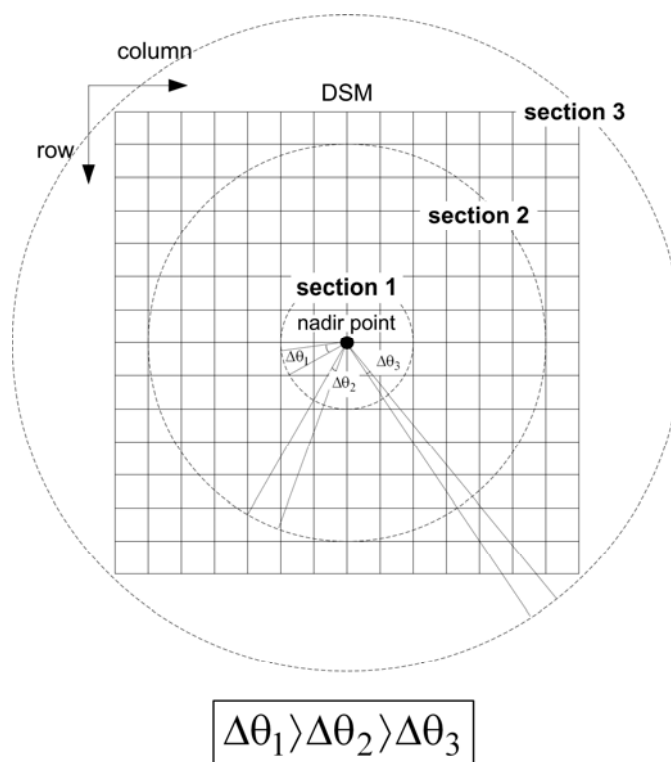


Figure 3.10: DSM partitioning for the adaptive radial sweep method (the azimuth increment value decreases as one moves away from the nadir point).

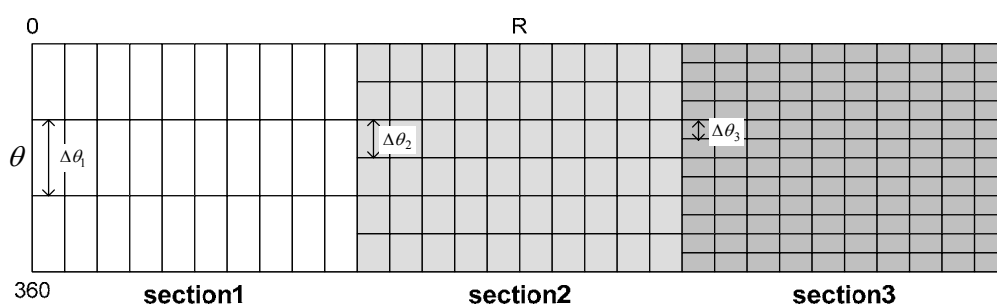


Figure 3.11: The R- θ array that corresponds to the partitioned DSM in Figure 3.10.

The implementation of the adaptive radial sweep method for occlusion detection and true orthophoto generation can proceed according to the following steps (a conceptual procedural flow can be seen in Figure 3.12):

1. Divide the DSM into concentric rings centered at the object space nadir point (Figure 3.10).
2. Using the sections defined in Step 1, define an R- θ array, as shown in Figure 3.11, where R indicates the radial distance from the nadir point and θ is the corresponding azimuth for a given DSM cell. The R- θ array will be used to store the α angle associated with each of the DSM cells. The pixel size in the R-direction can be chosen to be equivalent to the DSM pixel size. In the R-direction, the array is divided into sections that correspond to those defined in the previous step. Since different sections use different azimuth increment values, the number of rows in the array increases as the radial distance increases. More specifically, the azimuth increment value should vary between sections to ensure that the majority of the DSM cells are visited without excessive repetition or gaps.

3. Define a visibility map with the same dimensions of the DSM grid. All the cells in the visibility map are switched off to indicate occlusion. Also, define two arrays with the same dimensions as the R- θ array. These arrays will be used to store the X and Y coordinates of the corresponding cells in the DSM.
4. For each of the cells in the DSM, compute the corresponding R, θ , and α values. One should note that the R and θ values might not correspond to an integer location in the R- θ array. Therefore, the α angle is stored in the closest R- θ array element. In the meantime, the corresponding X and Y coordinates are stored in the respective X and Y array elements.
5. After populating the R- θ , X, and Y arrays, proceed by checking the α angles in the R- θ array for a given azimuth value. Visible locations along this direction should be updated in the visibility map using the corresponding coordinates in the X and Y arrays.
6. Finally, import the grey values at visible DSM cells from the original image using the traditional differential rectification procedure. In this way, occluded areas will be left blank, thus producing a true orthophoto.

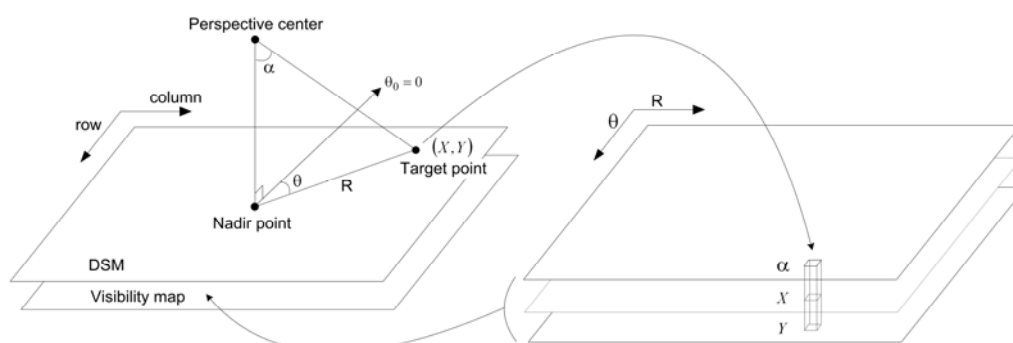


Figure 3.12: Conceptual procedural flow of the adaptive radial sweep method of occlusion detection.

One should note that the number of sections and their respective azimuth increment values will affect the efficiency of the adaptive radial sweep method and the storage requirements of this approach. To alleviate storage requirements while maximizing efficiency, the spiral sweep method has been developed, in which the DSM cells are swept in a spiral pattern starting from the nadir point.

Spiral Sweep Method

Similarly to the adaptive radial sweep algorithm, the spiral sweep method is an angle-based approach. However, the spiral sweep method scans the DSM cells starting from the nadir point in a spiral pattern while directly checking the α angles along the radial directions, without the need for DSM partitioning or additional arrays. The implementation of the spiral sweep method requires a visibility map and an α array with the same dimensions as the DSM grid. Initially, all the cells in the visibility map are switched off to indicate occlusion. The process begins by populating the α array while computing the off-nadir angle to the line of sight between the perspective center and each

DSM cell. Afterwards, the α array is swept in a spiral pattern, as shown in Figure 3.13. For each cell in the α array, the α angle is compared to the angle associated with the last visible point along the same radial direction from the nadir point. If the α angle of the cell in question is larger than the α angle of the last visible cell along the same radial direction, this cell will be considered to be visible, and the corresponding cell in the visibility map is switched on. Finally, the grey values for visible cells in the DSM are imported from the input image according to the differential rectification procedure.

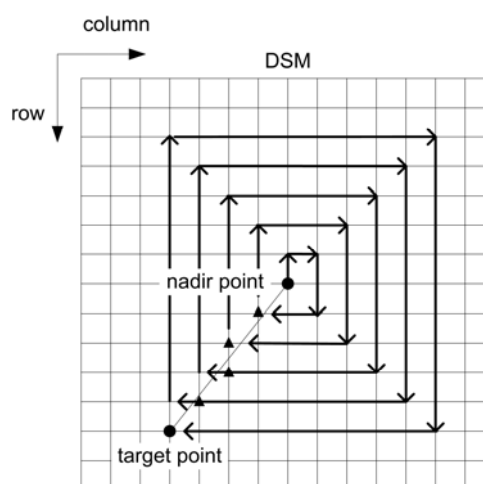


Figure 3.13: Conceptual procedural flow of the spiral sweep method of occlusion detection.

To verify that the angle-based approach overcome the drawbacks of the Z-buffer method, the visibility maps created using these methods are compared with each other for three different situations in Figure 3.14, Figure 3.15, and Figure 3.16. First, Figure 3.14(a) and Figure 3.14(b) show the visibility maps created using Z-buffer and angle-based methods when the DSM cell size is less than the GSD of the imaging sensor, respectively. In Figure 3.14(a), the DSM cell A which is closest to the projection center is

deemed visible, while the cells B, C, D, and E are incorrectly considered to be invisible. On the other hand, all the DSM cells in Figure 3.14(b) are correctly considered to be visible because the off-nadir angles of the DSM cells increase as one moves away from the cells A to E.

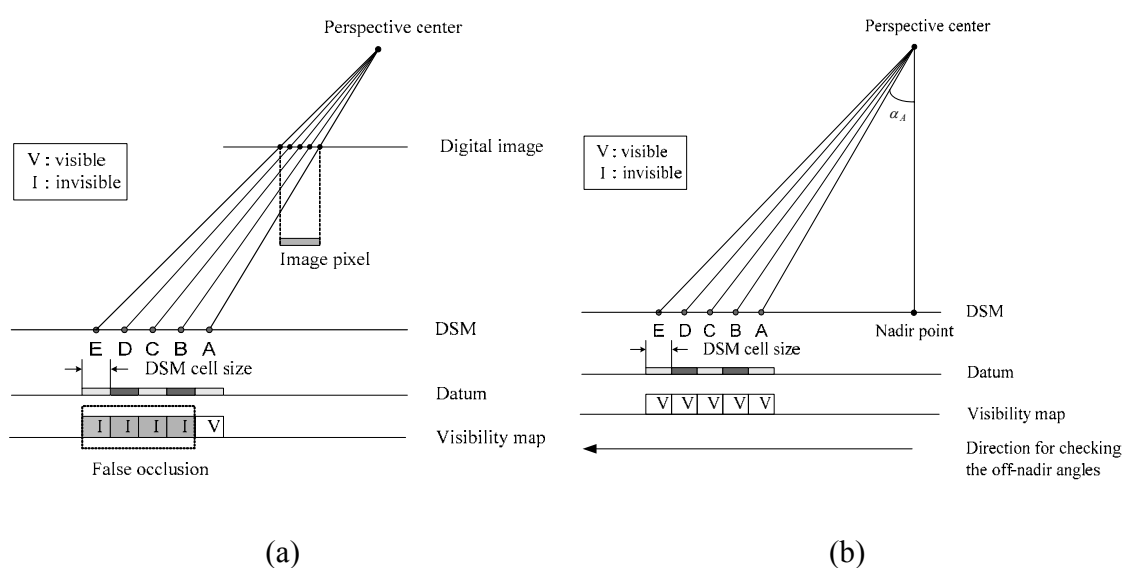


Figure 3.14: Visibility maps created using Z-buffer method (a) and angle-based approach (b) when the DSM cell size is less than the GSD of the imaging sensor.

Figure 3.15(a) and Figure 3.15(b) show the performance of the visibility analysis using Z-buffer and angle-based methods, respectively, when dealing with a DSM including terrain and above-terrain structures. The DSM cell size is chosen to be equivalent to the GSD of the imaging sensor at the terrain level. Figure 3.15(a) shows false visibility (at DSM cell E) in the occluded areas by vertical structures. The false visibility in the figure comes from having non-compatibility between GSD of the imaging

sensor at the building rooftops and DSM cell size. On the other hand, Figure 3.15(b) shows correctly detected occluded DSM cells D, E, and F and visible cells A, B, C, and G.

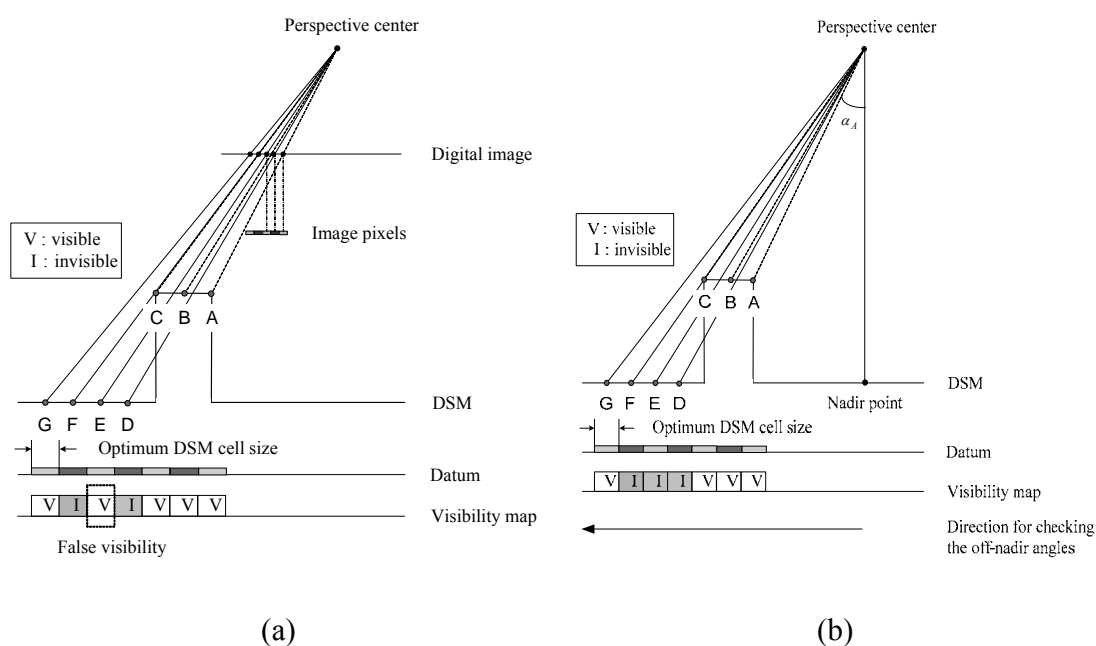


Figure 3.15: Visibility maps created using Z-buffer method (a) and angle-based approach (b) when the DSM size is chosen to be equivalent to the GSD at the terrain surface.

Figure 3.16(a) and Figure 3.16(b) show the performance of the visibility analysis using Z-buffer and angle-based methods, respectively, when dealing with a DSM including terrain and narrow vertical structures. Figure 3.16(a) shows false visibility in the occluded areas by vertical structures. The false visibility (known as M-portion problem) occurs because the cells C and D do not have any competition from points on

the building roof. On the other hand, Figure 3.16(b) shows correctly detected occluded DSM cells C, D, E, and F and visible cells A and B.

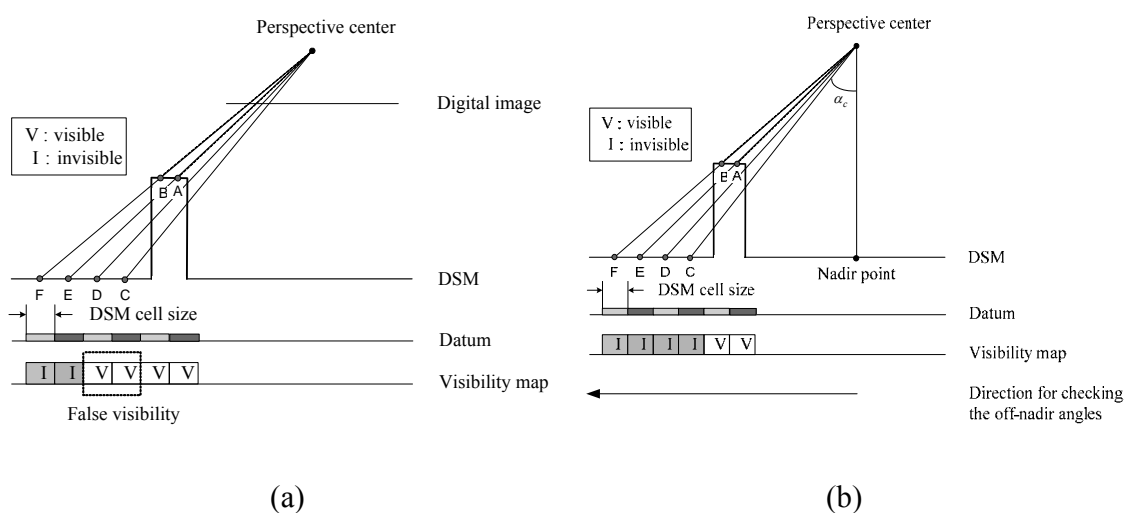


Figure 3.16: Visibility maps created using Z-buffer method (a) and angle-based approach (b) when a DSM includes narrow vertical structures.

The simulated DSM in Figure 2.5 has been used for occlusion detection through the implementation of the adaptive radial sweep and spiral sweep methodologies. Detected occlusions from the adaptive radial sweep and spiral sweep methods are shown in Figure 3.17(a) and Figure 3.17(b), respectively. A closer look at Figure 3.17 reveals that the detected occlusions from the developed methods are almost identical except for very small differences at the occlusion boundaries. These differences are the result of number rounding of the involved values to the nearest integer. Comparing the detected occlusions with those resulting from the Z-buffer technique (refer to Figures 2.7, 2.9, and 2.11), one can see improved results without false visibilities and/or occlusions.

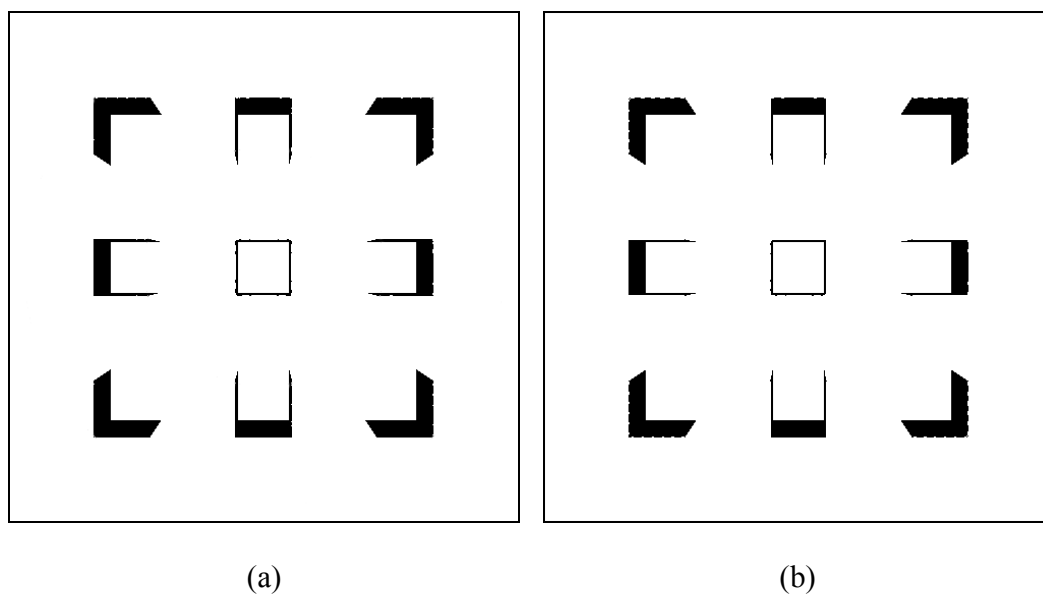


Figure 3.17: Detected occlusions from the adaptive radial sweep (a) and spiral sweep (b) methods using the simulated DSM in Figure 2.5.

Since the adaptive radial sweep and spiral sweep methods are both derived from the angle-based approach, the true orthophotos generated using these methods are almost identical. The execution time for generating orthophotos using the spiral sweep method is shorter than the time required for the adaptive radial sweep method, when large areas of interest are handled. On the other hand, it is the other way around in the case of relatively small areas of interest. Figure 3.18(a) shows real examples of true orthophotos generated using the adaptive radial sweep method. Also, an example of true orthophoto using Z-buffer method is shown in Figure 3.18(b). The black portions in Figure 3.18(a) and Figure 3.18(b) indicate detected occlusions that are due to relief displacement at the building locations (also refer to Figure 3.7(b)). To compare the true orthophoto results from the adaptive radial sweep method and Z-buffer method more carefully, the enlarged

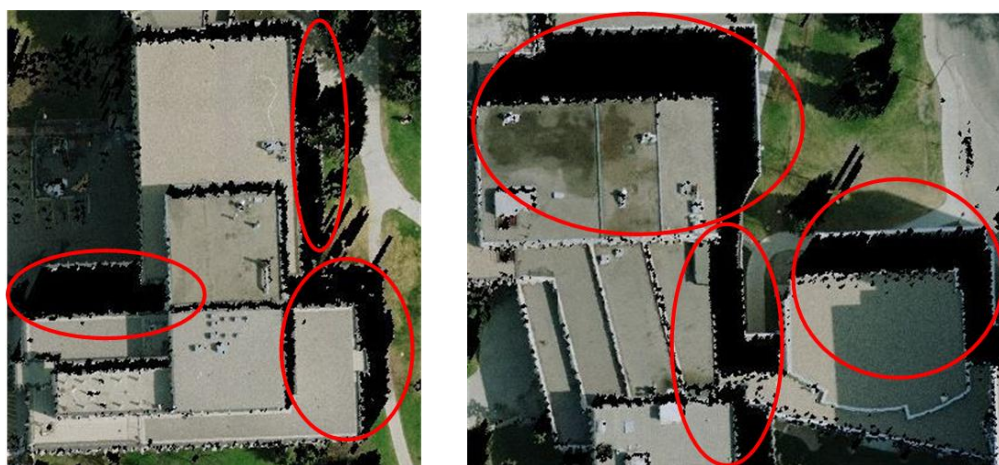
areas in the true orthophotos created using the methods are shown in Figure 3.19(a) and Figure 3.19(b), respectively. The true orthophotos produced using the adaptive radial sweep method do not introduce any false visibility or occlusions. On the other hand, the true orthophoto produced using Z-buffer method still has false visibility in the double mapped areas. Some of buildings have less false visibility and some have more because this method is sensitive to the relative relationship between the DSM and the image GSD. Figure 3.20 (a) shows the true orthophoto (based on adaptive radial sweep method) after filling occluded cells using overlapping images. The true orthophoto generated is draped on top of the DSM to produce the 3D visualization of the surfaces in Figure 3.20 (b).



(a)

(b)

Figure 3.18: A true orthophoto generated using adaptive radial sweep method (a) and a true orthophoto generation using Z-buffer method (b).

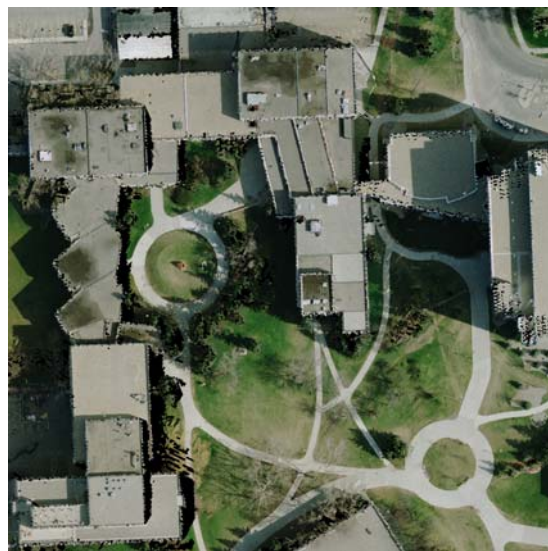


(a)



(b)

Figure 3.19: Enlarged areas in the true orthophotos created using adaptive radial sweep method (a) and using Z-buffer method (b).



(a)



(b)

Figure 3.20: A true orthophoto (based on the adaptive radial sweep method) after filling the occlusions using overlapping images (a) and 3D perspective view after draping the generated true orthophoto on top of the DSM (b).

One should note that Figure 3.18 (a) and Figure 3.20 are real examples of the preliminary 2D and 3D visualizations shown in the proposed framework diagram (Figure 1.1) in Chapter 1. The surface descriptions from the preliminary 2D and 3D visualizations created using the proposed true orthophoto generation methods are of improved quality and value, compared to those created using the current popular technique (Z-buffer method). However, a closer look at the products (produced using the proposed true orthophoto generation method) indicate that they are not yet of sufficient quality for the purpose of this research. Figure 3.21 shows the degraded quality near building boundaries in the true orthophotos produced. Furthermore, the effects of small features (such as cars, sculptures, and trees), which are not properly represented by the LiDAR-based DSM, on the quality of the true orthophoto are exemplified in Figure 3.22. Such degradation is an obstacle to the proper interpretation of the 2D/3D products generated. Due to the irregular and sparse nature of LiDAR data, it is almost impossible to have enough LiDAR points reflected from the exact building boundaries and small features. Hence, the DSM produced using the LiDAR points does not represent building boundaries and small features sufficiently.



Figure 3.21: Jagged building boundaries due to the incompleteness of the DSM.



Figure 3.22: Low quality of the produced true orthophoto around small features (e.g., cars, sculptures, and trees) due to the incompleteness of the DSM.

At this stage, it is quite important to mention that such degradation arises due to incomplete surface models, not from the proposed methodologies. In other words, the methodologies proposed to relate the image spectral and the LiDAR positional information have reliable performance; however, the positional information utilized does not represent breaklines well. To achieve the goal of this research, which is better surface description, Chapters 4 and 5 will focus on the enhancement of the surface models.

3.5 Summary

This chapter first presented the prerequisites for utilizing both photogrammetric and LiDAR data. Quality assurance and control of photogrammetric and LiDAR data were conducted to acquire photogrammetric and LiDAR datasets with reliable quality. Afterwards, co-registration was conducted to register both of the datasets to a common reference frame. Highly reliable co-registration results were achieved by utilizing LiDAR data as a source of control for photogrammetric geo-referencing. In this procedure, linear and areal features derived from LiDAR data are incorporated.

Two angle-based true orthophoto generation methods (the adaptive radial sweep and spiral sweep methods) were proposed to overcome problems such as false visibility and false occlusions that arise from the use of current methodologies. Moreover, the proposed methods do not require the incorporation of the internal characteristics and attitude of the imaging sensor for visibility analysis. Thus, their performance does not depend on the relative relationship between the DSM cell size and the GSD of the imaging sensor.

The quality of the 2D and 3D visualization products was also investigated. It was recognized that the degradation in the quality of the products was due to the incompleteness of the surface models, which was in turn caused by the limited LiDAR point resolution. Thus, to obtain better surface descriptions, methodologies for enhancing surface models will be investigated in Chapters 4 and 5.

Chapter 4 : Building Hypothesis and Primitive Generation

4.1 Introduction

In Chapter 3, the prerequisites for accurate data integration, which are quality assurance of photogrammetric and LiDAR data, quality control of photogrammetric and LiDAR data, and co-registration techniques were addressed. Once the photogrammetric and LiDAR have been aligned relative to the same reference frame, two methods of correctly relating image spectral and LiDAR positional information (the adaptive radial sweep and spiral sweep methods) were proposed. Through the investigation of the 2D and 3D visualization products that were generated from the procedures mentioned above, the problems caused by the incompleteness of the surface models were recognized. In other words, it was found that there is a lack of representation of features, mainly, breaklines (e.g., building boundaries in urban environments) due to the irregular and sparse nature of LiDAR data. Hence, there is a need to enhance the surface models by introducing precise building boundary information. DBM generation is usually performed in two steps: building detection and building reconstruction. Building detection is the process of generating the building hypothesis by differentiating buildings from other objects within the data. Building reconstruction, on the other hand, utilizes the hypothesized building regions in the data to derive its 3D representation (Ma, 2004).

Based on discussion mentioned above, the procedures for creating the enhanced surface models will be split into two parts and discussed in Chapters 4 and 5. This chapter will explain building hypothesis and primitive generation. The next chapter will discuss building reconstruction and enhancement of digital surface models, followed by

the refinement of the 2D and 3D visualization products. At this stage, one should note that the DBM generation method which will be proposed in this research is focusing on buildings with planar rooftops, which are bounded by straight lines (i.e., polyhedral building models).

Since elevation data is acquired directly by a LiDAR system, the degree of automation in building detection using this type of data is higher when compared to that using imagery (Brenner, 2005). Hence, this chapter discusses building detection through the manipulation of LiDAR data only. First, the classification of LiDAR data into terrain and off-terrain points is conducted in Section 4.2. The points classified as off-terrain points are then used to generate building hypotheses in Section 4.3. Finally, building primitive generation procedures that use the produced building hypotheses are discussed in Section 4.4.

4.2 Terrain/Off-terrain Point Classification

The building hypothesis generation procedure starts by classifying the LiDAR data into terrain and off-terrain points using an occlusion-based approach. The proposed methodology, like many other LiDAR classification techniques, is based on the assumption that there is a sudden elevation change at the transition between terrain and off-terrain points. The majority of existing techniques (as discussed in Chapter 2) detect these sudden changes by inspecting the slope or height differences within locally defined neighbourhoods. The size of these local neighbourhoods has a significant impact on the quality of the point classification. To overcome this sensitivity to the neighbourhood size, the proposed methodology utilizes a photogrammetrically-based global operation for

detecting sudden elevation changes. More specifically, the conceptual basis of the introduced methodology is that sudden elevation changes will cause relief displacements (i.e., leaning of vertical structures) in perspective views (Mikhail, 2001). The resulting relief displacement would, in turn, cause occlusions of nearby terrain points. Therefore, the presence of occlusions in perspective views can be used as an indication of the existence of occluding objects (i.e., off-terrain objects). The investigation of relief displacements and occlusion detection for true orthophoto generation (i.e., the angle-based approach) was discussed in Chapter 3. The main advantage of the angle-based methodology proposed in the previous chapter is that the occlusion detection procedure is performed in the object space. In other words, with the exception of the location of the projection center, the occlusion detection procedure is independent of the internal characteristics of the involved cameras and their orientation in space. The basic concept of the angle-based occlusion detection approach is extended to terrain/off-terrain classification of LiDAR data by introducing synthesized projection centers. This eliminates the need to simulate perspective views; hence it is only necessary to simulate the locations of the projection centers. Compared to the occlusion detection procedure which focuses on the identification of the occluded points (discussed in Chapter 3), the proposed terrain/off-terrain classification procedure focuses on the identification of the occluding points (i.e., the points causing the occlusion), which are hypothesized to be off-terrain points. A flow chart of the procedure is shown in Figure 4.1, and the step implementation details are discussed in the subsections that follow.

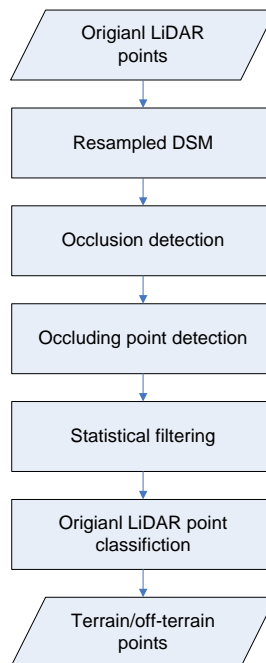


Figure 4.1: Flow chart for the terrain/off-terrain classification of the LiDAR points.

4.2.1 DSM generation

LiDAR systems deliver the 3D coordinates of points in an irregularly distributed cloud. The proposed occlusion detection method, however, is based on a regularly-spaced point cloud. Therefore, the first step of the proposed procedure is to resample the original point cloud onto a raster DSM. The resampling process should address two important issues: 1) the appropriate DSM cell size and 2) the most suitable interpolation technique. The cell size should be small enough to avoid loss of information during the resampling procedure. At the same time, the cell size should be large enough to avoid redundancy in the generated DSM. To satisfy these objectives, the cell size can be chosen to be equivalent to the average point spacing of the LiDAR point cloud. For optimal classification of the LiDAR data, the resampled DSM should not smooth the surface too

much, and should retain as well as possible the locations where sudden elevation changes take place. To satisfy these requirements, the nearest neighbour resampling approach is utilized because most of other methods (e.g., Kriging, Inverse Distance to a Power, Polynomial Regression, and Triangulation with Linear Interpolation) make the surfaces smooth without keeping abrupt changes of the elevations. The elevation at each DSM cell is defined as the elevation of the closest LiDAR footprint. Besides choosing the nearest point, the resampling procedure should consider the fact that multi-return LiDAR systems might provide several elevations at the same planimetric location. For instances in which multiple elevations are present for a given cell, the lowest elevation is picked and assigned to that cell. This elevation will be utilized in the final classification of the original LiDAR points.

4.2.2 Occlusion-based off-terrain point detection in the DSM

As mentioned in Chapter 3, the presence of a sudden elevation change in a DSM can be inferred by detecting the occlusion introduced by this elevation change using a projection center. In this procedure, occlusions can be discerned by sequentially checking the off-nadir angles, which are designated as “ α angles”, to the lines of sight connecting the projection center to the DSM cells, in a radial direction starting from the object space nadir point. Occlusions are present wherever there is a decrease in the off-nadir angle as one moves in a radial direction away from the nadir point.

In this work, detecting the presence of occlusions will be followed by identifying the occluding points (i.e., the points causing the occlusion), which will be hypothesized to be off-terrain points. The occluding points can be identified with the help of the

triangle formed by the first occluded point, the last visible point, and the projection center. The occluding DSM cells along the radial line connecting the nadir point and the first occluded point can be determined through a backward tracking procedure. Starting from the last visible point, backward tracking continues as long as the α angles of the DSM cells are equal to or greater than the off-nadir angle associated with the first occluded point. In other words, the occluding points consist of the DSM cells whose α angles are equal to or greater than the off-nadir angle of the first occluded point. Figure 4.2 illustrates the procedure for identifying the occluding points along a DSM profile. One should note that PC in the figure denotes perspective center.

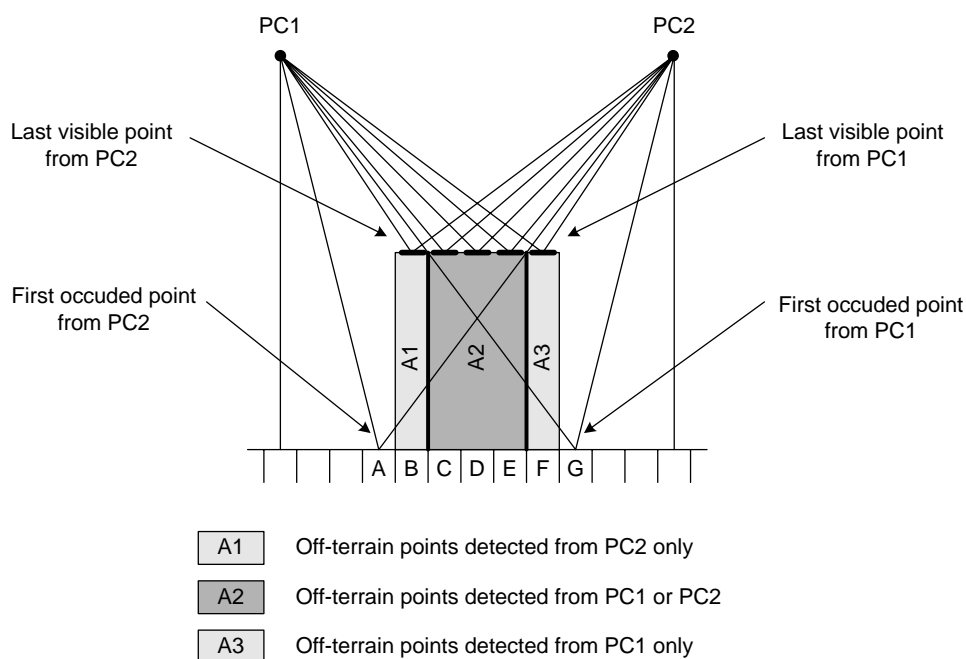


Figure 4.2: Occluding point detection using multiple projection centers (PCs).

In this figure, the DSM cell designated as “G” is the first occluded point detected using PC1 since $\alpha_G < \alpha_F$. Therefore, in the backward tracking process, cells F, E, D, and C are identified as occluding points (since the α angles for these points are larger than the off-nadir angle to the first occluded point – α_G) using PC1. Once backward tracking from the last visible point has been completed, the procedure continues checking the α angles along the profile in question, starting from the first occluded point, assuming that it is visible. If another occlusion is detected, another backward tracking process should commence. It should be noted that this procedure for the extraction of occluding points is valid in situations in which several off-terrain objects are occluding one another. However, as can be seen in Figure 4.2, for relatively large off-terrain objects, a situation might arise in which the backward tracking procedure will not be able to entirely recover the object using a single projection center. For example, in Figure 4.2, when using only PC1, the backward tracking procedure will stop at point C, so that point B is not detected as an off-terrain point. To avoid such a scenario, another projection center is used (e.g., PC2 in Figure 4.2). Using the second projection center, the backward tracking procedure will identify cells B, C, D, and E as off-terrain points. The final set of off-terrain points will consist of the aggregation of the off-terrain points identified using PC1 and PC2.

Having explained the concept of using synthesized projection centers to identify off-terrain points in an interpolated DSM, the necessary number and the locations of the synthesized projection centers should be discussed. The locations of the projection centers relative to the DSM should be established in a way that maximizes the occlusions introduced by these projection centers (i.e., by maximizing the differences between the off-nadir angles associated with the last visible and first occluded points). Since the

magnitude of the relief displacements and corresponding occlusions are inversely proportional to the height of the projection center above the terrain, one should place the projection centers as close as possible to the DSM. In this work, the heights of the projection centers are chosen to be slightly higher than the highest elevation in the DSM. The relief displacement for a given DSM cell is also directly proportional to the planimetric distance between that cell and the projection center. Therefore, the synthesized projection centers should be located at a certain horizontal distance away from the DSM. This distance should be determined in a way that ensures significant relief displacement at the DSM boundaries. Figure 4.3(a) and Figure 4.3(b) illustrate the impact of the vertical and planimetric location of the projection center relative to the DSM on the introduced occlusions. As shown in Figure 4.3(a), the lower projection center will provide wider occlusion areas than those from the higher projection center. Hence, the possibility that one can detect off-terrain points through the backward tracking process is higher in the case of the lower projection center compared to that of the higher one. Also, Figure 4.3(b) shows that the possibility of detecting off-terrain points is higher when the projection center has a longer radial distance compared to that with a shorter radial distance. Moreover, the impact of the location of the synthesized projection center on the close and distant buildings will be different. As seen in Figure 4.4, the impact of the location of PC1 on BLD2 is not significant compared to that on BLD1 because the radial distance between PC1 and BLD2 is much longer than the radial distance between PC1 and BLD1. In other word, the possibility of detecting off-terrain points on BLD2 will be very high regardless of the horizontal location (i.e., D in Figure 4.4) of PC1. Conversely, the possibility of detecting off-terrain points on BLD1 will be very high regardless of the

horizontal location of PC2. In summary, the location of the projection centers should be determined in a way that ensures a high possibility of detecting off-terrain points through the backward tracking process, while considering the discussion mentioned above. Also, the relatively lower possibility of detecting off-terrain points on the buildings near a projection center will be covered by the other projection centers.

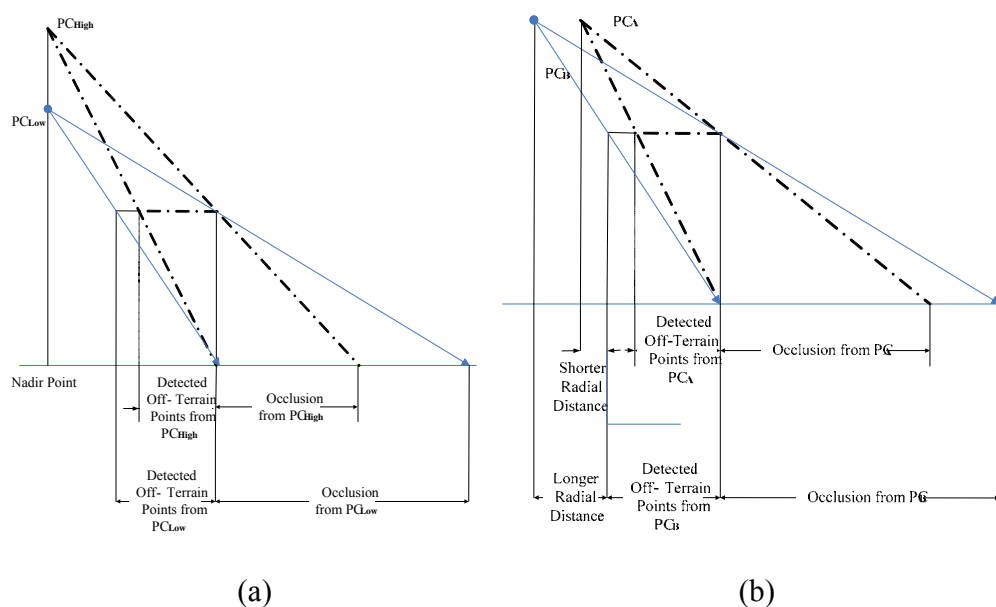


Figure 4.3: The impact of the vertical (a) and planimetric (b) location of the synthesized projection center on the extent of detected off-terrain objects.

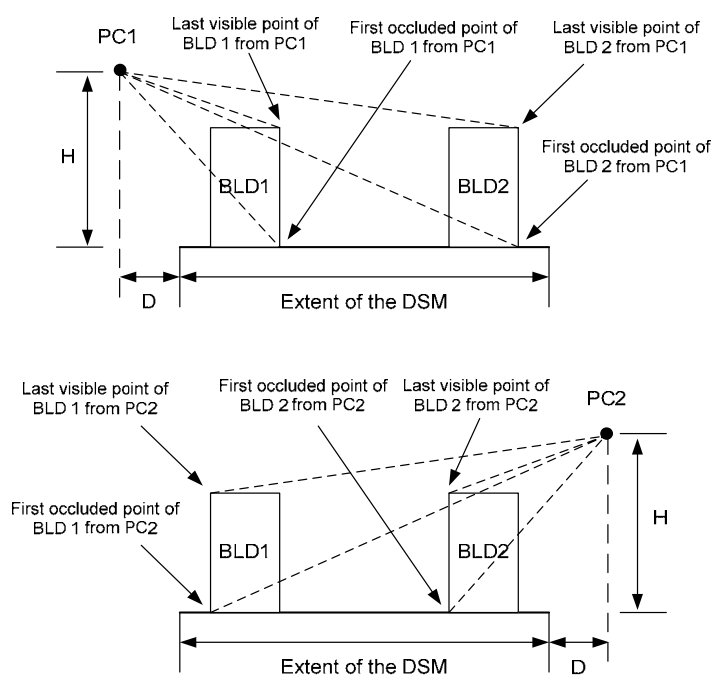


Figure 4.4: The different impact of the synthesized projection center on the close and distant buildings.

The remaining issue that should be addressed is defining the number of projection centers necessary for the detection of all occluding points. In a raster DSM, each cell has eight neighbours, any of which might occlude the cell. Therefore, a total of eight projection centers should be synthesized for each DSM cell. These projection centers should be placed relative to the DSM cell in a way that ensures backward tracking in each of the eight directions from the cell to its direct neighbours (these directions will be denoted as “cardinal directions” and will be given the labels 1 through 8). The optimal configuration of the synthesized projection centers for two DSM cells is shown in Figure 4.5. Opposite projection centers, which are located along the cardinal directions (1-5, 2-6, 3-7, or 4-8) can be used to check the occluding points for all the DSM cells along those directions. Thus, checking for occluding points can be carried out for all the DSM cells

along one profile at a time, Figure 4.6. By checking occluding pixels along each one of these profiles, one can check whether a given DSM cell is occluding neighboring points along these directions. In summary, the configuration of the synthesized projection centers for a given DSM will be similar to what shown in Figure 4.7

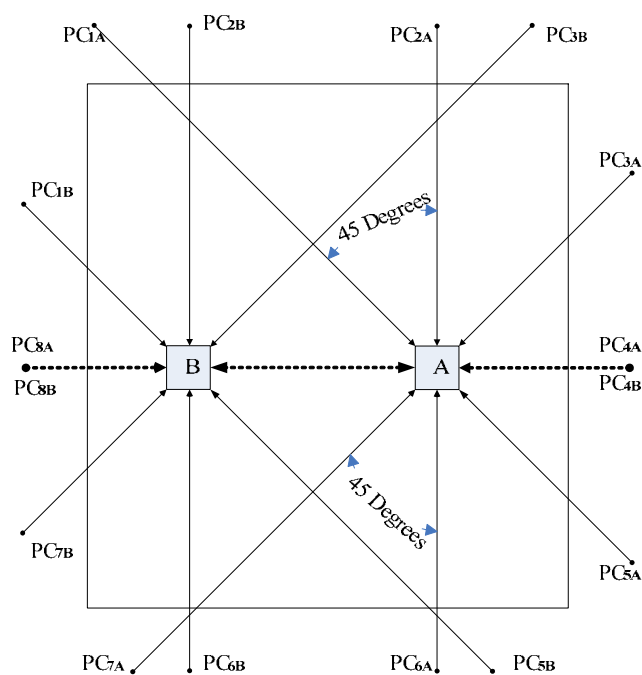


Figure 4.5: Optimal number of projection centers for two DSM cells (A and B).

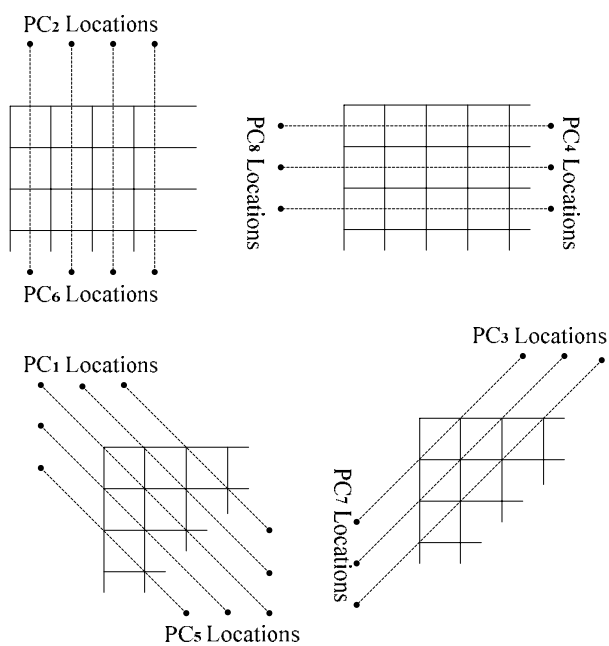


Figure 4.6: Checking all possible occluding directions for the DSM cells one profile at a time.

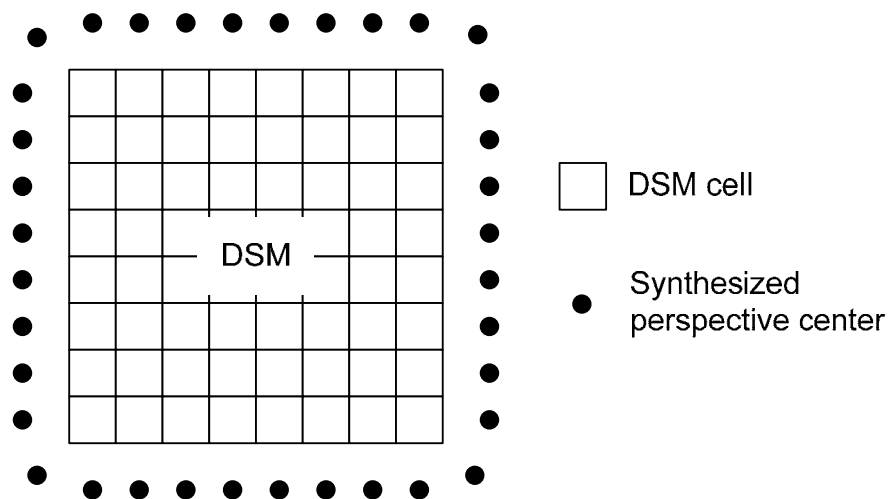


Figure 4.7: Chain of synthesized projection centers for a given DSM.

To illustrate the performance of the occlusion-based method for detecting off-terrain points in a DSM, the surface depicted in Figure 4.8(a) is simulated. The surface is composed of a sinusoidal terrain with a few man-made structures. Random noise has been added to the heights of the surface points. Hypothesized off-terrain points, which are causing occlusions, are shown in white in Figure 4.8(b), while terrain points are shown in black. As can be seen in this figure, the man-made structures have been correctly classified as off-terrain points. However, one can see that false off-terrain hypotheses are generated in the terrain area. These false hypotheses are caused by the noise introduced to the terrain surface, which lead to perceived occlusions and consequently false off-terrain hypotheses. Similarly to the noise effect, one can expect that high-frequency components of the terrain (e.g., cliffs) might cause some occlusions, leading to additional false off-terrain hypotheses. To remove these false hypotheses, the proposed procedure is augmented with a statistical filter to refine the classified points, as will be discussed in the next subsection.

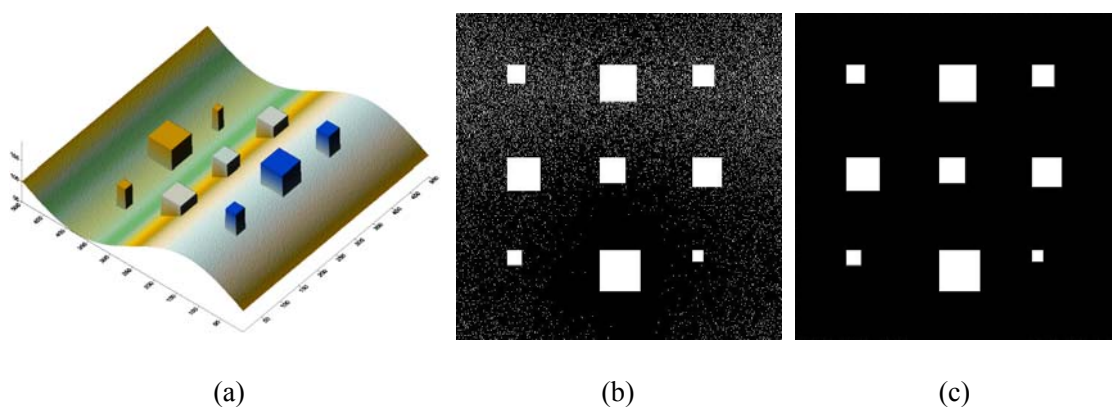


Figure 4.8: Simulated DSM (a), hypothesized off-terrain points (in white) before statistical filtering (b), and detected off-terrain points after statistical filtering (c).

4.2.3 Statistical filtering for the refinement of the classified points

As was mentioned earlier, surface roughness and noise lead to false hypotheses in the classification outcomes of the occlusion-based procedure. As it can be seen in Figure 4.8(b), false hypotheses are more prevalent in the hypothesized off-terrain points when compared with hypothesized terrain points. One might expect that the noise effect in off-terrain and terrain points should have the same effect (i.e., false terrain hypotheses should exist in the building areas as well as false off-terrain hypotheses in terrain areas). However, the locations and the configuration of synthesized projection centers lead to significant occlusions at the vicinity of buildings and other high objects. Such occlusions ensure the reclassification of false terrain points along building roofs. In other words, the backward tracking process will re-identify false terrain hypotheses along building roofs as occluding points. Therefore, the refinement of the occlusion-based classification algorithm will be based on the inspection of the elevations of classified off-terrain points, as compared to the heights of classified terrain points. More specifically, false off-terrain hypotheses will be corrected using a statistical filtering procedure, after using an appropriate probability distribution to represent the elevations of the hypothesized terrain points. Since terrain is relatively smooth, it is reasonable to assume that the terrain elevations in local neighbourhoods are normally distributed with a mean μ and a standard deviation σ . The elevations of terrain points within local neighbourhoods will be used to derive the mean and the variance of the corresponding distribution. To ensure that there are enough sample points for the reliable recovery of the statistical parameters of the terrain elevation within a given neighbourhood, the size of the neighbourhoods will be expanded until a predefined number of terrain sample points is identified in the local

neighbourhood in question (In this work, the predefined number of terrain sample points was chosen to be 100). The proposed procedure for statistical filtering is carried out as follows:

1. For each DSM cell, a local neighbourhood centered at that cell is defined. The size of this neighbourhood is expanded until enough terrain sample points have been identified.
2. The identified terrain sample points are used to derive an estimate of the statistical terrain parameters (μ_{terrain} and σ_{terrain}).
3. The height of the DSM cell (H_{cell}), its classified point type, and the estimated statistical parameters are utilized in the decision of whether to keep or refine this cell classification, according to the following rules:
 - a. If ($H_{\text{cell}} < \mu_{\text{terrain}} + 1.5 \sigma_{\text{terrain}}$), this point is classified as a terrain point, regardless of its original classification. The scaling factor of the standard deviation (1.5) is chosen since the probability of having a terrain point elevation that is less than $\mu_{\text{terrain}} + 1.5 \sigma_{\text{terrain}}$ is 93%, which is quite high.
 - b. If ($H_{\text{cell}} > \mu_{\text{terrain}} + 2.0 \sigma_{\text{terrain}}$), this point is classified as an off-terrain point, regardless of its original classification. The scaling factor of the standard deviation (2.0) is chosen since the probability of having a terrain point elevation that is larger than $\mu_{\text{terrain}} + 2.0 \sigma_{\text{terrain}}$ is 2%, which is quite low. In other words, the probability of a type I error is 2%.
 - c. If ($\mu_{\text{terrain}} + 1.5 \sigma_{\text{terrain}} < H_{\text{cell}} < \mu_{\text{terrain}} + 2.0 \sigma_{\text{terrain}}$), the original classification is maintained. In other words, there is no strong probabilistic basis for considering this cell to be either a terrain point or an off-terrain point.

4. The above procedure is repeated for each remaining DSM cell.

The above statistical procedure has been applied to refine the classification resulting from the occlusion-based procedure, shown in Figure 4.8(b). The refined classification is shown in Figure 4.8 (c). As it can be seen in the figure, all the false off-terrain hypotheses in the terrain area are correctly reclassified into terrain cells. The final stage of the proposed methodology utilizes the outcome of the statistical filtering to classify the original LiDAR points, as will be explained in the next subsection. One should note that results after the statistical filtering might be slightly different between one to the other according to different parameters used for the filtering process; however, the subsequent processes will take care of the difference of the results and end up with the same final products of this research.

4.2.4 Classifying the original LiDAR point cloud

So far, a procedure for the classification of points in a regularly spaced surface model (DSM) has been introduced. The DSM has been generated from irregularly spaced LiDAR points through a resampling procedure. The final stage of the proposed procedure uses the classified DSM points to categorize the original LiDAR point cloud into terrain and off-terrain points. The classification of the LiDAR points is based on their proximity to the classified DSM cells. In other words, if a LiDAR point lies within a given cell, then this point should have the same classification as that of the DSM cell.

As was explained in the resampling section, multi-return LiDAR systems might produce several elevation values at the same planimetric location. It should be noted that

the lowest LiDAR point has been utilized to resample the DSM. Therefore, if several LiDAR points lie within a cell that has been classified as an off-terrain point, then these points should all be classified as off-terrain. If several LiDAR points lie within a DSM cell that has been classified as a terrain point, then the lowest of these LiDAR points is classified as terrain. The classification of the remaining points depends on their height relative to the lowest LiDAR point. If the heights of the other points are significantly greater than the height of the lowest LiDAR point, then these points are classified as off-terrain points. In this work, the height difference threshold was chosen to be twenty centimetres.

To test the feasibility and the performance of the proposed procedure for terrain and off-terrain LiDAR point classification, several experiments using real data are conducted. A dataset including an area which has high frequency components in the terrain surface is selected (Figure 4.9 (a)). In detail, the dataset has complex tall buildings and a sudden elevation change along the terrain caused by tunnel entrances. As it can be seen in this figure, there are two roads extending into tunnels under the ground which are highlighted by ellipses in the middle and the bottom of that figure. Figure 4.9 (b) and Figure 4.9 (c) show the detected occluding points and classified off-terrain points after the occlusion-based and statistical filtering procedures. A closer look at Figure 4.9 (b) reveals that noise and high frequency components of the terrain (tunnel entrances) are causing false hypotheses of instances of off-terrain points (refer to the areas within the ellipses in Figure 4.9 (b) where off-terrain points are hypothesized at the tunnel entrances). Such false classification is expected since the high terrain points are occluding the low terrain points at the tunnel entrance. The statistical filtering rectified

this misclassification (refer to the areas within the ellipses in Figure 4.9 (c)). In other words, comparing the heights of the misclassified terrain points with the statistical properties of the neighbouring terrain points revealed the height proximity of these misclassified points to those associated with the correctly classified terrain points; thus leading to a reclassification of these points as terrain points. This result shows that the proposed methodology is quite successful in the classification of LiDAR point cloud including even high frequency components in the terrain surface. Figure 4.10 shows another example including complex and connected structures. Figure 4.10 (a) and Figure 4.10 (b) shows an aerial image patch and LiDAR data that covers the same area. Terrain (in blue) and off-terrain points (in red) in this area are identified through the proposed methodology and displayed in Figure 4.10 (c). The classified off-terrain points will be utilized to generate building hypothesis in the next section.

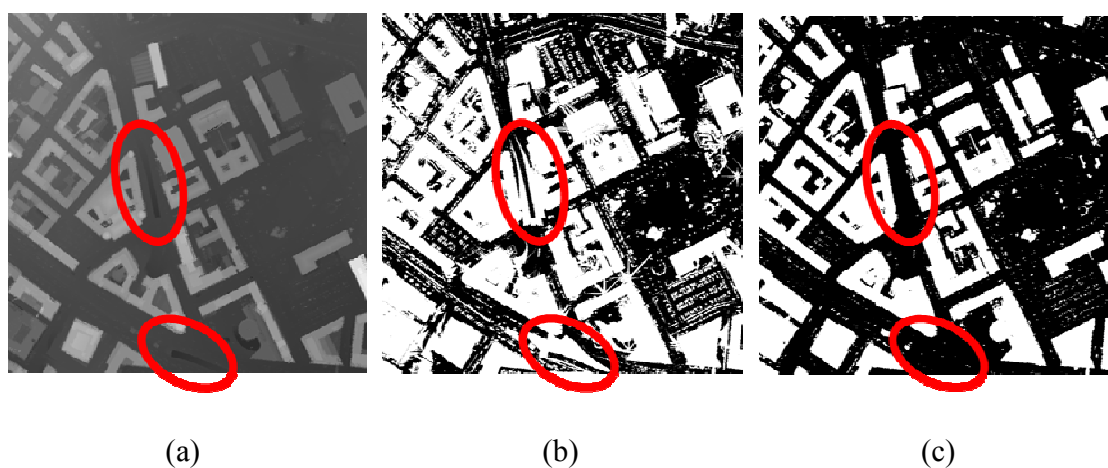


Figure 4.9: A dataset with high frequency components in the terrain surface (e.g., tunnels): resampled DSM (a), identified occluding points (b), and resulting off-terrain points after statistical filtering (c).

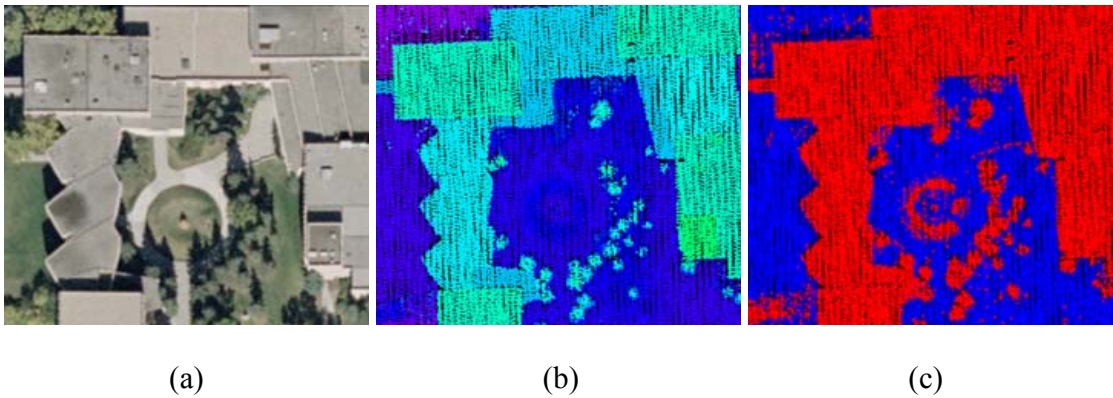


Figure 4.10: A dataset with complex and connected structures: aerial photo over the area of interest (a), LiDAR data that covers the same area (colors are assigned according to point elevations) (b), and classified terrain and off-terrain points (in blue and red, respectively).

4.3 Building Hypothesis Generation

Once the LiDAR point cloud has been classified into terrain and off-terrain points, classified off-terrain points are then used to generate building hypotheses. Recall that the target of this research is buildings with planar rooftops, which are bounded by straight lines. Figure 4.11 shows a flow chart of the procedures used to derive building hypotheses from off-terrain points while considering the target of this research.

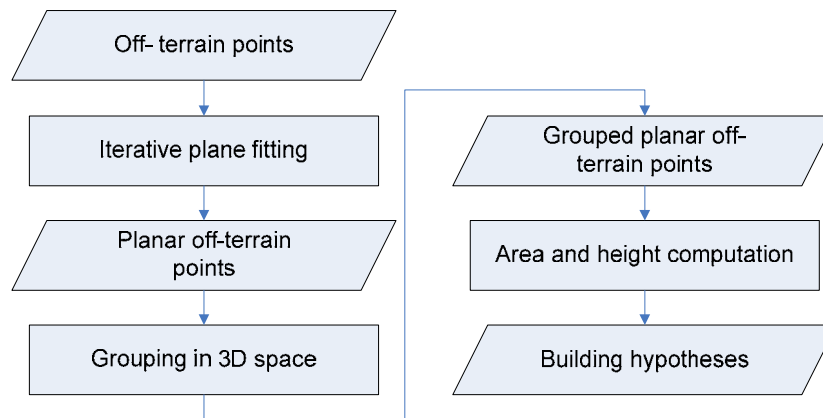


Figure 4.11: Flow chart of building hypothesis generation using off-terrain points.

Once the LiDAR point cloud has been separated into terrain and off-terrain points, the identified off-terrain points will be further classified into points belonging to planar surfaces and to rough surfaces. This classification process starts by establishing a spherical neighbourhood centered at each off-terrain point. Off-terrain points in this spherical neighbourhood are used to determine an initial fitted plane for the points in question, through a least squares adjustment procedure; the result is illustrated in Figure 4.12(a). After this first plane has been derived, the normal distances between the plane and the associated points are computed, as illustrated in Figure 4.12(a). The inverses of the normal distances are then used as weights for the next iteration of the plane fitting procedure. In other words, the farther the points are from the plane, the lower their weights will be. This procedure is repeated until plane parameter convergence (i.e., the plane parameters do not change from one iteration to the next) or the completion of a maximum number of iterations. After convergence, a buffer is defined above and below

the final fitted plane. The size of this buffer depends on the noise level expected in the LiDAR data; see Figure 4.12(b).

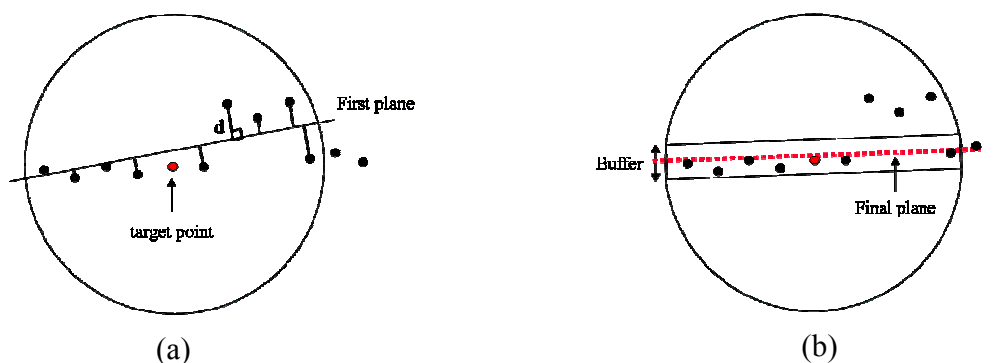


Figure 4.12: The first fitted plane for a spherical neighbourhood centered at an off-terrain point in question (a), and the final fitted plane derived through the iterative procedure using the inverses of the normal distances as weights (b).

The further point classification using the neighbouring LiDAR points is based on the ratio of the number of points within the buffer to the total number of points within the spherical neighbourhood. If the ratio exceeds a pre-defined threshold, then the central point will be classified as a point that belongs to a planar neighbourhood; see Figure 4.13(a). Otherwise, the point will be classified as part of rough surface; see Figure 4.13(b). It should be noted that if the iterative plane fitting procedure does not converge, the central point will be classified as belonging to a rough surface.

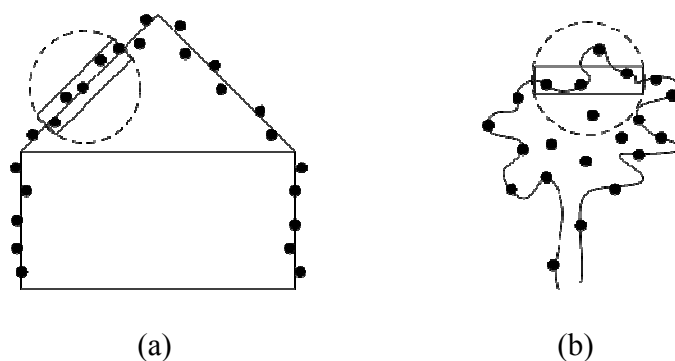


Figure 4.13: Majority of the points are within the plane buffer in case that the points belong to planar surface (a) and a few points are within the buffer in case that the points belong to rough surface (b) (side view).

At this stage, the most appropriate representation of plane while avoiding the main problem, which is the singularity of a given representation. For example, the equation, $X = aY + bZ + c$, cannot be used for planes parallel to the X-axis. Since buildings contain various planar patches with different slopes and aspects, this research introduces three different formulas for plane representation: 1) $X = aY + bZ + c$, 2) $Y = aX + bZ + c$, and 3) $Z = aX + bY + c$. First, all these plane representations are considered to derive the plane parameters for the points within the spherical neighbourhood. Since any type of plane representation with large condition number cannot have reliable plane parameters, such a representation is not considered as an appropriate model. Afterwards, using the remaining plane representations, the average of the squares of the distances between the off-terrain neighbourhood points and their corresponding projections onto the plane, along the normal to the plane, are computed. The plane representation equation providing the

lowest value is selected as the appropriate plane model for the neighbouring points in question.

So far, the identified off-terrain points are further classified into points belonging to planar surfaces and to rough surfaces. Afterwards, the points belonging to planar surfaces are grouped together according to their three-dimensional proximity. The points that are found to be spatially close to one another are grouped. A pre-defined threshold of two or three times the average point spacing of the LiDAR point cloud is utilized to determine whether the points are sufficiently close together to be grouped. The area and the height of the resulting groups relative to neighbouring terrain points will be used for building hypothesis generation with the help of thresholds that define the minimum area and height of the buildings in the study area. Figure 4.14 shows the building hypotheses generated using the identified off-terrain points in Figure 4.10(c). The different colors in this figure indicate different building hypotheses.

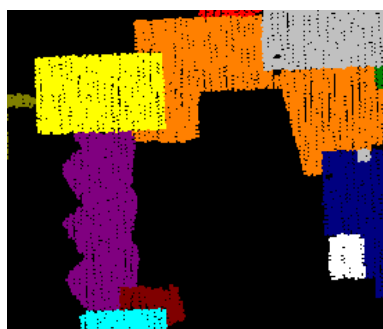


Figure 4.14: An example of building hypotheses generated through the proposed procedure.

A generated building hypothesis might be composed of several planar patches (e.g., compare the area in orange in Figure 4.14 and its corresponding areas in Figure 4.10(a)). This situation occurs when the closeness of the points on the different planes is less than the proximity threshold for grouping (Figure 4.15 (a)). Also, another situation might arise when a structure is formed by a series of connected planes with different slopes and aspects (Figure 4.15 (b)). Therefore, the next section proposes a segmentation procedures to break each building hypothesis down into a group of building primitives (i.e., the individual planar patches constituting a building rooftop).

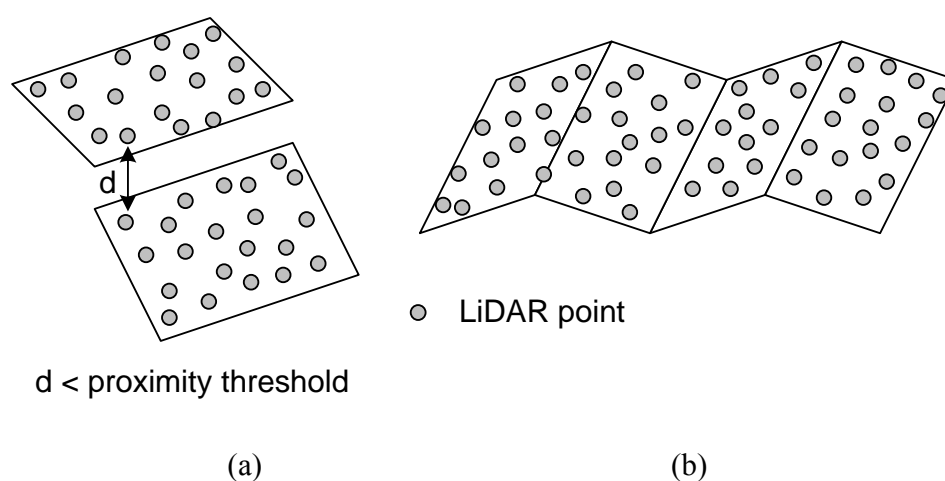


Figure 4.15: LiDAR points with the closeness less than a proximity threshold (a) and points on a structure formed by connected planes (b).

4.4 Building Primitive Generation

Building primitive generation begins with a segmentation procedure using the generated building hypotheses. This procedure is based on a voting scheme that keeps track of the point attributes, as defined by a local plane through its neighbouring points,

in an accumulator array. Afterwards, the modified convex hull procedure (Jarvis, 1977) is used to define the boundaries of the segmented planar patches. Figure 4.16 illustrates a flow chart of building primitive generation. Subsections 4.4.1 and 4.4.2 provide more detailed explanations of the segmentation and boundary generation procedures, respectively.

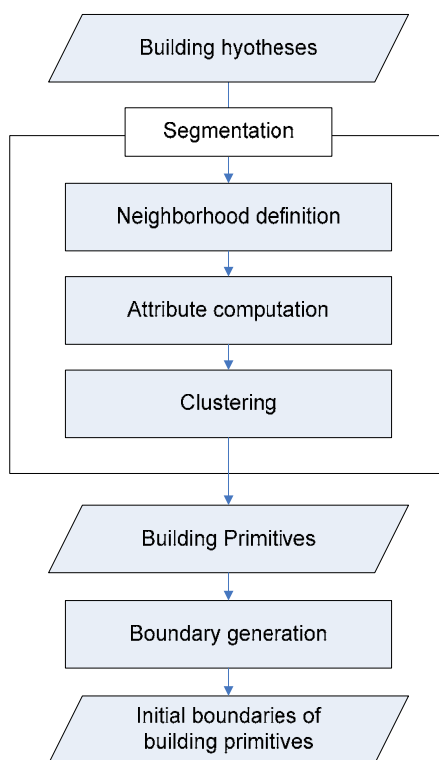


Figure 4.16: Flow chart of building primitive generation.

4.4.1 Segmentation

The segmentation method proposed will consider both the attribute similarity and the spatial proximity of LiDAR points while reducing the dimension of the attribute space. As shown in Figure 4.16, the segmentation procedure is composed of three sub-steps: 1) Neighbourhood definition; 2) Attribute computation; 3) Clustering of neighbouring points with similar attributes.

Neighbourhood definition

One should note that the attribute for a given point is defined by its neighbouring points and the way in which the neighbourhood of a LiDAR point is defined significantly affects the set of attributes computed for that point. Hence, the following paragraphs will discuss the appropriate neighbourhood definition to acquire useful attribute information. Three different types of neighbourhood definitions will be reviewed in this research. One way in which the neighbourhood of a point can be defined is by considering its proximity to other points that are projected onto the XY plane. The use of a TIN is the well known technique based on this neighbourhood definition. It has been used mainly for analyzing irregularly-distributed 3D points. However, serious drawbacks are revealed when points are located close to one another on the XY plane but are far from each other in the vertical direction. Figure 4.17(a) shows an example of neighbourhood definition using the TIN methodology; points on the ground and wall are considered to be neighbours of points on the roof. Another type of neighbourhood definition that can be used establishes proximity according to the Euclidian distance between points in 3D space. The points that are located inside a sphere of a certain radius centered at the point in question are

considered to be in its neighbourhood; see Figure 4.17(b). Even though three dimensional relationships between irregularly-distributed points are considered, points belonging to the wall are considered to be neighbours of points on the roof. Thus, the two neighbourhood definitions based on TIN and Euclidian distance in 3D space often include points belonging to different physical surfaces in the same neighbourhood.

Recall that the target of this research is buildings with planar rooftops, which are bounded by straight lines. Hence, the neighbourhood definition should take into account the physical shapes of objects (especially, planes) to acquire useful attributes for the target. A different definition which considers both the three-dimensional relationships between irregularly-distributed points and the physical shapes of surfaces is introduced and employed in this research (Filin and Pfeifer, 2005 and 2006). The physical shapes of the surfaces on which associated points are located are incorporated into the neighbourhood definition. This means that points located on the same surface are considered to be possible neighbours, while taking into account the proximity of the points. Points on different surfaces, on the other hand, are not considered to be neighbours, even if they are spatially close. This definition increases the homogeneity among neighbours. The definition starts by determining a cylinder whose axis is normal to the surface in question. The axis of the cylinder will be changed according to the orientaton of the surfaces. It is for this reason that this definition is referred to as the adaptive cylindrical neighbourhood. The schematic concept of the adaptive cylinder method, which follows this definition, is illustrated in Figure 4.17(c). As shown in the figure, points on the wall are not considered to be neighbours of the points on the roof. This neighbourhood definition method is implemented in a similar way as the plane

fitting procedure that is used for point classification using its neighbours in Section 4.3. Once the final plane is derived through the iterative plane fitting procedure, a cylinder will be defined by determining its axis, radius, and height. The axis will be normal to the final plane and the radius will be determined to include enough number of points to define reliable attributes. Also, the height will be determined by setting a buffer above and below the plane. The size of this buffer depends on the noise level expected in the LiDAR data. Finally, the neighbourhood will be defined by the points located inside the established cylinder; refer to Figure 4.12.

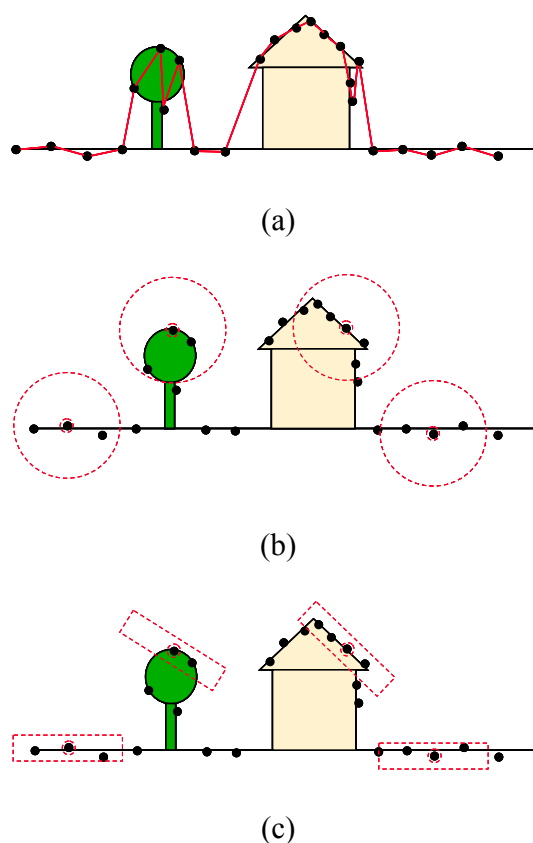


Figure 4.17: Different neighbourhood definition methods (side view): TIN (a), spherical (b), and adaptive cylinder (c).

Attribute computation

Point attributes are computed based on the neighbouring points identified using the defined neighbourhood. After introducing an origin, a plane is defined for each point using its neighbouring points. As illustrated in Figure 4.18, a normal vector from the origin to the plane is defined.

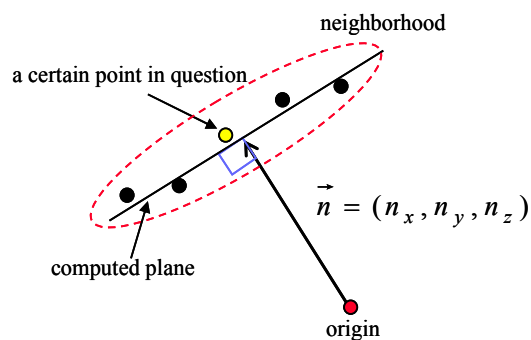


Figure 4.18: Vector defined from the origin to the computed plane for a given point, using its neighbouring points.

All techniques based on attribute clustering use a voting scheme with an accumulator array that is constructed in the attribute space. The dimension of the accumulator array depends on the number of the attributes utilized in the technique in question. The three components of the normal vector can be used as attributes in the voting scheme. One should note that one normal vector defines one infinite plane; therefore, planes sharing the same normal vector but disconnected in the object space will be clustered into one group. As mentioned before, this clustering approach ignores the proximity among points sharing similar attributes. Hence, none of the techniques based on this approach can be free from this problem.

The segmentation technique that uses the three components of the normal vector partitions points into distinct regions without any segmentation ambiguity except for that arising from co-planarity. However, the use of these attributes requires the construction of an accumulator array that has three dimensions, one for each vector component. A voting scheme that uses a three-dimensional accumulator array is computationally expensive. To reduce the three-dimensional accumulator array to two dimensions, the slopes of the normal vector in the x and y directions can be used instead of the three normal vector components as attributes for the planar patch segmentation (Elaksher and Bethel, 2002; and Filin and Pfeifer, 2006). Even though this method reduces the dimension of the accumulator array, the ambiguity of segmentation is a problem. If this method is used, parallel planes that have the same normal vector slopes in the x and y directions but different offsets in the z direction will be segmented as one group. This problem can be resolved through either spatial analysis of the data or the introduction of a one-dimensional accumulator array for the offsets in the z direction, after the segmentation in the two-dimensional attribute space is completed.

In this research, the magnitude of the normal vector (normal distance between origin and defined plane) is utilized as an attribute. One origin can be used for planar patch attribute computation. However, different planes with the same magnitudes of the normal vectors may exist. The tangent planes to a sphere centered on the origin are an example of this case. The points belonging to these planes will have the same attribute values. Therefore, two origins are introduced in this research; this significantly reduces the ambiguity that points belonging to planes with different slopes and aspects will have the same attribute values. Figure 4.19 (a) illustrate the situation that one origin is located

at an equal distance from the planes and the other origin is not. If one origin (origin 1) is located at an equal distance from the planes (i.e., $\|n_{11}\| = \|n_{12}\| = \|n_{13}\|$), the points belonging to these planes will have the same attribute values. Therefore, it would be impossible to separate these points into different groups in the attribute space. This problem can be resolved by introducing another origin (origin 2). The magnitudes of the normal vectors from the planes to the second origin will be different from one another (i.e., $\|n_{21}\| \neq \|n_{22}\| \neq \|n_{23}\|$). Hence, the points belonging to different planes will have different pairs of the attributes after introducing two different origins. These attributes will be utilized in the clustering procedure through the voting scheme. One should note that the number of origins determines the dimension of the accumulator array. If there is one origin for planar patch attribute computation, only a one-dimensional accumulator array is necessary for the voting scheme. Since two origins are introduced to reduce the possibility of the ambiguity mentioned above, two-dimensional accumulator array will be utilized in this research. Figure 4.19 (b) shows a diagram of the accumulator array for the points belonging to the planes in Figure 4.19 (a). All of these points are recorded in the accumulator array according to their attributes. As shown in Figure 4.19 (b), these points are recorded at the same location along the origin 1-axis. However, the points are recorded at the different locations along the origin 2-axis according to the planes that they belong to. The points belonging to the different planes will be recorded at the different locations in the two-dimensional accumulator array while avoiding ambiguity mentioned above.

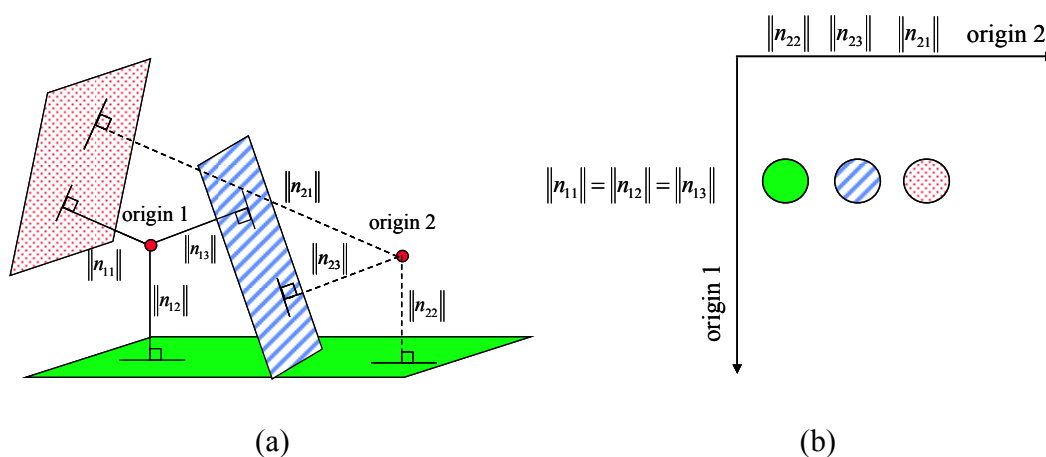


Figure 4.19: Situation that one origin is located at an equal distance from the planes and the other origin is not (a) and the recorded votes in two-dimensional accumulator array (b).

One should note that the utilization of two origins might still lead to ambiguities. Hence, the two origins should be located at positions that minimize the risk of ambiguity. Figure 4.20(a) shows an example of the ambiguity that causes the attribute vectors of different planes to be located at the same position in the accumulator array. The position of plane 1 in the attribute space is (n_1, n_2) ; n_1 and n_2 are the magnitudes of the normal vectors to plane 1 from the two origins. However, the other three planes share the same location in the attribute space. Although the likelihood of this ambiguity occurring in reality is very low, the possibility cannot be ignored. Therefore, this research suggests that the two origins be located such that the angle between the line connecting the two origins and the horizontal plane is 45 degrees; see Figure 4.20(b). This suggestion is based on the prior knowledge that the slopes of building roofs are less than 45 degrees, as most roofs are either horizontal or gently slanted. According to this assumption, planes 1

and 3 are almost nonexistent in reality because their slopes are greater than 45 degrees. By positioning the two origins in this manner, the possibility of ambiguity due to the locations of the origins is significantly reduced. To reinforce this statement, the possibility of the occurrence of ambiguity is calculated by performing a test with a real dataset containing forty two building hypotheses. The ambiguity occurred with only one hypothesis out of the forty two (about 2%). Even though the chance of an ambiguity occurring is extremely low after introducing two origins at the proposed positions, further processing has to be suggested to remove the ambiguity thoroughly. This additional processing is implemented in the clustering procedure. The methodology to derive coplanar points using these attributes follows.

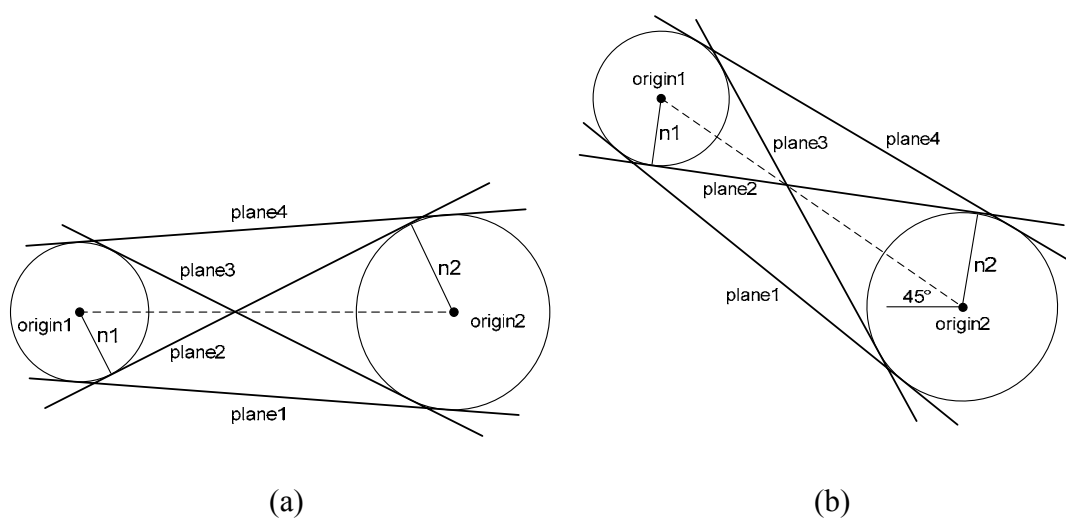


Figure 4.20: Ambiguity from two origins (side view) (a), and the positioning of two origins that minimizes the possibility of such ambiguity (side view) (b).

Clustering

Once the locations of the two origins are determined, the attributes for all the points in the dataset are computed and recorded in the accumulator array. Afterwards, clustering of points is conducted while considering proximity and coplanarity of the points. Figure 4.21 illustrates a flow chart of the clustering procedure proposed in this research. The points belonging to different planes in the object space are expected to form different accumulated peaks in the attribute space. Figure 4.22 shows an example of planar patch segmentation. A LiDAR dataset over a region that includes a building with two planar patches (e.g., gable roof) is selected; see Figure 4.22(a) and Figure 4.22(b). The points that belong to the patches produce two peaks in the accumulator array through the voting scheme; see Figure 4.22(c).

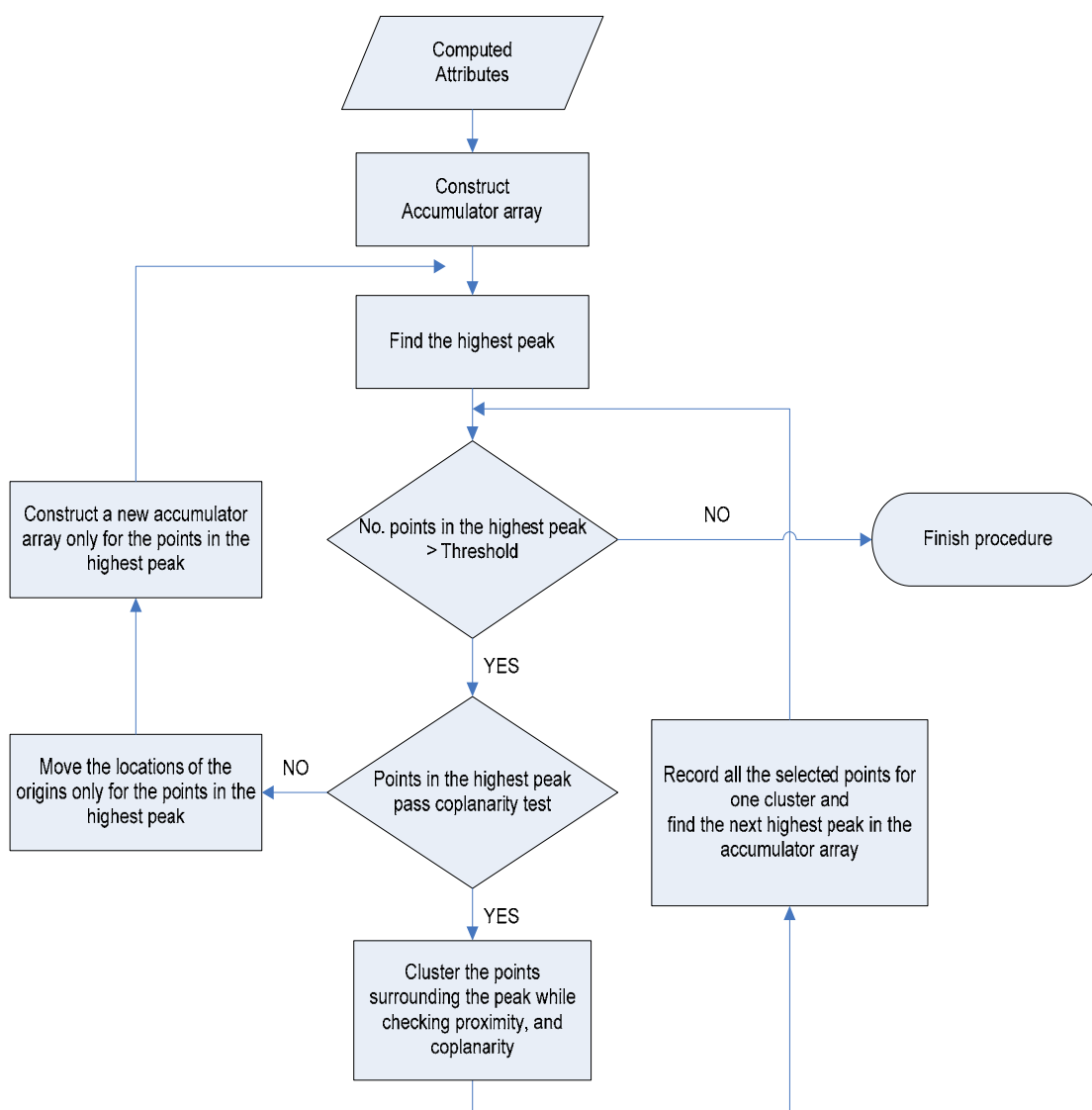
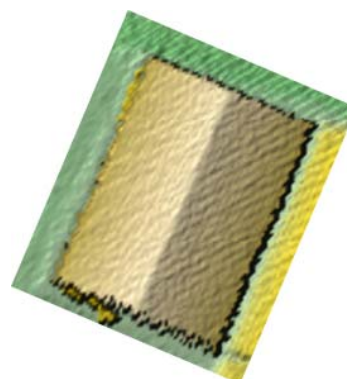


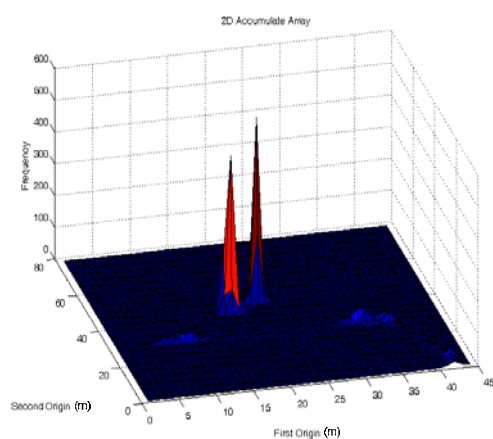
Figure 4.21: Flow chart of the clustering procedure.



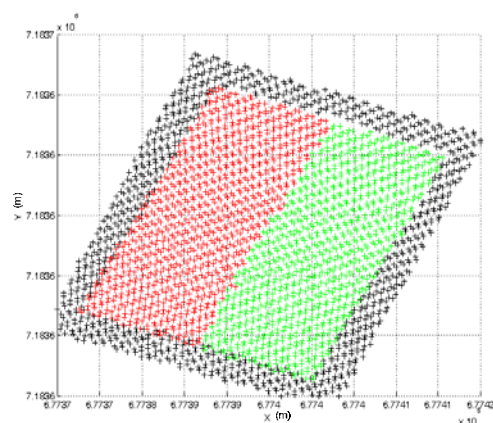
(a)



(b)



(c)



(d)

Figure 4.22: Aggregation of points with similar attributes: the digital image (a), the Digital Surface Models over the area of interest (b), the accumulator array (c), and the segmented patches (d).

Afterwards, the points, which contribute to the highest peak are identified. Using these points, plane fitting is conducted through least squares adjustment procedure. Then, the quality of plane fitting is evaluated by checking the average of the squares of the distances between the points and their corresponding projections onto the plane along its

normal direction. The acceptable quality of plane fitting is decided while considering the noise level of LiDAR data utilized. Poor plane fitting will occur when the ambiguity mentioned in the attribute computation procedure exists even though the possibility is relatively low. In other words, the points belonging to the planes with different slopes and aspects might contribute to the highest peak and cause the poor plane fitting result. In this case, the ambiguity will be resolved by introducing two new origins with different locations (compared to the original ones) for the points causing the problem. More specifically, a small accumulator array for only the points located at the peak will be constructed using their attributes recomputed from two new origins. This is expected to lead to the separation of the points belonging to the planes with different slopes and aspects in the accumulator array. Then, plane fitting using the points contributing to the highest peak will be conducted again. This process is repeated until a good quality of plane fitting is acquired. Afterwards, the clustering process moves to the other points which did not contribute to the highest peak but with similar attributes (i.e., bins neighbouring to the highest peak). This step is necessary to consider the inaccuracy of the computed attributes of certain points, which are generally either located around break lines or affected by noises. More specifically, an initial cluster will be first defined by including the points contributing to the highest peak. Then, the points registered at the neighbouring cells around the highest peak will be identified in the accumulator array. Among these points, only ones which are close (i.e., 3D proximity) to the points belonging to the initial cluster in the space domain will be considered as candidates. Normal distances between the candidate points and the plane defined by the points in the initial cluster will be computed. Then, the points which have normal distances less than

the pre-determined threshold (computed based on the noise level of LiDAR data utilized) will be accepted into the cluster. This process will be implemented until no more points can be included into the cluster. Once this cluster growing has been completed, the points in the cluster will be recorded and removed from the accumulator array. Now, the second highest peak can be detected and the same steps implemented for the first highest peak will be repeated. This process of moving from the highest peak to the next one is repeated until the number of points located at the last peak is less than the number of points that have been pre-determined to make up the minimum detectable patch size in the object space. Figure 4.22(d) shows the clustered points categorized into two different groups using the above technique.

One should note that this procedure provides a robust and accurate segmentation solution because the points are clustered while globally assessing the local attributes in the parameter space together with the proximity of the points in the object space at the same time. Moreover, it is more efficient compared to the segmentation process using more than two attributes in terms of computational load since the proposed process utilizes only two attributes.

So far, the points belonging to different planar patches are identified and grouped into different clusters. In other words, building primitives (i.e., planar patches constituting rooftops) are derived from building hypotheses as the outcome of the segmentation process.

4.4.2 Initial boundary generation for building primitives

One should note that the points belonging to the coplanar but disconnected planes can be grouped into the same cluster. This will only happen if the points contributed to the highest peak are from two different coplanar groups. The separation of these groups can be achieved by conducting a neighbourhood analysis through boundary detection of the clustered points. Also, the boundaries of the clusters will provide the information of building shape. First, the points in each cluster are used to determine a plane through a least squares adjustment procedure. Once all the points involved are projected onto the determined plane, a boundary detection algorithm is applied to the projected points. The modified convex hull approach (Jarvis, 1977) is adopted to determine the boundary for each of the segmented clusters. Figure 4.23 illustrates the principal steps of the modified convex hull approach for tracing the boundary of a point cluster. As shown in the first row, the process starts by selecting the leftmost point (empty circle) as a boundary point. All points within a neighbourhood (grey circles) are selected. For LiDAR data, this neighbourhood can be defined as two or three times the average point spacing of the data in consideration. The convex hull algorithm is then used to determine the next point on the boundary by only considering the points within this neighbourhood. After that, the algorithm proceeds to this newly determined boundary point and the same procedure is repeated until the boundary is fully determined. The last row shows the different results produced by using the conventional convex hull and the modified one. Figure 4.24(a) and Figure 4.24(b) show the points extracted from the previous steps in the proposed segmentation methodology and the detected boundary of these points, respectively.

This boundary detection procedure is extended to deal with points from different patches, which are coplanar but spatially separated. Figure 4.25(a) shows an example of such a scenario, before applying the boundary detection algorithm. As can be seen in the figure, there are two large sets of points and a few spurious points. Since the boundary detection process is designed to start from the left most points, the boundary for the set of points located at the bottom of the figure is detected first. Then, all the points located inside the boundary are identified and classified as one cluster. Once all these points have been recorded and removed from the entire dataset, the same procedure is conducted for the remaining points, in an iterative process; see Figure 4.25(b).

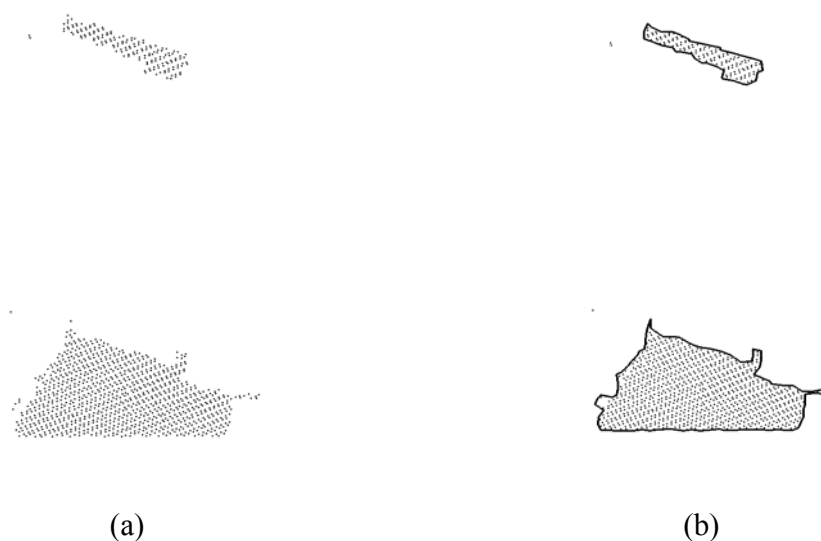


Figure 4.25: Neighbourhood analysis via boundary detection: multiple coplanar patches detected from the attribute space (a), and patches separated through boundary detection (b).

One should note that a building hypothesis generated in Section 4.3 might be composed of several planar patches. Two situations are involved in this case. The first situation occurs when the closeness of the points on the different planes is less than the proximity threshold for grouping. The other situation comes from a structure formed by a series of connected planes with different slopes and aspects. The proposed segmentation and boundary generation techniques identify the LiDAR points located on the same planar patch while considering the similarity of their attributes as well as their proximity. In other words, each building hypothesis is broken down into a group of building primitives (i.e., the individual planar patches constituting the building rooftop) with their initial boundaries. Figure 4.26(a) and Figure 4.26(b) illustrate the generated building primitives and their boundaries. The building hypotheses including the several planar surfaces (as shown in Figure 4.14) are separated into the several primitives.

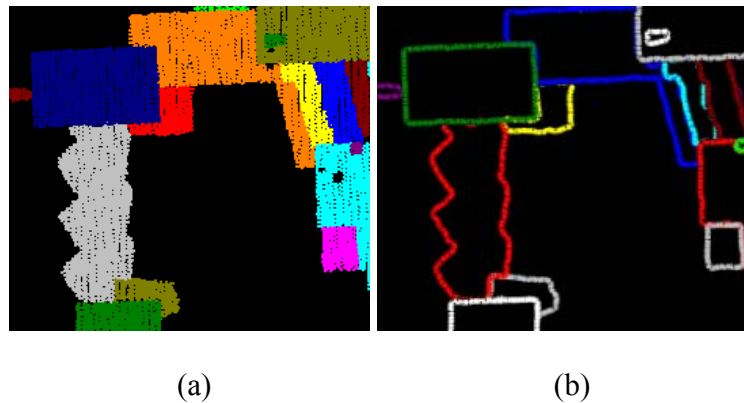


Figure 4.26: Building primitives (a), and boundaries of the building primitives (b).

One of the initial boundaries of the building primitives is projected onto the involved imagery, in Figure 4.27. As shown in the figure, the boundaries closely follow the trend of the building shape. However, deviations exist between the initial boundary of the building primitive and the precise building boundaries. As mentioned in Chapter 3, these deviations are mostly due to the irregular and sparse nature of LiDAR data. Chapter 5 will propose methodologies to improve the quality of the boundaries of the building primitives. Moreover, the chapter will address the refined 2D and 3D visualizations once the enhanced surface models are acquired.



Figure 4.27: Projected initial boundary onto the imagery for a given building primitive.

4.5 Summary

This chapter explained the procedures necessary for building hypothesis and primitive generation. The proposed angle-based approach for true orthophoto generation in Chapter 3 was extended and applied for terrain and off-terrain classification by introducing synthesized projection centers. The proposed methodology is quite successful in the classification of LiDAR point cloud including even high frequency components in the terrain surface (e.g., cliffs).

Afterwards, building hypotheses were generated using the classified off-terrain points. By checking planarity of the off-terrain points, they were further classified into points on planar and rough surfaces. The points belonging to planar surfaces were grouped according to their three-dimensional proximity. After this, building hypotheses were generated while considering the area and the height of the groups relative to neighbouring terrain points.

To acquire building primitives from the generated building hypotheses, segmentation and boundary generation were then conducted. The adopted neighbourhood definition, which considers both the three-dimensional relationship between irregularly distributed points and the physical shapes of surface, increased the homogeneity of the derived attributes. Then, the increased homogeneity improved the quality of point clustering. An efficient and robust clustering process was designed by utilizing only two attributes and by globally assessing the local attributes in the parameter space together with the proximity of the points in the object space at the same time. Finally, initial

boundaries of the building primitives were acquired using the modified convex hull approach.

Visual investigation of the projected initial boundaries onto the corresponding image verified that the boundaries closely follow the trend of the building shape. However, deviations between the derived initial boundaries of the building primitives and the precise building boundaries were recognized. These deviations were caused by the irregular and sparse nature of LiDAR data. There is need for the improvement of the initial boundaries of the building primitives to acquire a precise building model. Thus, methodologies to improve the quality of the building primitive boundaries will be proposed in Chapter 5 together with the refined 2D and 3D visualization.

Chapter 5 : Building Reconstruction and Visualizations

5.1 Introduction

In Chapter 4, the procedures necessary for building hypothesis and primitive generation were explained as steps in the enhancement of surface models. These procedures were carried out based on LiDAR data only. Through the investigation of the boundaries of the building primitives produced in that chapter, it was found that more accurate building boundaries are required in order to generate high quality building models, surface models, and surface descriptions. To fulfill the need for quality, this chapter will first address methodologies for generating enhanced building models. After this, the creation of enhanced surface models and surface descriptions will be discussed. Building model generation will be based on the integration of photogrammetric and LiDAR data. Stereo aerial images will be utilized for this integration.

For precise building model generation, four different types of boundary segments are acquired, depending on different situations. The scenarios for different situations and the methods for extracting these boundary segments are explained in detail in Section 5.2. Once the precise building models have been generated, the quality of the digital surface models will be improved by combining the building models and the terrain models (using the terrain points acquired previously, in Section 4.2 of Chapter 4). Finally, in Section 5.3, high quality 2D and 3D visualizations will be produced using the enhanced surface models and the corresponding imagery.

5.2 Building Reconstruction

Since precise building models are essential for the generation of high quality surface models and surface descriptions, this section focuses on methods for precise building model generation. Figure 5.1 shows a flow chart of the building reconstruction procedure proposed in this research.

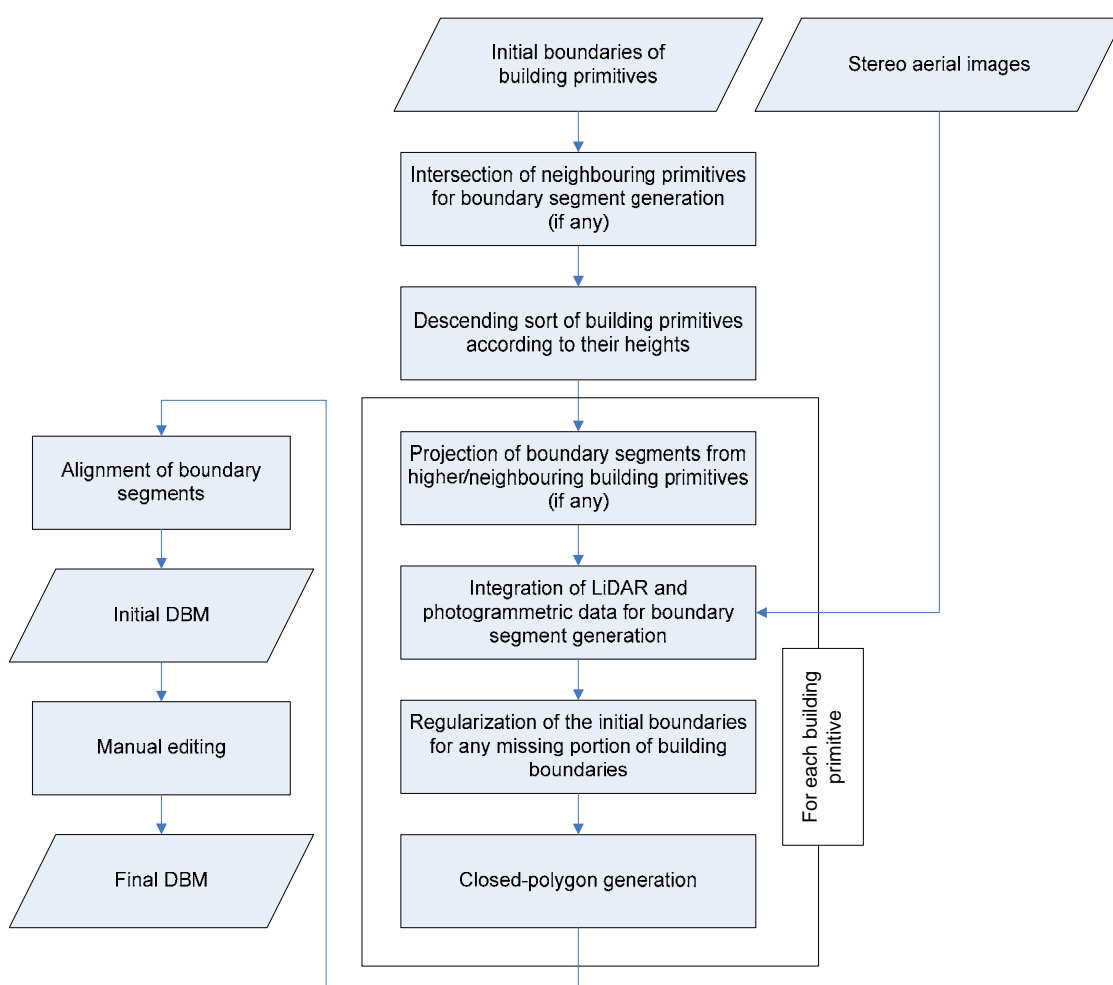


Figure 5.1: Flow chart of the building reconstruction procedure.

The proposed procedure starts with precise building boundary segment generation. The methods of boundary segment generation are designed to take into consideration four different building boundary segment scenarios. For each different scenario, the appropriate data type (i.e., either LiDAR data or both LiDAR and photogrammetric data) is selected, and an appropriate method is developed. A ridge line on a gable roof, as shown in the area enclosed by the red dashed ellipse in Figure 5.2 (a), is one of the examples of the first scenario. The initial boundaries of the building primitives corresponding to the roof patches are projected on the corresponding image. Since the plane parameters of the building primitives were derived with high accuracy in Chapter 4, a method of boundary segment generation for this case is developed by utilizing the plane parameters of two neighbouring building primitives. The precise boundary segments can be accurately derived through the intersection of neighbouring building primitives (1 and 2 in Figure 5.2 (a)). The second scenario includes all the boundary portions for which both LiDAR and photogrammetric data can be utilized. The two datasets are integrated, and their synergistic properties are utilized in the boundary segment generation method in this case. The third scenario exists when there are building primitives which share a vertical wall but have different elevations. In this case, a higher building primitive usually hide a lower one. Figure 5.2 (b) and Figure 5.2 (c) show an example of this case. As shown in the figures, a higher building primitive (1) is partially hiding another lower one (2) (in the area enclosed by the red dashed ellipse). The initial boundary of the building primitive (2) is projected on the corresponding stereo images (red solid lines in Figure 5.2(b) and Figure 5.2(c)). The boundary in the area enclosed by the red dashed ellipse seems to be far from the actual building boundary in the left image. Such a

deviation is the result of relief displacement from the higher building primitive (1). One should note that boundary of the building primitive (1) can be determined through the method using the integration of two datasets while a portion of the building primitive (2) cannot. For this case, the boundary segments constructed for the higher building primitives are utilized to generate boundary segments for lower one while considering the proximity of the building primitives involved. The fourth scenario involves the building boundary portions (for which precise boundary segments have not been detected) that remain after all three methods mentioned above have been considered. Figure 5.3 shows an example of this case. The portions of building primitive (2), which are enclosed by the red dashed ellipses, do not appear in either of left and right images or in both of them. In other words, the upper region A of building primitive (2) is totally hidden by building primitive (1) in the left and right images. And, the lower region B of building primitive (2) appears only in the left image. The initial boundaries of the building primitives are utilized in this case after regularization.

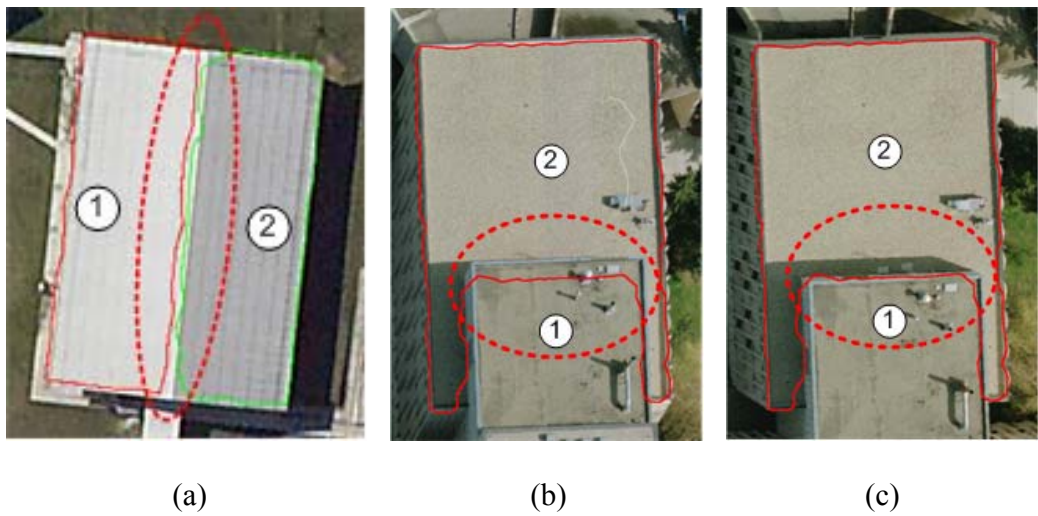


Figure 5.2: A ridge line on a gable roof (a) and a building primitive hidden by another higher on in left (b) and right (c) images, in the areas enclosed by the red dashed ellipses.

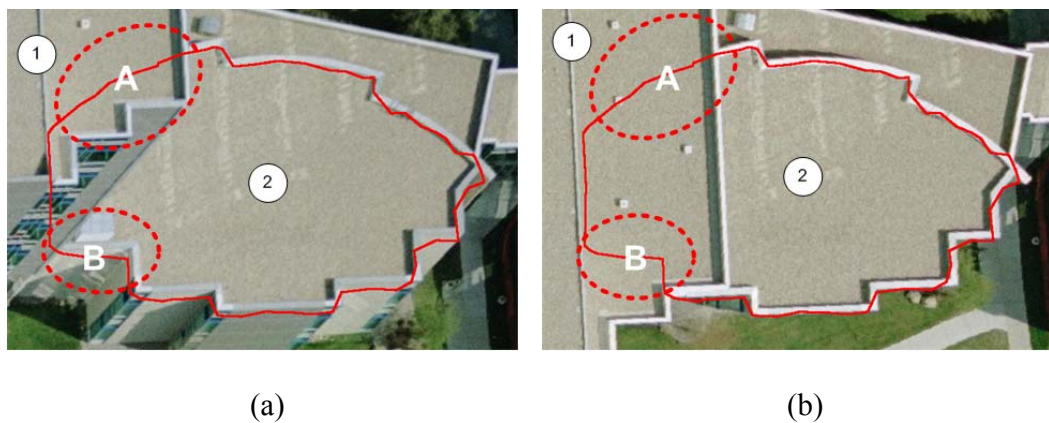
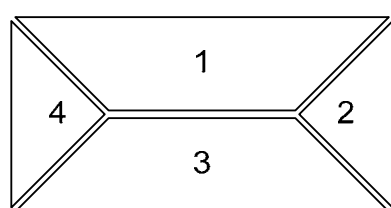


Figure 5.3: Portions of a building primitive, which are hidden by a higher one either in left (a) and right (b) images or in both of the images, in the areas enclosed by the red dashed ellipses.

After producing all boundary segments for each building primitive, while considering all the different boundary scenarios, the segments are converted into closed-polygons. Finally, building models are constructed using all the boundary segments of the closed-polygons. For the missing and erroneous boundaries, manual editing is introduced as a post-processing step. More detailed explanations of the building model generation procedures are provided in the subsections that follow.

5.2.1 Precise boundary segment generation through the intersection of neighbouring planar patches

Since the building primitives produced earlier have accurate plane parameters, precise boundary segments for ridge lines (see Figure 5.2(a)) can be generated by intersecting the two building primitives adjacent to the ridge line. Prior to the implementation of the intersection procedure, neighbourhood analysis of the building primitives should be conducted. The neighbourhood analysis starts by defining a 3D adjacency table that identifies neighbouring building primitives. In the adjacency table, two building primitives will be deemed as neighbours if part of the initial boundary of one primitive is located within a buffer zone surrounding the boundaries of the other primitive. Figure 5.4 shows an example of 3D neighbourhood analysis for building primitives and a defined adjacency table. The locations of the building primitives and the relevant adjacency table for these primitives are shown in Figure 5.4 (a) and Figure 5.4 (b), respectively.



(a)

	1	2	3	4
1		x	x	x
2	x		x	
3	x	x		x
4	x		x	

(b)

Figure 5.4: Locations of building primitives (a) and the relevant 3D adjacency table

(b).

The neighbouring building primitives are selected using the constructed 3D adjacency table. The intersection of the building primitives that are almost parallel and/or coplanar is avoided by checking the angle between surface normal vectors of the primitives since this would lead to a weak intersection. In other words, a set of two primitives for which this angle is greater than a pre-defined threshold is selected and intersected to acquire reliable results. Since the outcome of the intersection is an infinite line, the segmented points in the neighbouring primitives are used to define the endpoints of a finite segment. More specifically, all the segmented points of the two building primitives are first projected onto the intersection line. After this, the normal distance between each point and its corresponding projected point is computed. Only the points whose normal distances are less than a pre-defined threshold (which is determined as a function of the average point spacing of LiDAR data) are considered in the next step (see Figure 5.5). The extreme end points on the intersection line can be used to define a finite line segment.

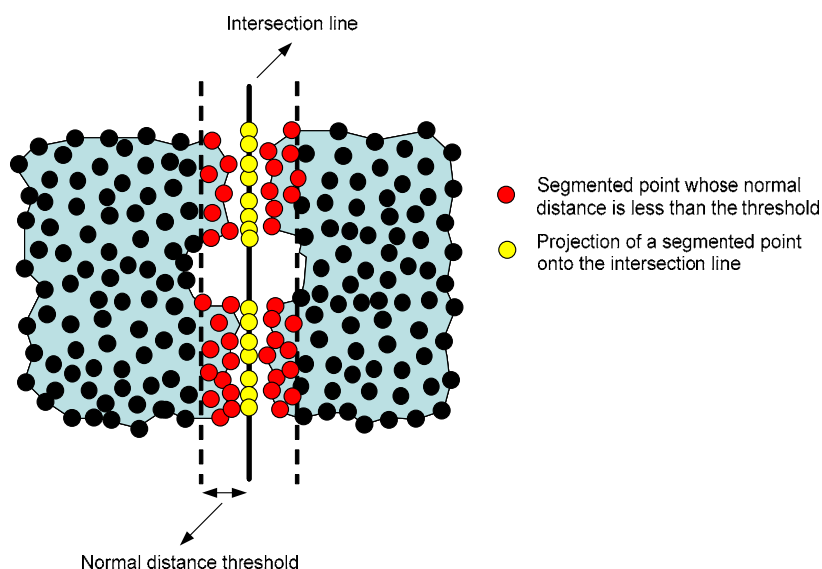


Figure 5.5: Segmented points in the neighbouring primitives and their projections onto the intersection line (top view).

The gap between adjacent projected points on the intersection line (yellow dots in Figure 5.5) is analyzed to determine whether the intersection line should be broken down into several boundary segments. Where there exists a gap that is greater than a given threshold (which is determined as a function of the average point spacing of LiDAR data and knowledge of building structure), it is concluded that this intersection line portion consists of more than a single line segment (see Figure 5.6). The extent of each boundary segment is defined by identifying the extreme end points on the intersection line. Once a boundary segment has been determined, all the boundary points that are closely located to the segment are identified and removed from the boundary in question. One should note that these points will not be considered in the other boundary segment generation methods. In other words, only the remaining boundary points will be utilized in later

sections. Figure 5.7 shows a real example of a boundary segment extracted through the intersection of neighbouring building primitives. The derived boundary segment (Figure 5.7(a)) is projected onto the corresponding imagery (Figure 5.7(b)). As shown in the figure, the boundary segment is extracted precisely.

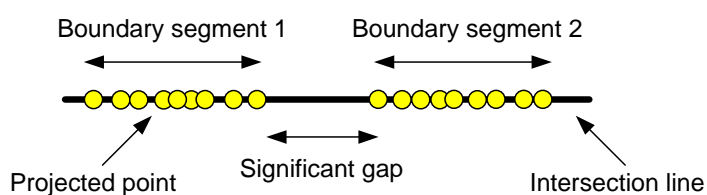
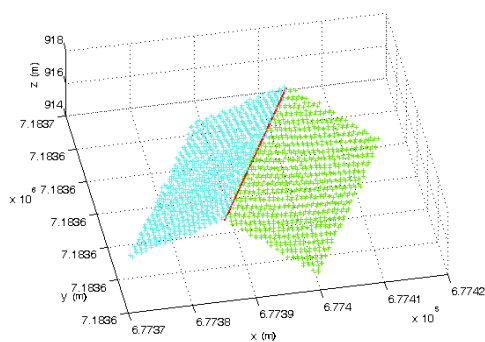


Figure 5.6: Boundary segment generation through the detection of significant gaps between adjacent projected points.



(a)



(b)

Figure 5.7: Boundary segment generated through the intersection of two neighbouring primitives (a) and the segment projected onto the corresponding image (b).

5.2.2 Precise boundary segment derivation through the integration of LiDAR and photogrammetric data

Once the boundary segments have been generated through the intersection of neighbouring building primitives, precise boundary segments for the remaining portions of the building boundaries will be derived through another method for boundary segment generation. Before explaining the procedures for this method, one should note that the initial boundaries of the building primitives produced in Chapter 4 provide overall trend but not accurate details of the building shape. Conversely, imagery contains richer building boundary information, such as edge lines and colour attributes, which provide more details on the shape of the buildings. To provide accurate building boundary segment generation results, a method based on the integration of LiDAR data and stereo imagery is proposed at this stage. One should note that the matching procedure is a key part of image-based approaches for building reconstruction. However, feature matching in large scale imagery over urban areas still remains to be an ill-posed problem. These problems come mainly from differences in scale, geometric distortions, illumination conditions, and relief displacements. Some researchers have tried to introduce epipolar geometry and cross-correlation methods to improve the performance of the matching procedure, using only linear features derived from imagery (Baillard and Zisserman, 1999). However, these kinds of attempts would fail when one is dealing with straight line segments, which are parallel to the epipolar lines and when there are geometric and spectral differences between conjugate features in the left and right images due to relief displacement. Moreover, such matching measures do not consider the derived information from the LiDAR segmentation (e.g., the parameters defining the planes of

the building primitive in question). Hence, it was decided to incorporate LiDAR data in the image matching procedure as a constraint in this research. This solution will later provide more precise building reconstruction results compared to those derived from either photogrammetric or LiDAR data alone. Figure 5.8 shows a flow chart of the precise boundary segment generation method based on the integration of LiDAR and photogrammetric data. This method is carried out through several steps: 1) Warped image generation; 2) Straight line detection; 3) 3D line matching; 4) Grouping of matched 3D lines; and 5) Precise boundary segment selection. These steps will be explained in the following paragraphs. Briefly, warped images will be generated to relate imagery and LiDAR data in one step. The geometric difference along the building primitive will be eliminated by utilizing the warped images in the matching procedure. Since the target of this research is buildings with planar rooftops, which are bounded by straight lines, the detection of straight lines will be conducted using warped images. Matching process will be carried out on the LiDAR plane of the building primitive in question while utilizing the derived straight lines. In other words, incorporating LiDAR data in the image matching process will provide geometric constraints to improve the matching quality. Precise matched 3D lines will be acquired from this process. Afterwards, matched 3D lines will be divided into groups of non-overlapping line segments, which are believed to be competing for the same boundary segment of the building primitive in question. Finally, a spectral constraint will be utilized to select the precise building boundary segment among the members of each group.

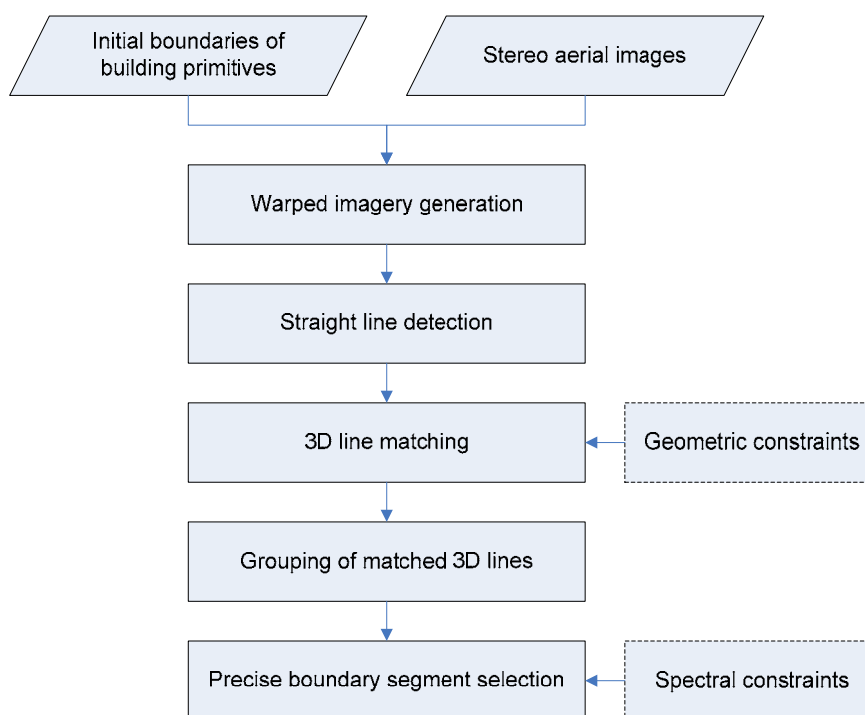


Figure 5.8: Flow chart of the precise boundary segment generation method based on the integration of LiDAR and photogrammetric data.

Warped imagery generation

One should note that the use of *warped imagery*, which is a new concept in the integration of LiDAR data and imagery, is introduced instead of using the original imagery directly. This integration will eliminate geometric differences along the building primitive in the warped images; hence, direct comparison of spectral information between these images will be possible without considering geometric distortions which exist in the original imagery. More specifically, warped images are generated through the simple projection of the original images onto the plane of the relevant building primitive generated from the LiDAR data. The inverse concept of photography is applied to the

generation of warped imagery. First, the range of a building primitive is extended beyond the derived initial boundary while considering the resolution of the LiDAR data. Using the collinearity equations, each object point on the building primitive plane in question is projected onto the corresponding image plane. Then, the grey value at the projected image location is assigned to the corresponding location of the object point on the building primitive plane. Figure 5.9 illustrates the concept of warped imagery. As can be seen in the figure, the degree of similarity between the left and right warped images for a location on the rooftop of a building primitive will be high since the corresponding points in the left and right images are conjugate; refer to points D, E and F and their grey values on the warped images ($g(d_l)$ & $g(d_r)$, $g(e_l)$ & $g(e_r)$, and $g(f_l)$ & $g(f_r)$). The degree of similarity for a point that does not physically belong to the building rooftop (e.g., point B in Figure 5.9), on the other hand, will be lower since the projected points onto the left and right images correspond to non-conjugate points. For example, the image points (b_l) and (b_r) in Figure 5.9 correspond to the object points C and A, respectively. Hence, the grey values at the same location of point B on the left and right warped images will come from different objects on the wall and ground, respectively. In summary, the left and right warped images only agree with one another along the rooftop patch.

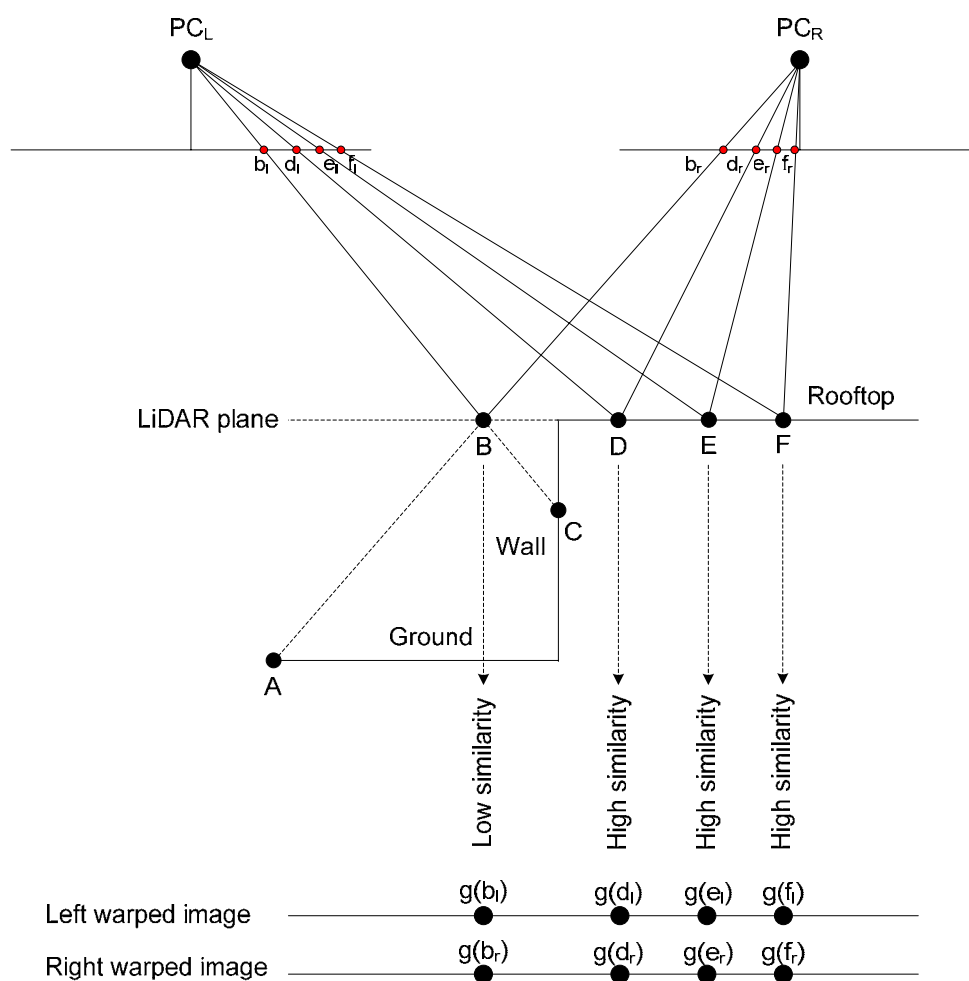


Figure 5.9: Concept of warped imagery.

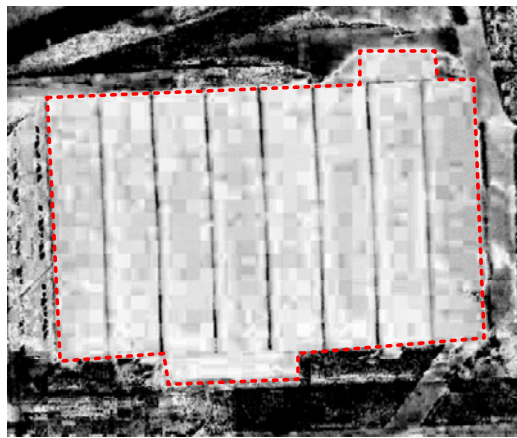
Figure 5.10 (a) and Figure 5.10 (b) show the left and right warped images produced using a real dataset. Also, a similarity map (Figure 5.10 (c)) is derived by comparing grey values at the same location on the left and right warped images. High similarity is represented by brighter grey values and the other way around for low similarity. As can be seen in the similarity map, the region along the rooftop patch (enclosed by red dashed line) has brighter grey values than other regions. In other words,

the region along the rooftop patch has high similarity; however, the other regions outside the rooftop patch have low similarity.



(a)

(b)



(c)

Figure 5.10: Produced left (a) and right (b) warped images and a similarity map (c) derived from these images.

Straight line detection

Once the concept of warped imagery has been introduced, linear features which are extracted directly from the warped images are utilized in this boundary segment generation method. Before implementing the linear feature extraction procedure, visibility analysis is conducted through the use of visibility maps, which were produced together with the true orthophotos in Chapter 3. The reason for the visibility analysis is to ignore the edges if they do not originate from the primitive under consideration. Figure 5.11(a) and Figure 5.11(b) show a visibility map along one profile, and the top view of the map, respectively. The edge pixels in occluded/invisible areas will be ignored since they do not belong to the building primitive in question. Once the visibility analysis has been conducted, linear feature extraction is carried out using the edge detection technique.

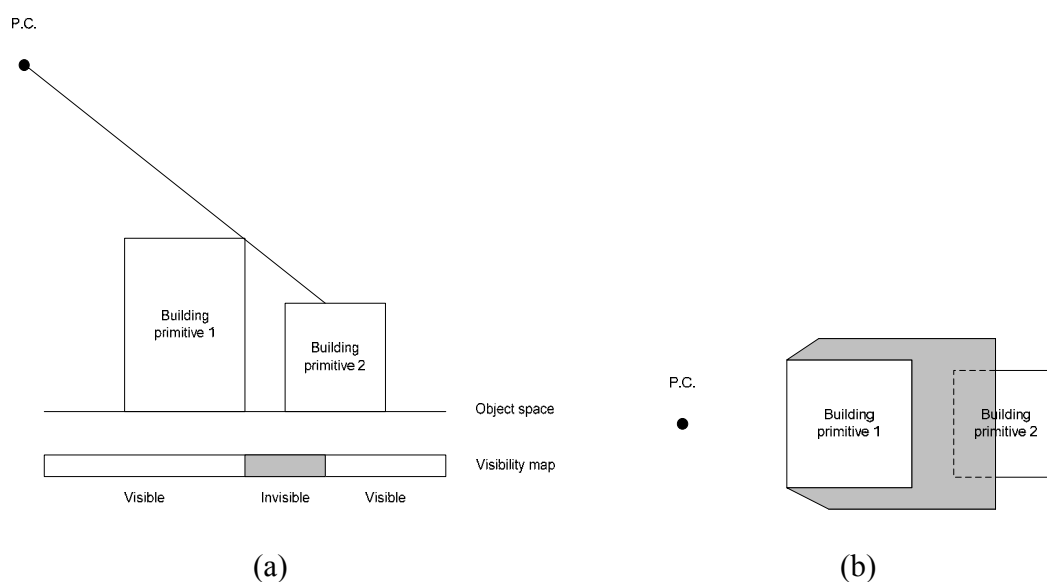


Figure 5.11: Visibility map along one profile (a), and top view of the visibility map (b).

Discrete edge points are first detected by applying the Canny edge detector (Canny, 1986) to the warped images. A buffer is defined around the initial boundary of each building primitive in the two warped images. Then, only the edge points that are inside the defined buffer zone (which is determined as a function of the average point spacing of LiDAR data) are utilized to extract straight lines. Following the edge detection, edge linking is conducted by tracking neighbouring edge points. Afterwards, key points in the chain generated by edge linking are detected using Douglas-Peucker algorithm (Douglas and Peucker, 1973). The key points usually correspond to the vertices of the chain. Then, the original chain is split into several small chains using the detected key points. After the division process has been completed, the chains of edge points are converted into straight lines through line fitting using a least squares adjustment procedure. The proximity and parallelism (or collinearity) of the straight lines are investigated to determine whether they belong to the same edge line. For this investigation, the line merging method introduced by Zuxun et al. (2004) is adopted. The linear features which are believed to belong to the same object line are merged in order to construct a single straight line through a line fitting process. Figure 5.12(a) and Figure 5.12(b) show the straight line segments detected in the left and right warped images, respectively.

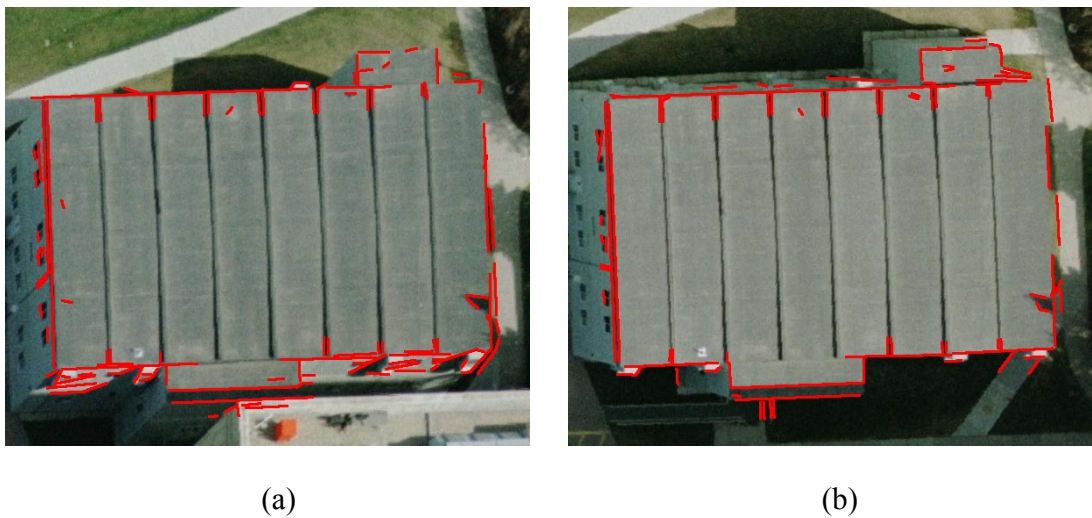


Figure 5.12: Straight line segments detected in the left (a) and right (b) warped images.

3D line matching

The next step involves the matching of straight line segments detected in the left and right warped images. As mentioned above, feature matching is usually conducted in the image space. However, it fails in situations in which the linear features are parallel to the base line, as well as when there are geometric and spectral differences between conjugate features in the left and right images due to relief displacement. Moreover, the matching measures employed do not consider the information derived from the LiDAR segmentation procedure (e.g., the parameters defining the plane of the building primitive in question). The line segments extracted from the left and right warped images are matched through the use of three geometric constraints: angular deviation, normal distance, and presence of overlap. Two line segments (e.g., line segments, AB and CD from the left and right warped images, respectively) are considered to be matching candidates if the angle and the normal distance between these segments are smaller than

given thresholds; see Figure 5.13(a). If the angle and normal distance values are within the pre-specified thresholds, the presence of overlap between the two segments after their projection onto the line bisecting the space between them is checked ($B''C''$ in Figure 5.13(b)). The pairs of line segments that satisfy the three geometric constraints are collected from among all the possible pairs of line segments. At this stage, one-to-many matching of the line segments in the left and right warped images is allowed. Afterwards, these pairs of line segments are ordered according to their normal distances (i.e., the first constraint). Among the line pairs, the one with the shortest normal distance between line segments is selected (let's call the line segments in this line pair $L1$ and $L2$). Then, any other line pairs that contain either $L1$ or $L2$ are discarded from the list of line pairs. In the same manner, this process continues for the line pair with next shortest normal distance among the remaining line pairs in the list. Now, one-to-one matching between the line segments in the left and right warped images has been completed. One-to-one matching based on the ordering of the normal distances between line segments provides accurate matching results without producing a large number of similar results. After this process, each line pair remaining in the ordered set will define a matched 3D line by determining the extreme points among the projected endpoints along the line bisecting the space between the two segments in question (the resulting line is $A''D''$ in Figure 5.13(b)).

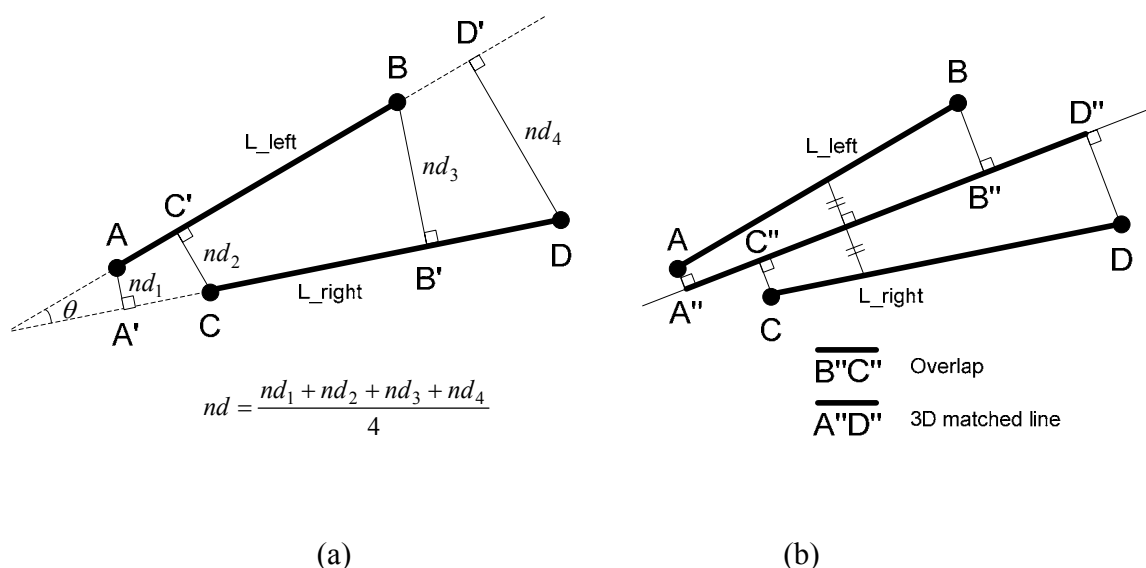


Figure 5.13: Matching straight line segments in warped images using angle and normal distance constraints (a) and the presence of overlap between straight line segments, and 3D matched lines (b).

Figure 5.14 shows the matched 3D lines for the straight line segments in Figure 5.12(a) and Figure 5.12(b). One should note that the technique of matching the line segments onto the warped imagery plane takes advantage of both the higher planimetric accuracy of the image-based reconstruction and the higher vertical accuracy of the LiDAR data. As seen in the figure, some of the matched 3D lines have significantly different orientations than the real boundary. Assuming that the segmentation result is reliable, the initial boundary of the building primitive provides a good overall building shape trend. Hence, the matched 3D lines are compared to the initial boundary of the building primitive to remove matched 3D lines that do not correspond to the boundaries of the building primitives.



Figure 5.14: Matched 3D lines for the straight line segments in Figure 5.12(a) and (b).

The concept of the comparison of the matched 3D line under investigation to the corresponding initial boundary is illustrated in Figure 5.15. First, lines that are orthogonal to the matched 3D line, with pre-defined lengths, are spaced at regular intervals along the matched line (these are the dashed lines in the figure). The intersections of these dashed lines with the initial boundary are conducted. The closest intersection points (green circles in the figure) to the matched line are identified in this process. Afterwards, the ratio of the number of the intersection points (i.e., green circles) to the number of orthogonal lines (i.e., dashed lines) is calculated. For a matched 3D line that follows the trend of the building shape as defined by the initial boundary, this ratio will be close to one (Figure 5.15(a)). Conversely, the ratio for a line that does not follow the trend will be

much less than one (Figure 5.15(b)). Only matched 3D lines whose ratios are greater than a pre-defined value are kept and utilized in the following procedures. Figure 5.16 shows the matched 3D lines after filtering out the lines that do not follow the trend of the building shape as represented by the initial LiDAR boundary.

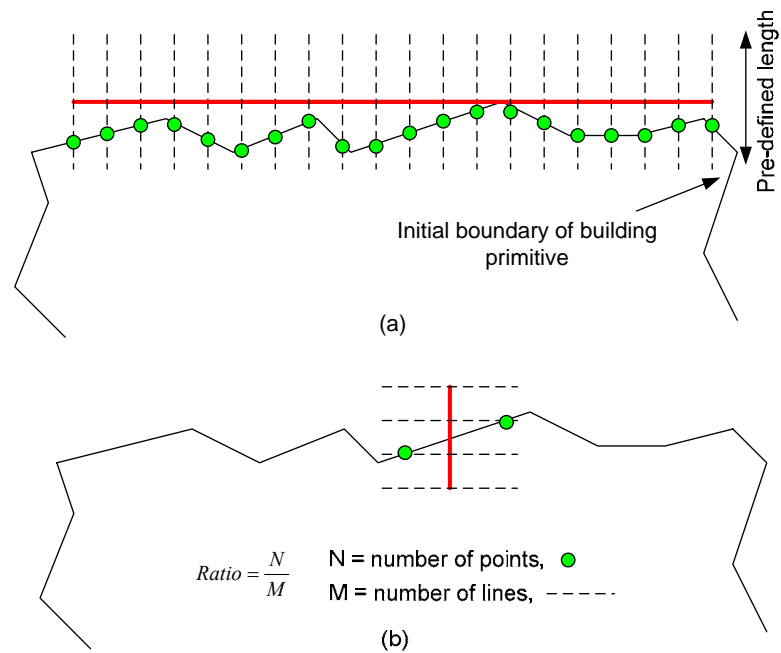


Figure 5.15: A matched 3D line that follows the trend of the initial boundary of the building primitive (a), and one that does not (b).



Figure 5.16: Filtered matched 3D lines which are obtained after the filtering process is applied to the matched 3D lines in Figure 5.14.

Grouping of matched 3D lines

The objective of this step is to divide the filtered matched 3D lines into groups of non-overlapping line segments, which are believed to be competing for the same boundary segment of the building primitive in question. The division is based on a reference line established for each of these groups. A matched 3D line will be selected as a reference line if it is the longest line segment among neighbouring/overlapping line segments and is located within the buffer surrounding the initial LiDAR boundaries of the building primitive in question. Based on those criteria, line segments 1, 2, 3, 5 and 7 will be selected as reference lines when considering the initial boundary and matched 3D lines in Figure 5.17 (a). Once the reference lines are established, the matched line segments will be grouped together based on their angular deviation, proximity, and

overlap with the reference lines (i.e., using the same 3D line matching constraints in Figure 5.13). Finally, all the matched line segments in the same group are extended to the extreme points in that group (refer to Figure 5.17 (b) where the identified five groups after the extension of their members are shown).

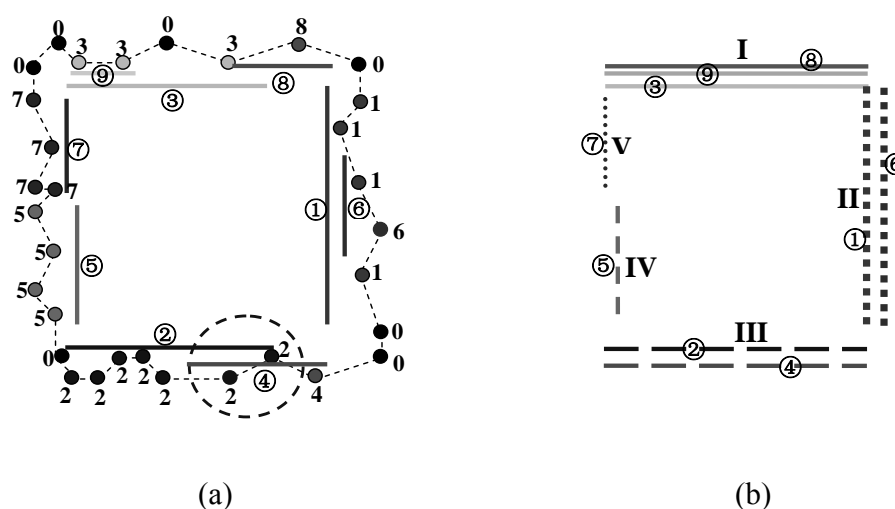


Figure 5.17: Establishing reference lines (a) and defining group members (b).

Even though one-to-one matching was conducted in the previous step, some of the extended members in a given group may be very close one another. Therefore, the close line segments in each group are merged according to the normal distances between these segments. The normal distance threshold for merging is defined by the Ground Sampling Distance (GSD) of the imaging sensor, as well as the noise level in the edge detection results and the established geo-referencing parameters (in this research, a normal distance threshold equivalent to three times the GSD has been used). Figure

5.18(a) and Figure 5.18(b) show the reference lines and the respective groups, established using the filtered matched 3D lines in Figure 5.16.

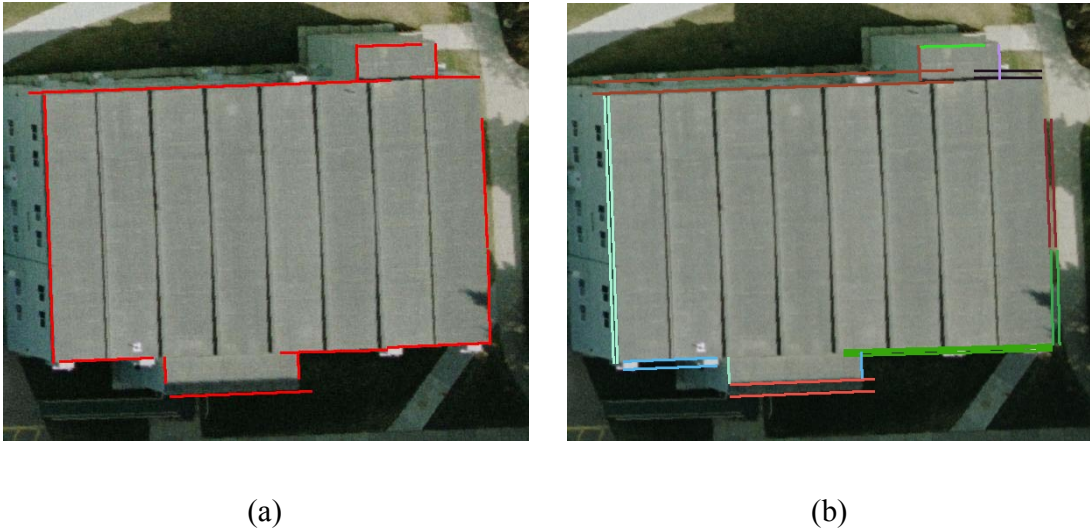


Figure 5.18: Established reference lines (a) and grouped matched 3D lines (b).

Precise boundary segment selection

The aim of this step is to select one line segment, which is believed to represent a precise boundary segment for the building primitive in question, from each of the established groups. For example, Figure 5.19 illustrates the case in which the line segments L1, L2, and L3 are matched 3D line segments in the same group on the left and right warped images.

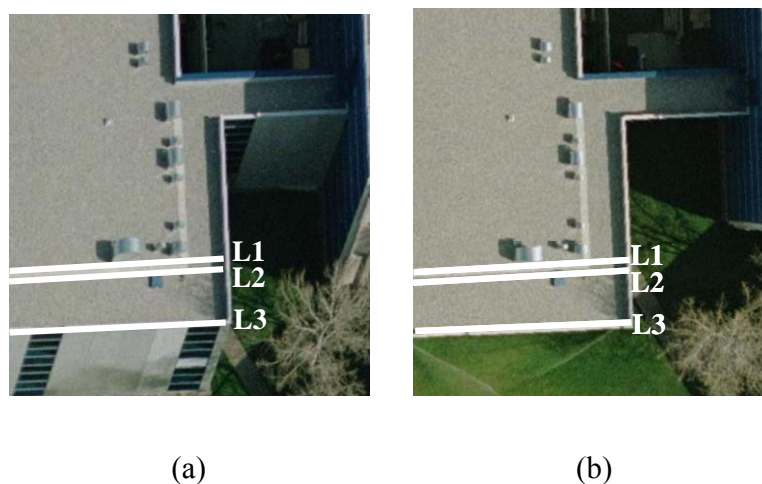


Figure 5.19: The members of an established group on the left (a) and right (b) warped images.

A spectral constraint is defined to select the precise building boundary segment among the members of each group. For this constraint, the similarity of the colour values on either side of each of the group members in the left and right warped images is investigated. The similarity measure at a given location along the building primitive plane (or warped image plane) is defined as the cosine of the angle between the Red Green Blue (RGB) colour vectors (Dony and Wesolkowski, 1999) at the same location in the left and right warped images. For example, the similarity measure at point (F) along the LiDAR plane in Figure 5.20 is defined by the cosine of the angle between the RGB colour vectors at (f_l) and (f_r) in the left and right images, respectively.

For precise boundary segment determination, two average similarity measures are defined for each group member, one for each of the regions on either side of the boundary segment. The precise boundary segment will be defined as the line segment for which the steepest transition from high to low degrees of similarity exists. As can be seen

in Figure 5.19 and Figure 5.20, the matched line segments L1 and L2 will not be selected as precise boundary segments since the degrees of similarity on both sides of these lines are high. Instead, the line segment L3 will be selected as the precise building boundary segment since it has the largest difference between degrees of similarity on either side; there is high similarity on one side (i.e., within the region along the building rooftop – see point D in Figure 5.20) and low similarity on the other side (i.e., where the similarity measure is defined by the RGB colour vectors along the building wall and along the ground in the left and right warped images, respectively – see point B in Figure 5.20). More detailed explanations of the computation of the average similarity measure and precise boundary segment selection using these measures are provided in the following paragraphs.

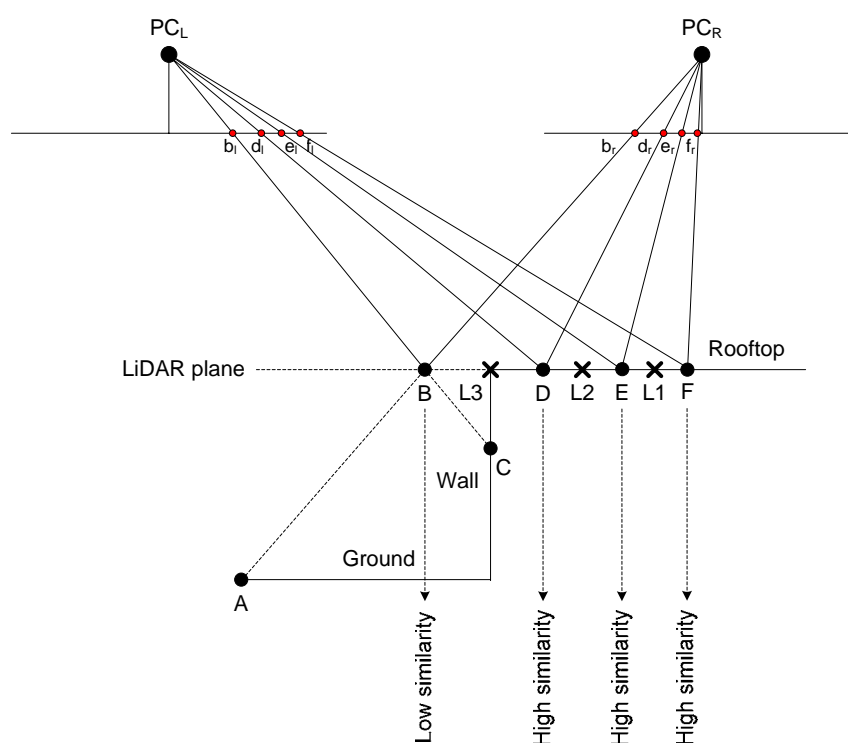


Figure 5.20: Similarity measures for different locations along the LiDAR plane.

Regions around the line segments in a particular group are defined based on the line segments (refer to Figure 5.21(a)). For example, the region r_2 is defined by L1 and L2. Also r_3 is defined by L2 and L3. Additionally, two more regions, r_1 and r_4 are defined by outermost lines and pre-determined buffers. Afterwards, each line segment divides the region defined for the group (i.e., $r_1 + r_2 + r_3 + r_4$) into two parts. For example, L1 defines two regions, R_{1_In} ($= r_1$) and R_{1_Out} ($= r_2 + r_3 + r_4$), around the line, as shown in Figure 5.21(b). For each line segment, two average spectral similarity values are computed, one for each of the regions, R_{i_In} and R_{i_Out} (for i^{th} line segment), using Equation 5.1. Afterward, the differences between the average spectral similarity values for the regions on either side of each line segment are calculated. After comparing the difference values for the line segments in each group, the line segment with the greatest difference value will be selected as the precise building boundary segment for the group (Equation 5.2). Figure 5.22 shows the precise boundary segments established for the groups in Figure 5.18(b).

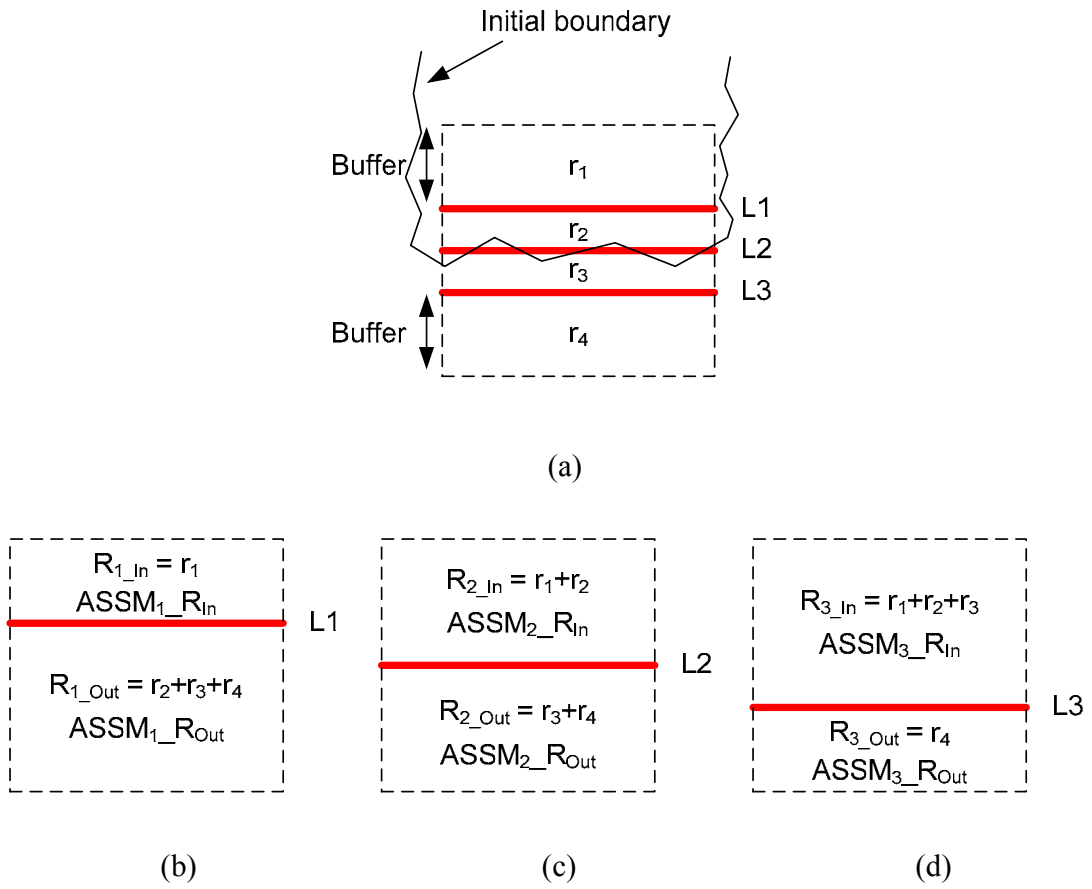


Figure 5.21: Configuration of the regions around the matched 3D line segments in one group (a), regions on either side of the line segments L1 (b), L2 (c), and L3 (d).

$$ASSM_{i_R} = \frac{\sum_{t=1}^m SSM_t}{m} \quad (5.1)$$

$$\arg \max_{\forall i} |ASSM_{i_R_{In}} - ASSM_{i_R_{Out}}|, i = 1, \dots, n \quad (5.2)$$

Where:

$ASSM_{i_R}$ is the average spectral similarity measure for a region on either side of line segment i ;

SSM_i is the spectral similarity measure for a certain point; and

m is the total number of points in a certain region.

n is the total number of line segments in the same group.

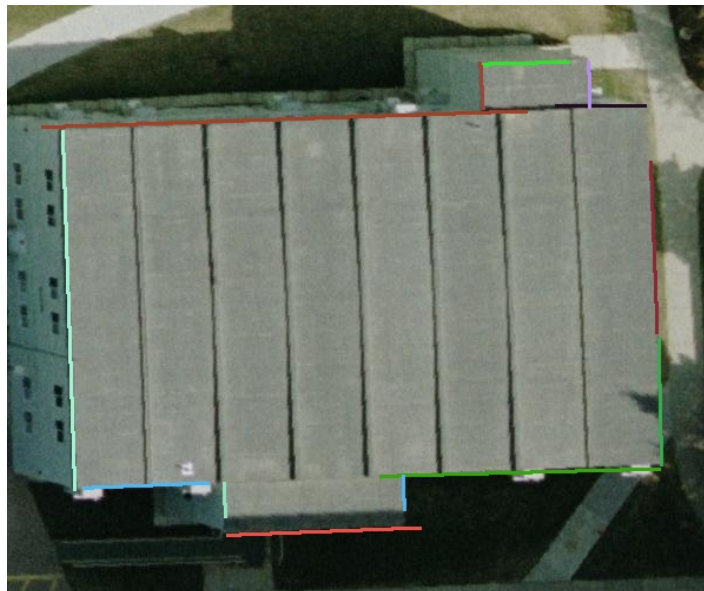


Figure 5.22: Established precise boundary segments for the groups in Figure 5.18(b).

So far, the boundary segments for the second scenario are derived through the integration of photogrammetric and LiDAR data. The synergistic properties from the integration of both datasets are utilized in the method to acquire precise boundary segments.

5.2.3 Precise boundary segment derivation through projection and regularization

One should note that this research focuses on the urban environments with complex and connected buildings. Hence, there might be significant occlusions in the large scale imagery. In this situation, a higher building primitive usually hides a lower one either partially or fully (refer to Figure 5.2 (b) and (c) and Figure 5.3). The first solution will be proposed for the areas including building primitives that share a vertical wall but have different elevations. Afterwards, the second solution will be suggested for the building boundary portions that remain after all other boundary segment refinement procedures have been considered.

Boundary refinement based on hierarchical projection

The solution for the building primitives that share a vertical wall but have different elevation can be derived from the projection of the constructed precise segments of higher building primitives onto lower, neighbouring building primitives, if any exists. This will be a solution for the third scenario mentioned above.

To do that, a 2D adjacency table that identifies neighbouring building primitives should be defined after the projection of their initial boundaries onto a horizontal plane. In the adjacency table, two building primitives will be deemed as neighbours if part of the initial boundary of one primitive is located within a buffer zone surrounding the boundaries of the other primitive. The 2D adjacency table will be utilized to find neighbouring building primitives for the primitive currently under consideration. Figure 5.23 illustrates the concept of this method. The red line indicates the boundary segment projected from the higher/neighbouring building primitive onto the building primitive

currently under consideration. Then, the boundary points of the current primitive, which correspond to the boundary segment (i.e., red line), are projected onto the segment. The extreme end points among the projected points define the range of the precise boundary segment for current primitive, similarly to the procedure explained in Section 5.2.1 (also refer to Figure 5.5 and Figure 5.6). Figure 5.24 shows a real example for the boundary segment generation based on the projection. The constructed boundary segments of the higher and neighbouring building primitive are shown as white lines in Figure 5.24(a). These lines are projected onto the current primitive and its boundary segments defined through the process mentioned above. Red line in Figure 5.24(b) indicates the initial boundary of the current primitive. White lines in the figure indicate boundary segments for the current primitive which are obtained after the projection process.

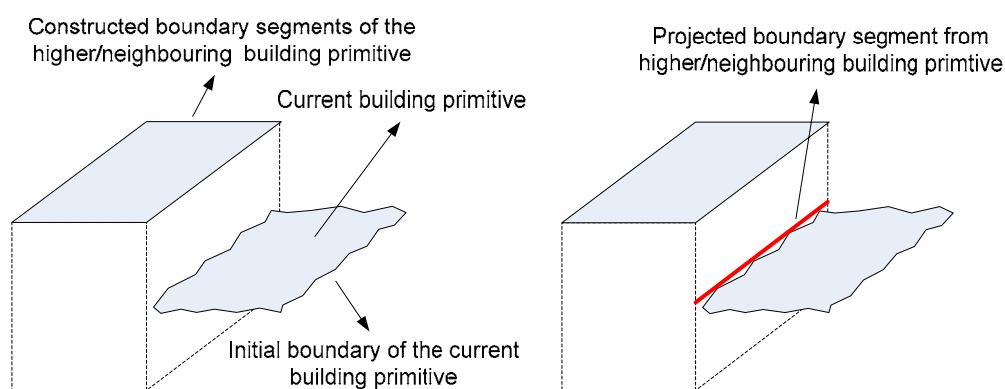


Figure 5.23: Projection of the constructed boundary segments of the higher/neighbouring building primitive onto the lower primitive under investigation.

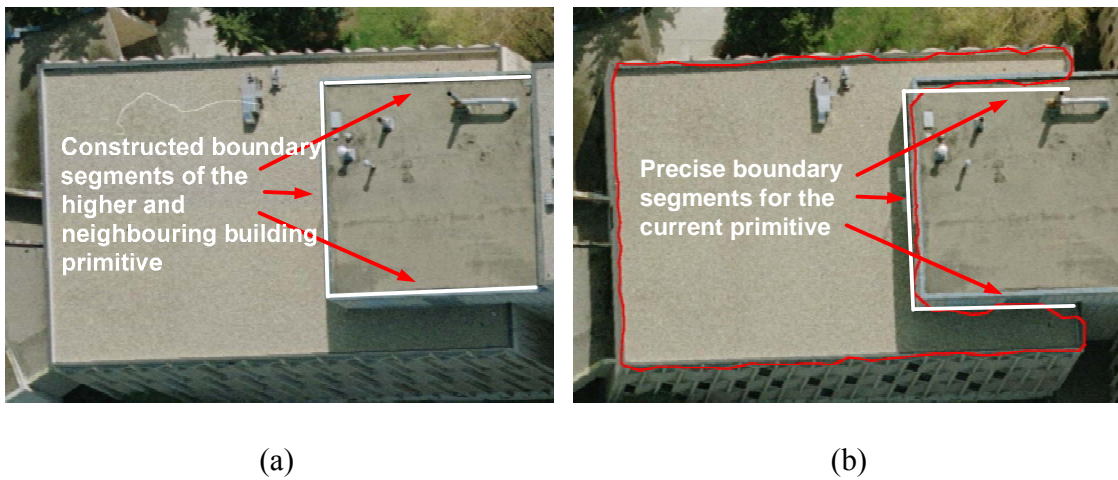


Figure 5.24: Constructed boundary segments of the higher and neighbouring building primitive (a) and precise boundary segments for the current primitive after projection process (b).

Boundary refinement based on regularization

Finally, the fourth scenario will be discussed for the case in which a higher building primitive partially or fully hides a lower, non-adjacent building primitive in the imagery (refer to Figure 5.3). Also, other cases with shadow effect, low image contrast, and non-straight boundaries can be included in this scenario. In these cases, the three different boundary segment generation methods mentioned above do not work properly. Since it is difficult to acquire useful spectral information, only the positional information from the LiDAR data will be utilized in this case. In other words, the building-primitive boundary will be reconstructed by regularizing the initial boundaries of the building primitives using the Douglas-Peucker and line fitting algorithms. Using the Douglas-Peucker algorithm, the key points, which correspond to the corner points of the boundaries,

are detected from the boundary points. All the boundary points located between a pair of key points are utilized for line fitting through a least squares adjustment. Then, the boundary points are projected onto the corresponding line derived from line fitting process. The extent of each line segment is defined by the extreme end points on the line in question. Figure 5.25 shows a real example for the constructed boundary segments after regularization process. In the figure, blue lines indicate the constructed boundary segments.

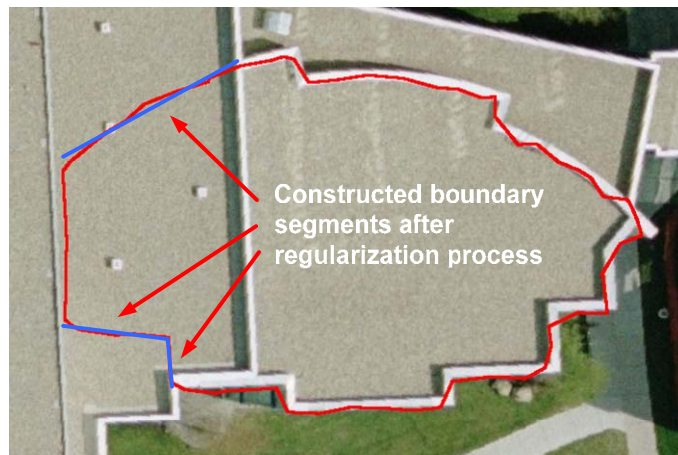


Figure 5.25: Constructed boundary segments after regularization process.

5.2.4 Closed-polygon and 3D building model generation

This procedure begins by establishing the proper sequence of the established boundary segments for each building primitive, by investigating their proximity to the ordered chain of vertices along the initial LiDAR boundary for that primitive. Figure 5.26 shows an example of establishing the proper sequence of the boundary segments. While following the ordered chain of the boundary vertices, the sequence of the line segments will be determined as $1 \rightarrow 4 \rightarrow 2 \rightarrow 3 \rightarrow 1$. To construct a closed-polygon for a given

building primitive, an intersection procedure is implemented to connect neighbouring boundary segments according to their established sequence. Figure 5.27 shows the closed-polygon generated from the previously established precise boundary segments in Figure 5.22.

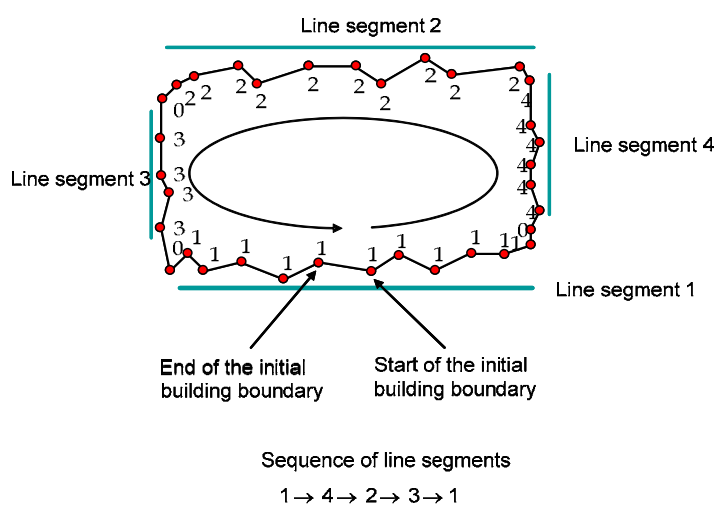


Figure 5.26: Establishing the proper sequence for the identified boundary segments.



Figure 5.27: Closed-polygon generated from the established precise boundary segments in Figure 5.22.

The boundary refinement and closed-polygon generation procedures are carried out for the individual building primitives one by one. The last step in the DBM generation process is the automated simultaneous co-alignment of the boundary segments for all the building primitives. To do this, it starts by defining a 2D adjacency table that identifies neighbouring building primitives, after the projection of their boundary segments onto a horizontal plane. Projecting the boundary segments onto a horizontal plane is necessary in order to identify neighbouring building primitives that may have different elevations (i.e., those that might share a vertical wall), as shown in Figure 5.28(a). In the adjacency table, two building primitives will be deemed neighbours if some of the boundary segments of one primitive are located within a buffer zone surrounding the boundaries of the other primitive. Then, for neighbouring building primitives, one investigates the proximity and the degree of parallelism of the boundary segments projected onto the horizontal plane. Boundary segments that meet pre-specified thresholds, which define the acceptable range of collinearity/parallelism, normal distance, and distance between the end points for two neighbouring boundary segments, will be merged through a straight-line fitting procedure. Finally, the merged lines are projected back onto their respective building primitive planes. As an illustration, Figure 5.28(a) shows the polygons defined for three building primitives, which are located at three different elevations. The boundary segments projected onto a horizontal plane are shown in Figure 5.28(b). Finally, the co-aligned boundaries are shown in Figure 5.28(c).

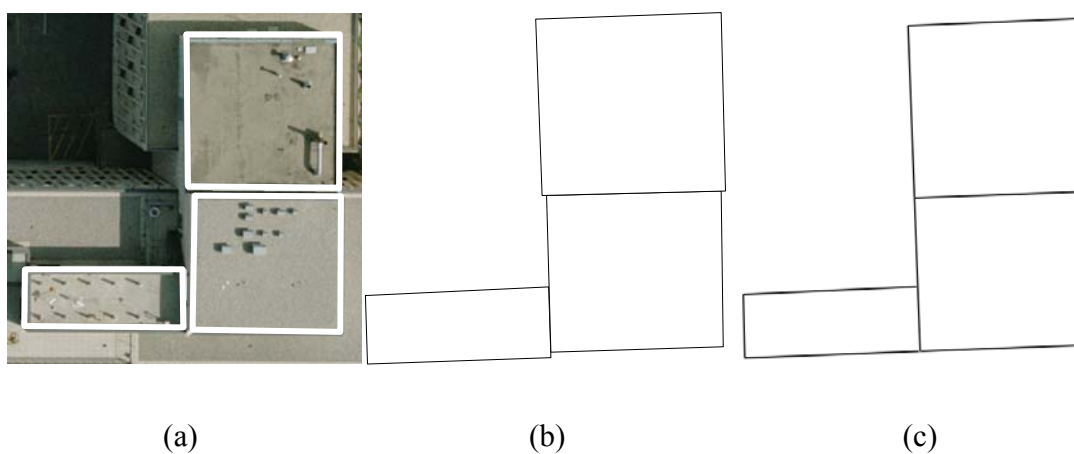


Figure 5.28: Closed-polygons for three building primitives at different elevations (a); boundary segments projected onto a horizontal plane (b); and co-aligned boundary segments (c).

After the boundary alignment procedure has been carried out, a DBM wire frame is generated by connecting the vertices of the co-aligned boundary segments along the building rooftops with other versions of these boundary vertices at the terrain elevation, which is defined as the average elevation of the neighbouring terrain points (i.e., the buildings' footprints). Figure 5.29(a) shows a DBM wire frame generated using the polygon in Figure 5.27. The wire frame is also converted into KML format, which can be directly imported to Google Earth; Figure 5.29(b).

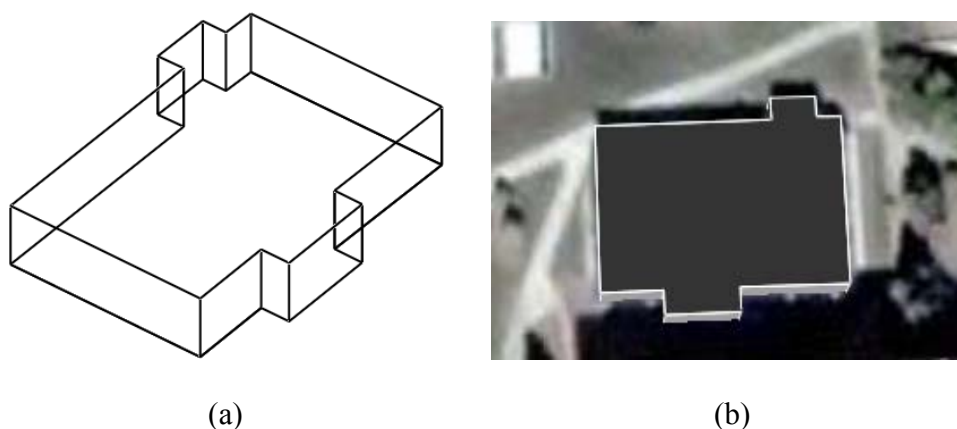


Figure 5.29: A generated DBM wire frame (using the polygon in Figure 5.27) (a) is imported to Google Earth (b).

So far in this chapter, an automated procedure has been introduced for the utilization of LiDAR and image data in the generation of precise boundary segments for each of the previously identified building primitives. For some situations (e.g., relief displacements, shadows, and/or lack of image contrast), the results of the procedure might have missing and/or erroneous boundary segments. Figure 5.30 shows an example of a closed-polygon with erroneous segments. The segments are located in the areas (A and B) enclosed by white dashed ellipses. The erroneous segment in area A is caused by a cooling fan on top of the roof. Erroneous boundary segment in area B is caused by shadows and low change in the spectral similarity measure on both side of the 3D matched line. To compensate for these situations, a manual mono-plotting procedure is introduced, in which the operator interactively deletes or adds boundary segments. The end points for missing boundary segments are measured in one image, and a mono-plotting procedure is used to project these measurements into the object space using the

established geo-referencing parameters, as well as the parameters defining the plane of the building primitive under investigation. It should be noted that the operator does not need to precisely measure the end points of the missing line segments (i.e., the operator needs to just make sure that the measured points lie along the line segments).

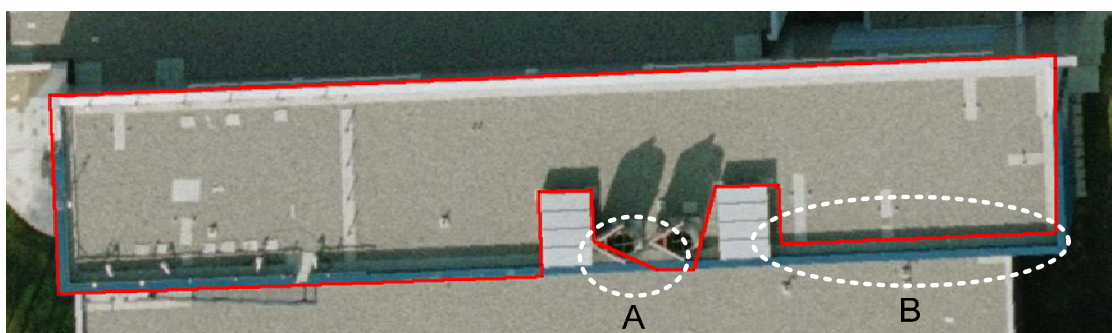


Figure 5.30: An example of closed-polygon with erroneous segments.

5.3 DSM Enhancement and Visualizations

Once the precise DBM has been produced, the enhanced surface model will be generated using the precise building boundary information from DBM. Two options for generating a new DSM can be proposed at this stage. More specifically, the new DSM can be generated by combining the derived DBM and either the original DSM or the DTM (which is generated using terrain LiDAR points separated from the original LiDAR points; refer to Chapter 4). Since two types of DSMs involve the derived DBM, both of them will have the improved surfaces around buildings. The only difference between the two DSMs will exist in the non-building areas. In other words, the DSM derived from the combination of the original DSM and DBM will still have the grid cells generated from

the LiDAR points scanned over small features such as cars, sculptures, and trees. On the other hand, the other DSM derived from the combination of the DTM and DBM will have changed elevations (i.e., the same level as the terrain areas) over the cells for the small features because the LiDAR points scanned over these features are separated from the terrain through the terrain and off-terrain classification process (refer to Chapter 4).

True orthophotos will be generated for 2D visualization, using three different types of DSMs (i.e., original DSM, DSM + DBM, and DTM + DBM) and the imagery involved, through the true orthophoto generation method proposed in Chapter 3. Figure 5.31, Figure 5.32, and Figure 5.33 show three different true orthophotos created using the three different types of DSMs. Also, a building (enlarged area enclosed by red box) in three different true orthophotos are shown in the figures. By comparing these figures, the qualities of the true orthophotos in Figure 5.32, and Figure 5.33 are obviously improved, especially for buildings, compared to the true orthophoto in Figure 5.31.

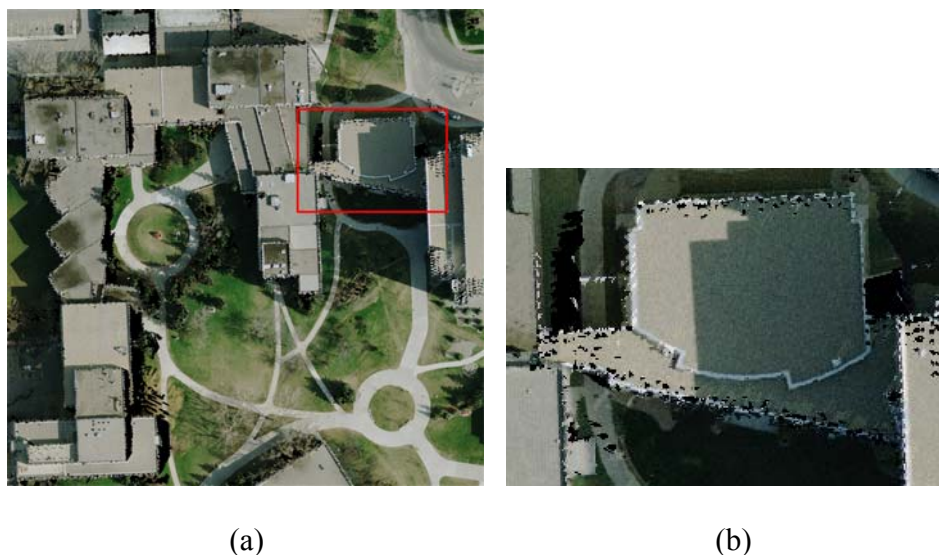


Figure 5.31: A true orthophoto created using the original DSM (a) and the enlarged area enclosed by red box (b).

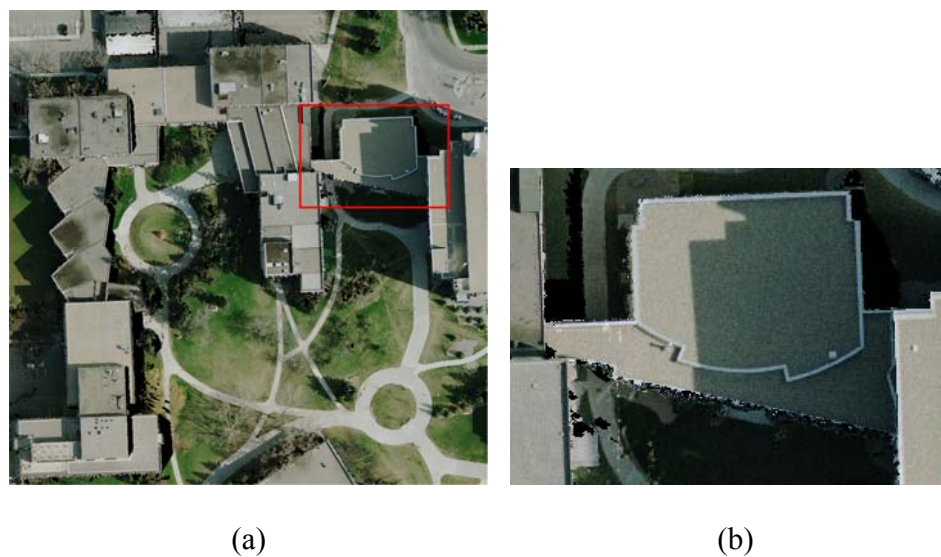


Figure 5.32: A true orthophoto created using a DSM obtained by adding the DBM to the original DSM (a) and the enlarged area enclosed by red box (b).

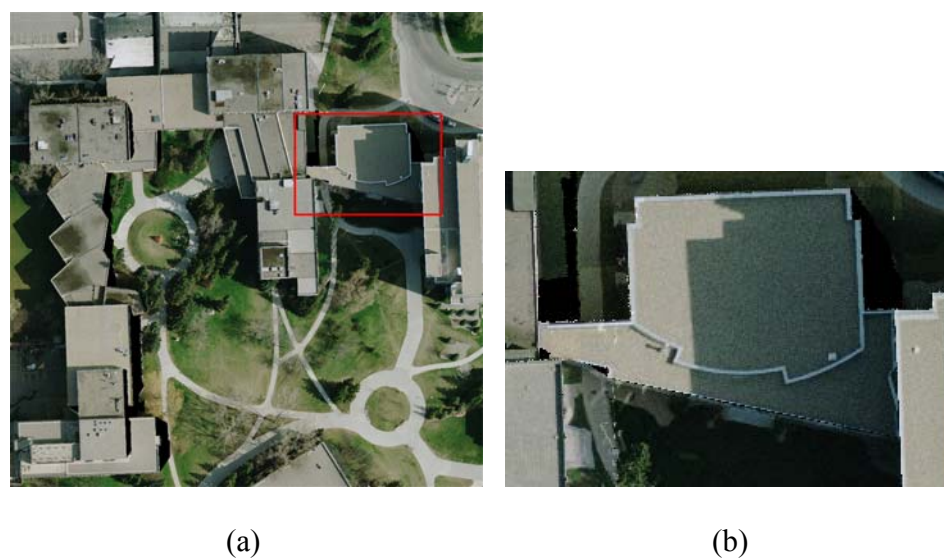


Figure 5.33: A true orthophoto created using a DSM obtained by adding the DBM to the DTM (a) and the enlarged area enclosed by red box (b).

Also, non-building areas in the two true orthophotos using the original DSM and a DSM obtained by adding the DBM to the DTM are compared in Figure 5.34. Small features in the true orthophotos created using the original DSM are shown in Figure 5.34 (a). Also, same features in the other true orthophoto created using a DSM obtained by adding the DBM to the DTM are shown in Figure 5.34 (b). As can be seen in the figures, the quality of the interpretation of the small features is obviously improved in Figure 5.34 (b).



(a)



(b)

Figure 5.34: Small features in the true orthophotos created using the original DSM (a) and using a DSM obtained by adding the DBM to the DTM (b).

Through the comparison of the true orthophotos created using different types of DSMs, it is proved that the true orthophoto created using a DSM obtained by adding the DBM to the DTM provides the best quality of true orthophoto either for buildings and non-building features. Also, 3D visualizations of the surfaces are produced by draping the true orthophotos over the corresponding DSMs. The quality of 3D visualization is also obviously improved in Figure 5.35 (b) compared to the one in Figure 5.35 (a).



(a)



(b)

Figure 5.35: A 3D visualizations produced using the original DSM (a) and a DSM obtained by adding the DBM to the DTM (b).

5.4 Summary

This chapter focused mainly on precise building reconstruction, followed by the enhancement of surface models and 2D/3D visualizations. Since the boundaries of the building primitives produced in Chapter 4 do not delineate precise breaklines, boundary segment refinement procedures were proposed to achieve precise building reconstruction.

For precise boundary generation, the integration of photogrammetric and LiDAR data was utilized to take an advantage of the synergistic properties of both datasets. More specifically, an object-based integration process was introduced in this research. By utilizing warped imagery derived through the object-based integration process, the image matching problem was resolved, since the incorporated LiDAR data worked as a constraint. In addition, spectral similarity transitions over the matched line segments extracted from the warped imagery were investigated to select precise boundary segments.

Since this research focuses on the urban environments with complex and connected buildings, there might be significant occlusions in the large scale imagery. The hierarchical projection approach was proposed to reconstruct boundary segments in the occluded areas. This process is designed for the building primitives that share a vertical wall but have different elevations. The reconstruction procedure was performed by projecting the boundary segments constructed for higher building primitives onto the lower and neighbouring ones. In addition, some of building boundary segments was acquired either by intersecting neighbouring building primitives or regularization process using the initial boundaries of building primitives. Then, all the derived boundary

segments were utilized to construct closed-polygons, followed by alignment. After the alignment procedure, a DBM wire frame was generated and utilized to produce an enhanced DSM. The enhanced DSM by adding the DBM and the DTM provided the best quality of visualizations either for buildings and non-building features.

Chapter 6 : Experiments and Results

6.1 Introduction

In the previous chapters, the methodologies within the framework for accurate reconstruction and visualization of urban environments were described in detail. Chapter 3 presented the prerequisite steps (namely, photogrammetric and LiDAR quality assurance and quality control) for the utilization of both photogrammetric and LiDAR data. Afterwards, the co-registration of the two datasets was conducted to align them to a common reference frame. To ensure that the co-registration procedure is of optimal quality, the LiDAR data is used as the source of control for image geo-referencing through the incorporation of linear and areal features. Then, two angle-based true orthophoto generation methods were proposed to relate the spectral and positional information in imagery and LiDAR data, respectively. Since the surface models produced from the original LiDAR data do not sufficiently represent building breaklines, Chapters 4 and 5 introduced a procedure to improve the quality of the surface models and visualizations. In Chapter 4, building hypotheses and primitives were generated using LiDAR data only. Afterwards, Chapter 5 focused on building reconstruction through the integration of photogrammetric and LiDAR data, followed by 2D and 3D visualizations. To validate the feasibility and evaluate the performance of the methodologies proposed in the previous chapters, the results of experiments using real LiDAR and image data are presented in this chapter. All the methods proposed in this research and other researchers' methods which are utilized to be compared with the proposed ones are implemented through programs generated by the author in either Microsoft Visual C++ or Matlab.

6.2 Dataset Description

Photogrammetric and LiDAR datasets used in this research were acquired around the University of Calgary campus in Calgary, Alberta, Canada. The LiDAR dataset (10 strips) was captured by an Optech 3100 system during two mapping missions at different flying heights (1,000m and 1,400m). The average point spacing for the combined data is approximately 0.75m (about 1.3 points per square meter). The planimetric accuracy specifications for the two flights are approximately 50cm and 70cm, respectively, while the vertical accuracy is expected to be approximately 15cm. Nine photos in three strips (with a scale of 1:5000) were captured by an analog camera – RC30, with a focal length of 153.33mm – at an average flying height of 770m. The photos were then digitally scanned at a resolution of 12 microns, resulting in a 6cm GSD. The expected planimetric and vertical accuracies from the photogrammetric data are 6cm and 14cm, respectively. Figure 6.1 shows the configuration of the nine photos (delineated by rectangles in the figure) overlaid on the captured LiDAR data. Strip adjustment of the LiDAR strips is conducted after identifying inconsistency between the strips through the LiDAR quality control process.

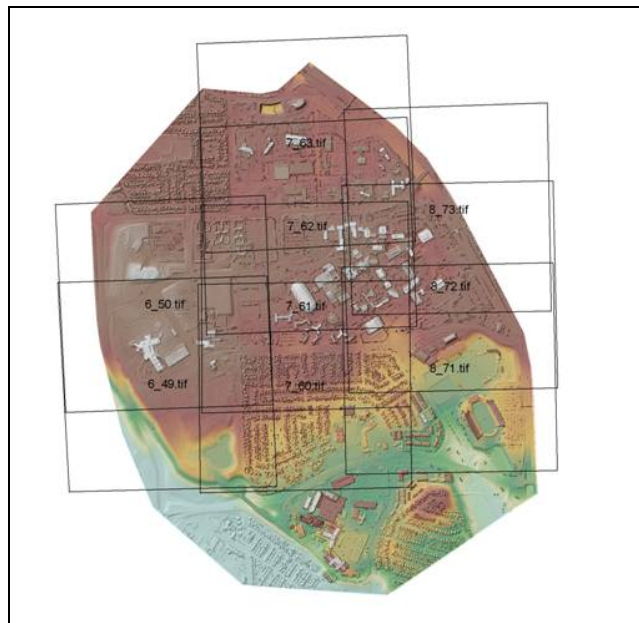


Figure 6.1: Nine overlapping aerial photos overlaid on the LiDAR data.

6.3 Co-registration

Once both datasets have been acquired, the co-registration procedure is conducted by using the LiDAR data as the source of control for image geo-referencing. As explained in Chapter 3, compatible geo-referencing results are obtained using areal or linear LiDAR control features. Hence, the geo-referencing results obtained using linear features are utilized for this experiment. Fifty control lines and forty eight tie points are used in the geo-referencing procedure. Figure 6.2 shows the locations of the control lines (red lines in the figure) in the LiDAR dataset.

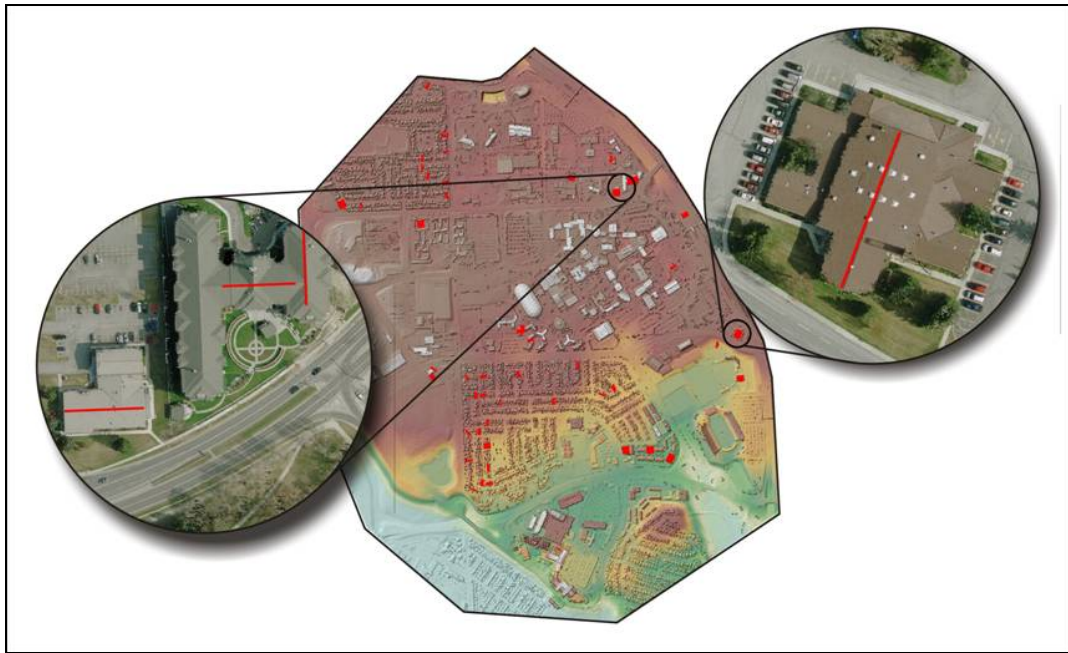


Figure 6.2: Locations of the control lines in the LiDAR dataset.

A stereo-pair out of 9 aerial images and corresponding LiDAR data were selected over the area of interest. As an example of the geo-referencing results, the EOPs and variance-correlation matrices of two overlapping aerial photos (denoted as the left and right images) covering an area containing complex and connected buildings are shown in Tables 6.1, 6.2, and 6.3. As can be seen in Table 6.2 and Table 6.3, all the parameters have been determined with high precision and there are no significant correlations among them. Minimum and maximum standard deviations of the attitude are ± 13 sec and ± 19 sec, respectively. Also, minimum and maximum standard deviations of the position are ± 0.049 m and ± 0.099 m, respectively.

Table 6.1 Estimated EOPs for the left and right images

	$\omega(\text{deg})$	$\phi(\text{deg})$	$\kappa(\text{deg})$	$X_o(m)$	$Y_o(m)$	$Z_o(m)$
Left image	-0.1507	1.3902	90.8894	700663.343	5662238.902	1903.608
Right image	0.1478	0.2004	92.5189	700656.238	5662696.694	1906.933

Table 6.2 Variance-correlation matrix for the left image

	$\omega(\text{sec}^2)$	$\phi(\text{sec}^2)$	$\kappa(\text{sec}^2)$	$X_o(m^2)$	$Y_o(m^2)$	$Z_o(m^2)$
$\omega(\text{sec}^2)$	$(\pm 14.20)^2$	-0.03	-0.08	0.01	-0.83	-0.07
$\phi(\text{sec}^2)$	-0.03	$(\pm 15.43)^2$	-0.01	0.81	0.02	-0.02
$\kappa(\text{sec}^2)$	-0.08	-0.01	$(\pm 12.82)^2$	-0.05	0.17	-0.02
$X_o(m^2)$	0.01	0.81	-0.05	$(\pm 0.083)^2$	0.03	-0.10
$Y_o(m^2)$	-0.83	0.02	0.17	0.03	$(\pm 0.084)^2$	0.07
$Z_o(m^2)$	-0.07	-0.02	-0.02	-0.1	0.07	$(\pm 0.049)^2$

Table 6.3 Variance-correlation matrix for the right image

	$\omega(\text{sec}^2)$	$\phi(\text{sec}^2)$	$\kappa(\text{sec}^2)$	$X_o(m^2)$	$Y_o(m^2)$	$Z_o(m^2)$
$\omega(\text{sec}^2)$	$(\pm 19.04)^2$	0.00	-0.03	0.04	-0.84	0.17
$\phi(\text{sec}^2)$	0.00	$(\pm 17.30)^2$	-0.19	0.81	-0.02	0.01
$\kappa(\text{sec}^2)$	-0.03	-0.19	$(\pm 13.65)^2$	-0.45	0.11	-0.03
$X_o(m^2)$	0.04	0.81	-0.45	$(\pm 0.098)^2$	-0.08	-0.02
$Y_o(m^2)$	-0.84	-0.02	0.11	-0.08	$(\pm 0.099)^2$	0.02
$Z_o(m^2)$	0.17	0.01	-0.03	-0.02	0.02	$(\pm 0.055)^2$

To investigate the precision of an object point that has been reconstructed through the geo-referencing process, one of the tie points located among the complex and connected buildings is selected and its standard deviations and correlation matrices are

examined. One should note that these standard deviations and correlation matrices of the tie points are derived through the bundle adjustment process while treating these points as unknowns. The standard deviations of the X, Y, and Z coordinates of such a representative tie point are about ± 6 cm, ± 6 cm, and ± 5 cm, respectively. The calculated standard deviations of the object point coordinates encompass the effects of noise in the Exterior Orientation Parameters (EOP), IOP, image point measurements, and LiDAR control lines.

6.4 Building Hypothesis and Primitive Generation

Once the co-registration process has been completed for the whole dataset, an area of interest that contains complex and connected buildings is selected to carefully evaluate the performance of the proposed methodologies, from building detection to visualizations. Figure 6.3(a) and Figure 6.3(b) show a portion of the image and LiDAR data gathered in this area. As shown in Figure 6.3 (a), this area has buildings, as well as some trees and mild terrain variation. The LiDAR points in Figure 6.3 (b) are assigned different colours according to their heights.

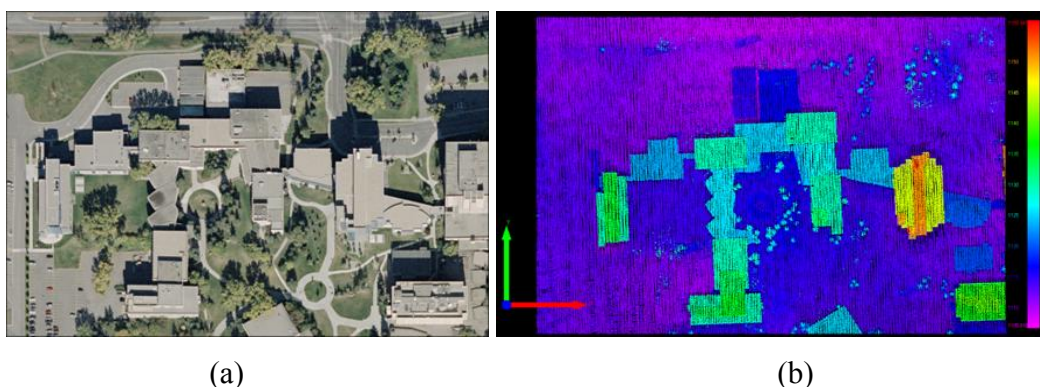


Figure 6.3: Aerial photo over the area of interest (a), and LiDAR points over the same area (b).

For building detection, the LiDAR points are classified as terrain or off-terrain points (Figure 6.4 (a)). The points in blue and red are terrain and off-terrain points, respectively. Then, the off-terrain points are further classified as points belonging to planar or rough surfaces. Neighbouring points that belong to planar surfaces are grouped, and the resulting groups are used to identify instances of buildings in the LiDAR data, as shown in Figure 6.4 (b). Points with different colours belong to different building hypotheses (it should be noted that some colours are repeated due to the limited number of colours in the display function). Descriptions, values, and justifications for the thresholds used for terrain/off-terrain point classification and building hypothesis generation are provided in Table 6.4 and Table 6.5, respectively.

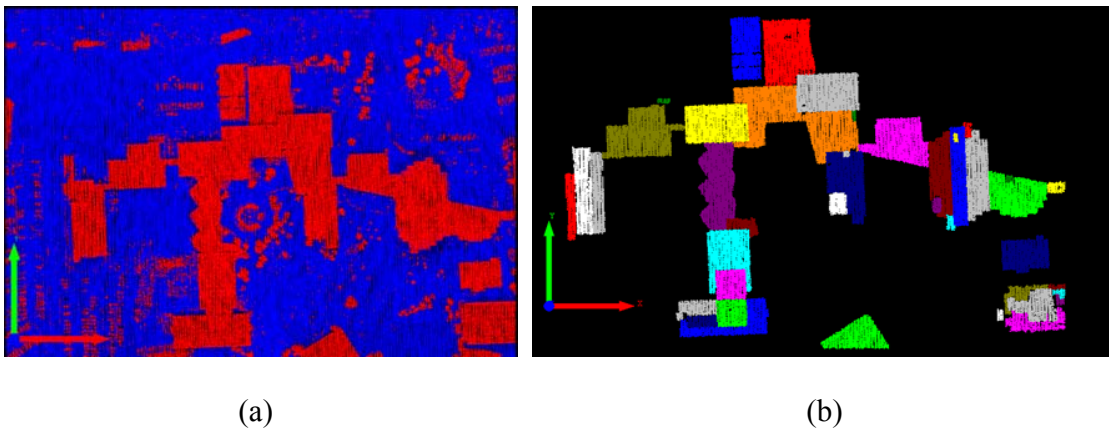


Figure 6.4: Classified off-terrain points in red (a), and generated building hypotheses (b).

Table 6.4 Descriptions, values, and justifications for the thresholds used for terrain and off-terrain point classification

Threshold	Description	Value	Justification	Section
DSM cell size	DSM cell size	0.8m	Approximately equal to the average point spacing of the LiDAR data	Section 4.2.1
Height of projection center	Height of synthesized projection center	Max height of DSM + 50m	Slightly higher than the highest elevation in the DSM to ensure significant occlusion	Section 4.2.2
Horizontal distance of projection center	Horizontal distance of projection center away from the DSM	150m away from the DSM boundary	Large enough distance to ensure significant difference between the off-nadir angle of the last visible point and the off-nadir angle of the first occluded point	Section 4.2.2
Statistical parameter for terrain points	Standard deviation scaling factor of the terrain points for the identification of terrain points	1.5	Probability of having a terrain point elevation that is less than $\mu_{\text{terrain}} + 1.5 \sigma_{\text{terrain}}$ is 93%, which is quite high	Section 4.2.3
Statistical parameter for off-terrain points	Standard deviation scaling factor of the terrain points for the identification of off-terrain points	2.0	Probability of having a terrain point elevation that is larger than $\mu_{\text{terrain}} + 2.0 \sigma_{\text{terrain}}$ is 2%, which is quite low	Section 4.2.3

Table 6.5 Descriptions, values, and justifications for the thresholds used for building hypothesis generation

Threshold	Description	Value	Justification	Section and Figure
Search radius	Radius of the spherical neighbourhood centered at a given off-terrain point	1.5m	Including enough number of points to define reliable attributes, “planar parameters”	Section 4.3 Figure 4.12
Final plane buffer	Buffer defined above and below the final fitted plane	0.4m above and below the final plane; total 0.8m	About 2 times the vertical accuracy of the LiDAR data (covering 95% of the LiDAR points on the plane)	Section 4.3 Figure 4.12
Planarity ratio	Ratio threshold to identify points that belong to a planar surface	0.95	Covers 95% of the LiDAR points on the plane	Section 4.3 Figure 4.13
Min building area	Minimum building area, used to discard small point groups	9m ²	Prior knowledge about building’s size with the area of interest	Section 4.3
Building height threshold	Building height threshold, used to discard point groups at lower heights	4.5m	Prior knowledge about building’s height with the area of interest	Section 4.3

Once the building hypotheses have been generated, the segmentation procedure is applied to each of the hypotheses to cluster the point cloud into several groups that correspond to the individual planar patches (i.e., the building primitives), as shown in Figure 6.5 (a). In the figure, the area enclosed by a solid white ellipse contains the building primitives produced from a single building hypothesis. Finally, the minimum convex hull procedure is applied to identify the initial boundaries of the building primitives, as seen in Figure 6.5 (b). Couple of initial boundaries of the building primitives are projected onto the corresponding images to illustrate deviation and closeness between the LiDAR boundaries and the actual boundaries in Figure 6.6. Descriptions, values, and justifications for the thresholds used to generate the building primitives and their initial boundaries are provided in Table 6.6.



Figure 6.5: Clustered building primitives (a), and the initial boundaries of the building primitives (b).

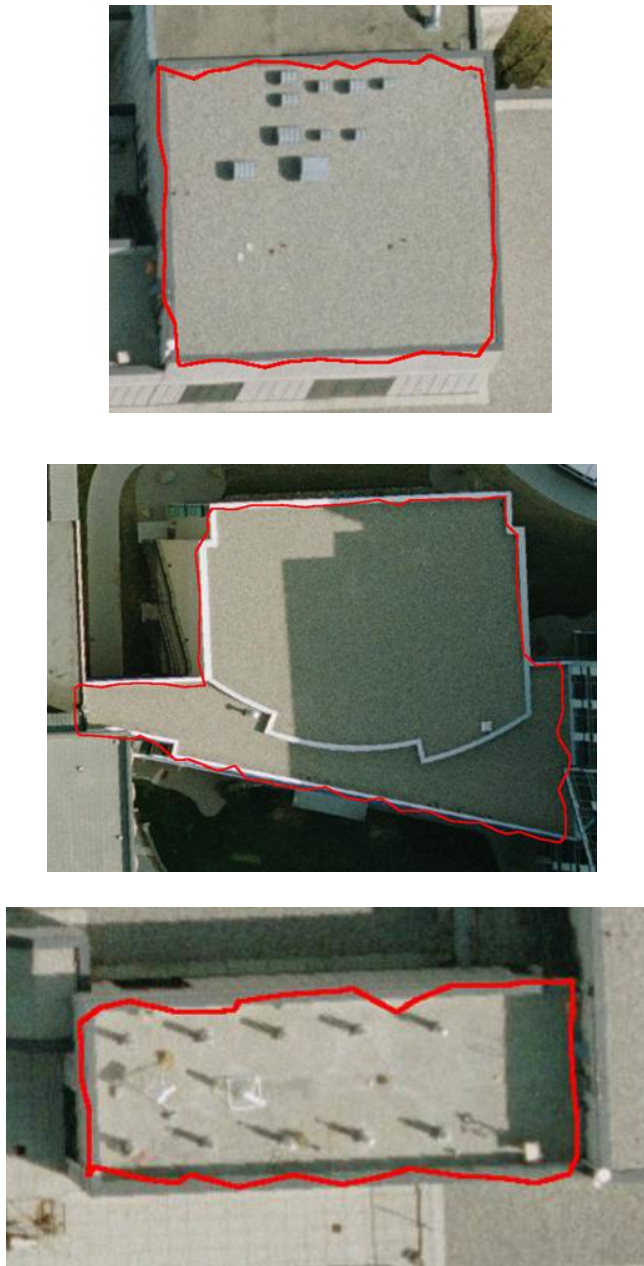


Figure 6.6: Examples illustrating the deviation and closeness between the initial boundary of the building primitives and the actual building boundaries.

Table 6.6 Descriptions, values, and justifications for the thresholds used for the generation of building primitives and their initial boundaries

Threshold	Description	Value	Justification	Section and Figure
Search radius	Radius of the spherical neighbourhood centered at a point	1.5m	Including enough number of points to define reliable attributes, “planar parameters”	Section 4.4.1
Final plane buffer	Buffer defined above and below the final fitted plane	0.4m above and below the final plane; total 0.8m	Two times the vertical accuracy of the LiDAR data (covering 95% of the LiDAR points on the plane)	Section 4.4.1
Coplanarity test threshold	Threshold for testing the coplanarity of points at the peak of the accumulator array	0.2m	Approximately equal to the vertical accuracy of the LiDAR data	Section 4.4.1
Proximity threshold	Maximum distance for determining the proximity among points in the object space	1.0m	Approximately equal to the average point spacing of the LiDAR data	Section 4.4.1
Minimum size of cluster	Minimum size of a derived point cluster	9m ²	Prior knowledge about building’s size within the area of interest	Section 4.4.1
Modified Convex hull radius	Radius of the neighbourhood used for the modified convex hull method	Min: 2m Max: 3m	Two to three times the average point spacing of the LiDAR data	Section 4.4.2 Figure 4.23

6.5 Building Reconstruction and Visualizations

In the next processing phase, the initial boundaries of the building primitives are refined through the proposed building reconstruction procedures. The refinement of the initial boundaries begins with the acquisition of boundary segments through the intersection of neighbouring planar patches. Since the area of interest used here does not include gable roofs, the author does not provide the line segment results generated from the intersection process (Please refer to the line segment result in Figure 5.7, which was derived using another dataset). Descriptions, values, and justifications for the thresholds used for precise boundary generation through the intersection of neighbouring planar patches are provided in Table 6.7.

Once the precise boundary segments have been derived through the intersection of neighbouring planar patches (if any exist), the initial boundaries of the building primitives are refined through the incorporation of stereo-imagery. The refinement process (i.e., the determination of the precise boundary segments for a given building primitive) utilizes the initial boundaries of the primitive, the parameters of the plane fitted through the segmented point cloud, the image geo-referencing parameters, and the straight-line segments detected in the imagery. Recall that this research deals with urban environments with complex and connected building structures. Hence, some boundary portions may be missed due to occlusions caused by the presence of higher neighbouring buildings. The missing portions of the boundaries are reconstructed by projecting the boundary segments constructed for the higher building primitives onto the lower neighbouring ones when these primitives share common vertical walls. Afterward, the regularization of the initial boundaries of the building primitives is applied if any portions

of the boundaries are still missing. Once all the boundary segments for a building primitive have been generated, a closed-polygon is generated using these boundary segments established from the above procedures. Finally, all the boundary segments of the closed-polygons in the study area are aligned simultaneously. Table 6.8 provides descriptions, values, and justifications for the thresholds used for precise boundary generation through the processes of integration, projection, and regularization.

Table 6.7 Descriptions, values, and justifications for the thresholds used for precise boundary generation through the intersection of neighbouring planar patches

Threshold	Description	Value	Justification	Section and Figure
Angle threshold	Angle between the surface normal vectors of neighbouring primitives	20 degrees	Avoids the intersection of planes that are almost parallel	Section 5.2.1
Normal distance threshold	Normal distance to identify the points close to the intersection line; the identified points are projected on the line to detect gaps and extreme points along the line	1.5m	About twice the average point spacing of the LiDAR data	Section 5.2.1 Figure 5.5
Gap threshold	Gap threshold to identify significant gap between the adjacent projected points along the intersection line	1.0m	Prior knowledge of buildings and the average point spacing of the LiDAR data	Section 5.2.1 Figure 5.6

Table 6.8 Descriptions, values, and justifications for the thresholds used for precise boundary generation through the processes of integration, projection, and regularization

Threshold	Description	Value	Justification	Section and Figure
Edge detection buffer	Size of the buffer on each side of the initial boundary, used for edge detection	1.0m	Approximately equivalent to the average point spacing of the LiDAR data (on each side of the initial boundary)	Section 5.2.2
Matching angle	Acceptable angle between candidate line segments in the matching process	6 degrees	Considers the geo-referencing results and the noise level of the edge detection results	Section 5.2.2 Figure 5.13
Matching normal distance	Acceptable normal distance between candidate line segments in the matching process	0.5m	Considers the geo-referencing results and the noise level of the edge detection results	Section 5.2.2 Figure 5.13
Ratio for filtering matched lines	Ration to detect matched lines following the trend of the initial boundary	0.6	Considers the noise level of the initial boundary results	Section 5.2.2 Figure 5.15
Matched line grouping angle	Angle threshold for grouping 3D matched lines	6 degrees	Considers the geo-referencing results and the noise level of the edge detection results	Section 5.2.2 Figure 5.17
Matched line grouping normal distance	Normal distance threshold for grouping 3D matched lines	1.0m	Approximately equal to the edge detection buffer size	Section 5.2.2 Figure 5.17
Buffer for outmost regions	Buffer size for reliable spectral similarity measure derivation in precise boundary segment selection	2.0m	Large enough to generate significant spectral similarity measure transitions	Section 5.2.2 Figure 5.21
Normal distance for regularization	Buffer for the regularization of the initial boundaries(Douglas-Peucker threshold)	1.0m	Prior knowledge of buildings and the average point spacing of the LiDAR data	Section 5.2.2

Figure 6.7 to Figure 6.10 show the initial and refined boundaries for four building primitives projected onto the left and right warped images. Also, Figure 6.8 (a), Figure 6.9 (a), and Figure 6.10 (a) show the line segments belonging to the higher and neighbouring building primitives. These building primitives are selected to qualitatively assess the performance of the boundary refinement procedure for different levels of building complexity. The improvement in the boundary segments gained through the proposed refinement process can be verified by comparing the initial and refined boundaries as well as the closeness to the actual building primitive boundary. One should note that the boundary segments derived through the integration and projection processes are denoted as IL and PL, respectively. Figure 6.7 shows an example of a simple building primitive. All four line segments (IL1 - IL4) are extracted through the boundary refinement process based on the integration of the imagery and LiDAR data. Figure 6.8 shows an example of a building primitive with low complexity. Five line segments (IL1 - IL5) are extracted through the boundary refinement process based on the integration of the imagery and LiDAR data. In addition, three line segments (PL1 - PL3) are derived by projecting the boundary segments (IL1 - IL3 of BP1) of a higher and neighbouring building primitive (BP1 located at the right side of Figure 6.8 (a)) onto the building primitive in question. Figure 6.9 and Figure 6.10 provide examples of boundary refinement for building primitives with medium and high complexity. The building primitive with medium complexity (Figure 6.9) is reconstructed using 15 IL and 2 PL segments (projected from two different building primitives, BP1 and BP2 in Figure 6.9 (a)). More specifically, PL1 and PL2 are derived by projecting IL1 of BP1 and IL2 of BP2 onto the current building primitive, respectively. On the other hand, the building

primitive with high complexity (Figure 6.10) is reconstructed using 8 IL and 5 PL segments (projected from three different building primitives, BP1, BP2, and BP3 in Figure 6.10 (a)). More specifically, PL1, PL2, PL3, PL4, and PL5 are derived by projecting IL1 of BP3, IL1 of BP2, IL1 of BP1, IL2 of BP1, and IL3 of BP1 onto the current building primitive, respectively. As shown in the figures, the IL boundary segments are detected precisely through the refinement process using the integrated imagery and LiDAR data. Moreover, the occlusion problem is solved by hierarchically projecting the building boundary segments belonging to higher primitives onto the lower one under investigation (i.e., creating PL segments). One should note that the use of the projection process for boundary segment reconstruction provides a way to overcome the problem of inaccurate boundary creation due to occlusions (which are particularly significant in urban environments). As a final product of the automated building reconstruction process, the DBM is generated and converted to KML format, which can be directly imported to Google Earth, as shown in Figure 6.11.

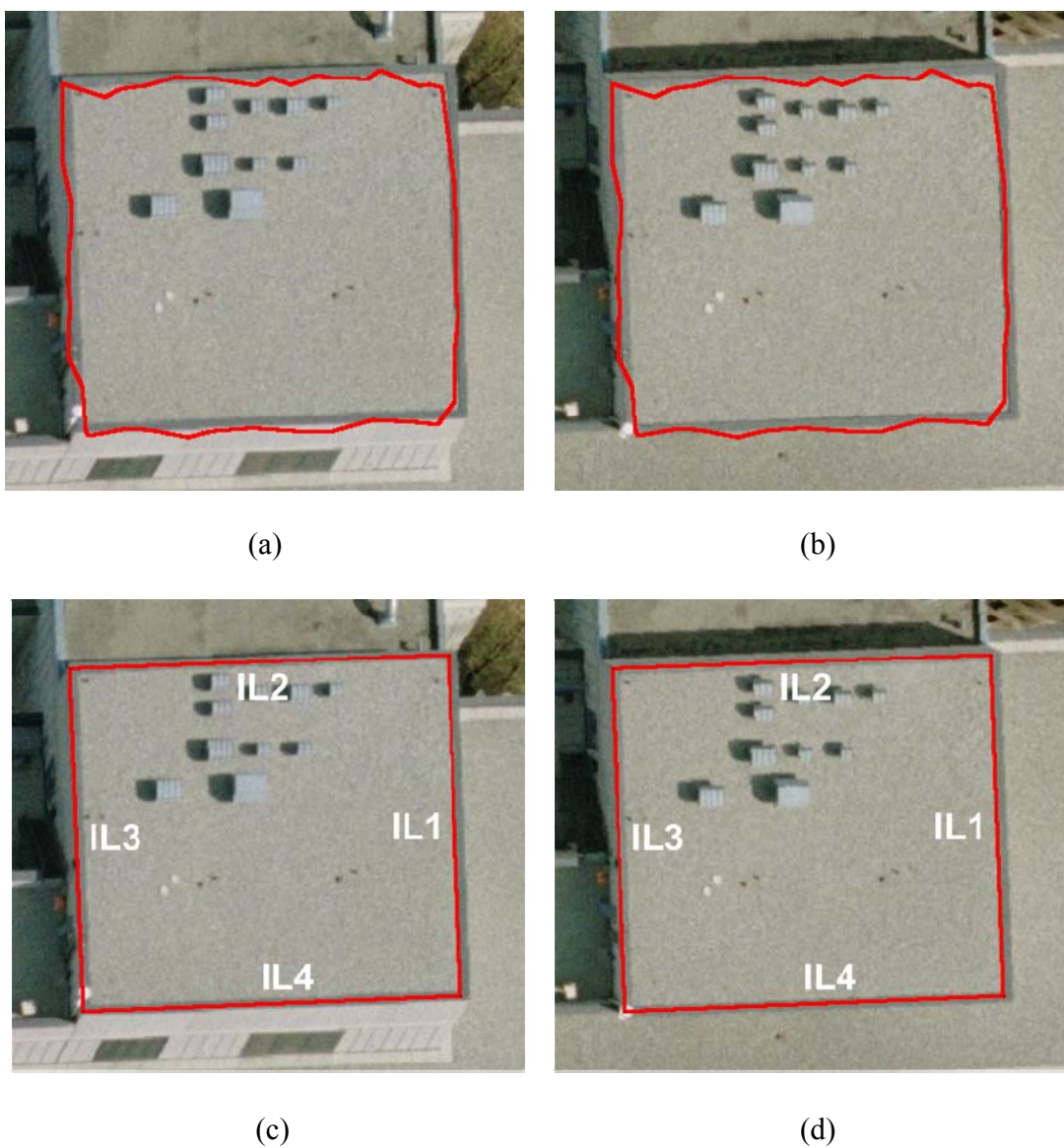


Figure 6.7: An example of a simple building primitive: initial boundary projected onto the left (a) and right (b) warped images; refined boundary projected onto the left (c) and right (d) warped images.

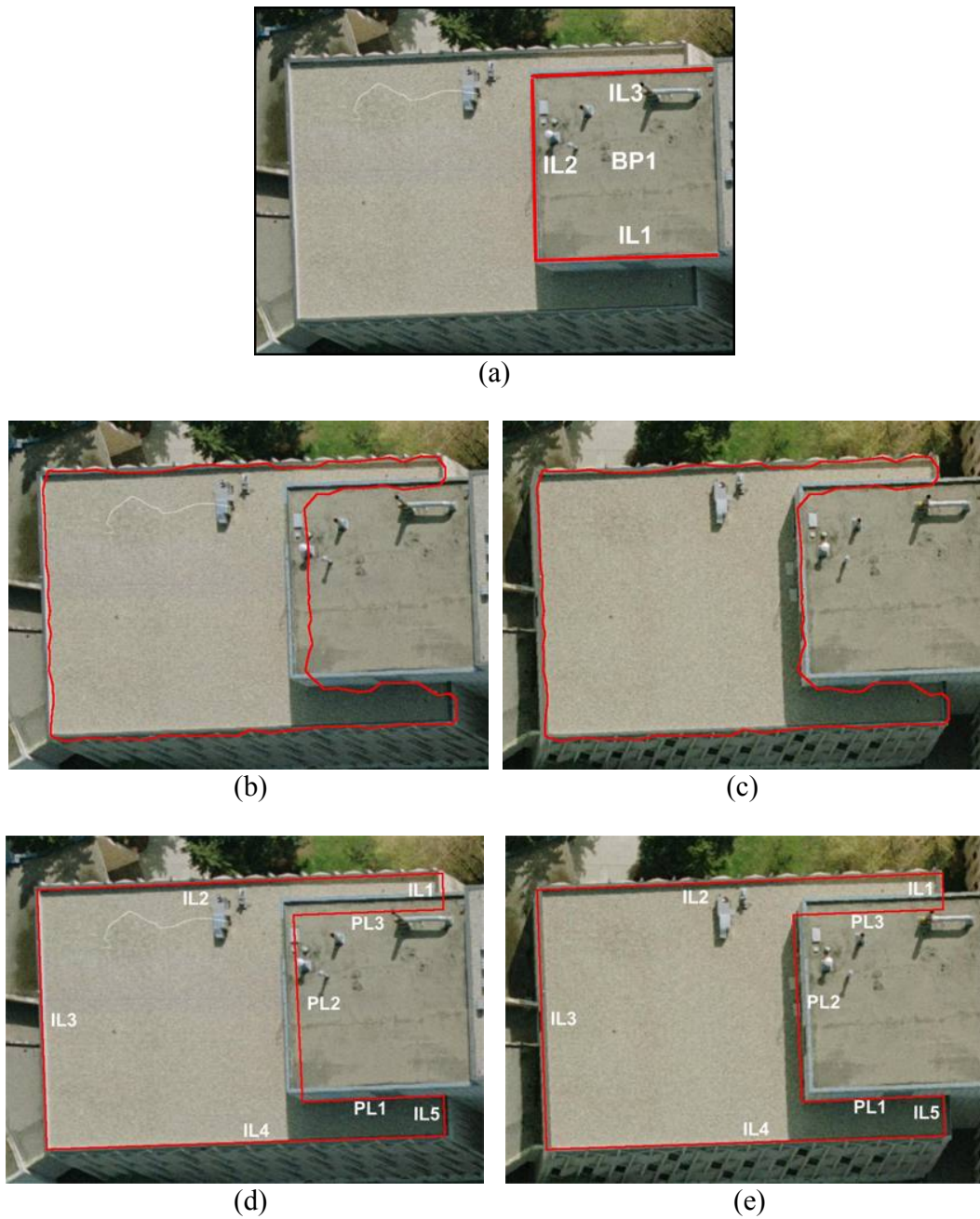


Figure 6.8: An example of a building primitive with low complexity: derived line segments for the higher and neighbouring building primitive (a); initial boundary projected onto the left (b) and right (c) warped images; and refined boundary projected onto the left (d) and right (e) warped images.



(a)



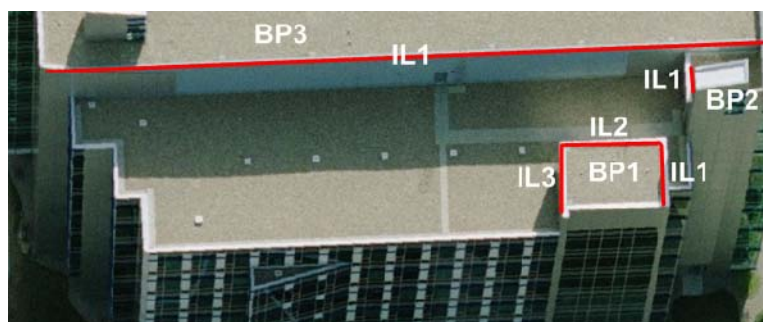
(b)

(c)

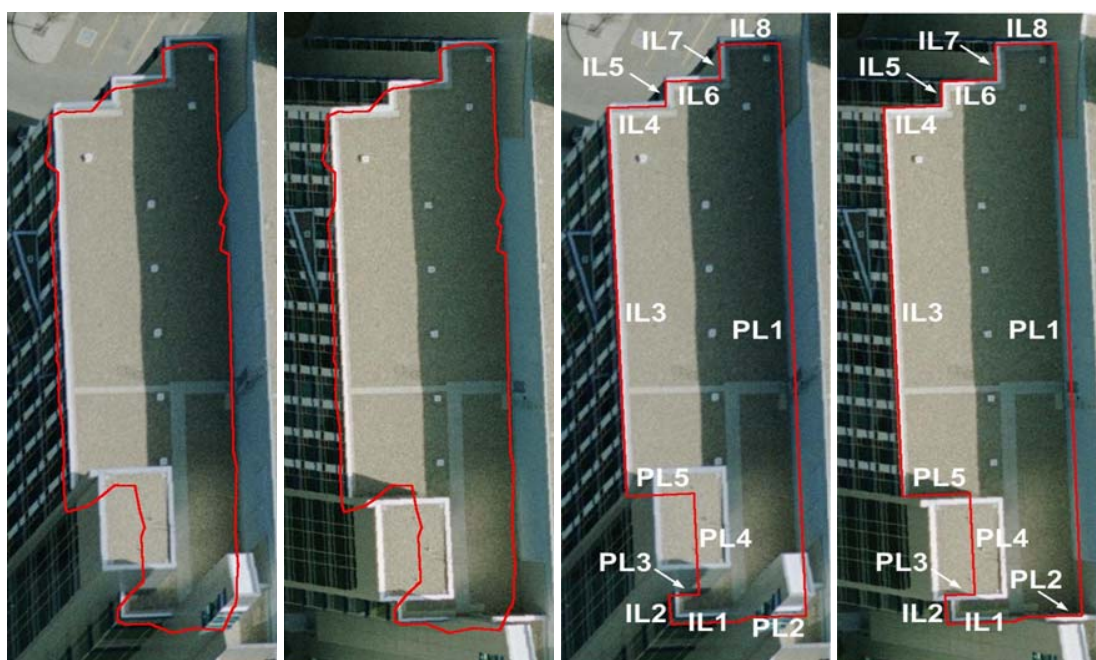
(d)

(e)

Figure 6.9: An example of a building primitive with medium complexity: derived line segments for the higher and neighbouring building primitives (a); initial boundary projected onto the left (b) and right (c) warped images; and refined boundary projected onto the left (d) and right (e) warped images.



(a)



(b)

(c)

(d)

(e)

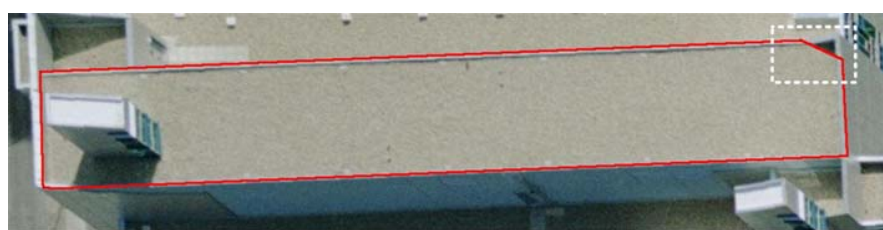
Figure 6.10: An example of a building primitive with high complexity: derived line segments for the higher and neighbouring building primitives (a); initial boundary projected onto the left (b) and right (c) warped images; and refined boundary projected onto the left (d) and right (e) warped images.



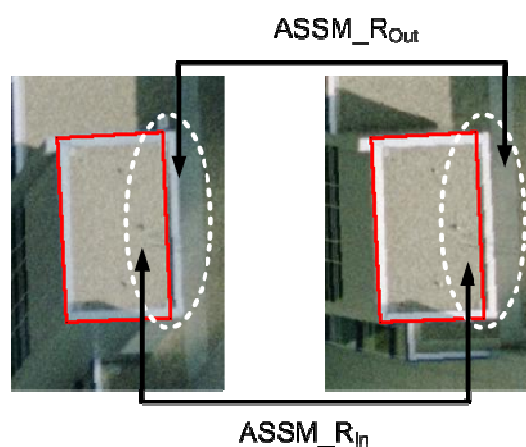
Figure 6.11: Initial DBM (in KML format) produced through the automated building reconstruction process.

The DBM produced through the automated building reconstruction procedure might include incorrectly detected boundary segments. Several examples of the erroneous boundary segments are shown in Figure 6.12. The line segment in the area bounded by the white box in Figure 6.12(a) is produced by the edges of the shadow around the fence on the rooftop. Since the shadow is located on top of the building primitive, the probability that the line of the shadow will be detected as a boundary segment is relatively high. On the other hand, Figure 6.12(b) and (c) exemplifies a different type of erroneous boundary segment, which is caused by a weak similarity transition from one region to another. In other words, the difference between $ASSM_{R_{In}}$ and $ASSM_{R_{Out}}$ is significantly small (check the line segment and surrounding region enclosed by the white dashed ellipse). The regions on either side of the line segment in question are almost homogeneous in the left and right warped images. Edge lines which are parallel to the base line (i.e., a line connecting two perspective centers) and with uniform texture on

both sides might cause such a problem. This will lead to the weak similarity transition from one side of the line segment to the other. Eventually, this weak transition makes the precise boundary segment selection process function inaccurately. The automatically established DBM includes these kinds of erroneous segments, which are handled through the manual editing procedure to produce the final DBM. Figure 6.13 shows the final DBM generated after manual editing of the initial DBM, which is established through the automated process. The areas with significant changes after manual editing are highlighted by red circles in Figure 6.11 and Figure 6.13.



(a)



(b)

(c)

Figure 6.12: Erroneous boundary segments produced through the refinement process due to shadow (a) and a weak similarity transition in the left (b) and right (c) warped images.



Figure 6.13: Final DBM (in KML format) after manual editing of the initial DBM, which is produced through the automated process.

Once the precise DBM has been acquired after the manual editing process, the enhancement of the DSM is done by combining the DTM and the final DBM, as shown in Figure 6.14. Then, a 2D visualization is produced by generating true orthophotos for the entire study area using the enhanced DSM and the corresponding imagery (Figure 6.15). Afterwards, the true orthophoto is draped over the enhanced DSM for 3D visualization as in Figure 6.16. To compare the qualities of the true orthophotos and 3D visualizations before and after DSM enhancement, couple of areas are selected and zoomed in (Figure 6.17 and Figure 6.18). Through this comparison, the quality of the visualization products after DSM enhancement is obviously improved when compared to that before DSM enhancement.

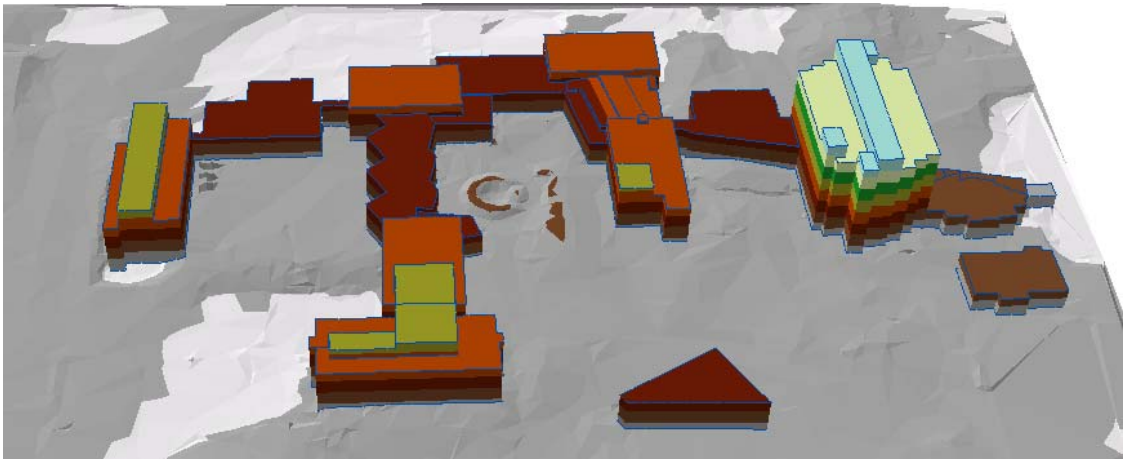


Figure 6.14: The enhanced DSM produced by combining the DTM and the final DBM.

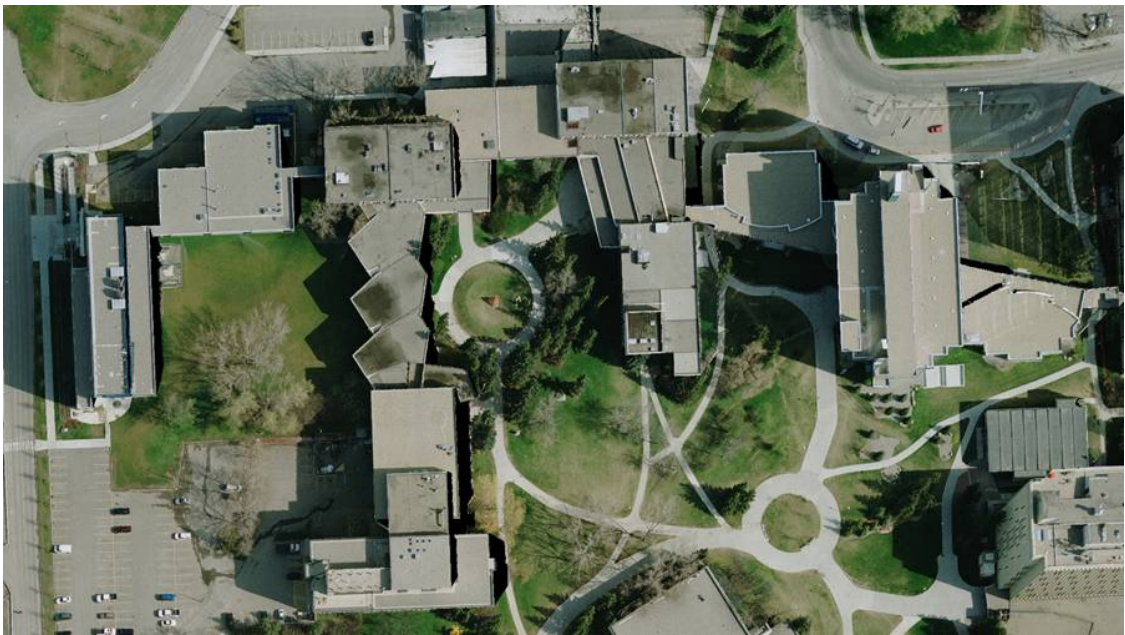


Figure 6.15: A true orthophoto produced using the enhanced DSM and the imagery involved.



Figure 6.16: A 3D visualization produced by draping the true orthophoto over the enhanced DSM.

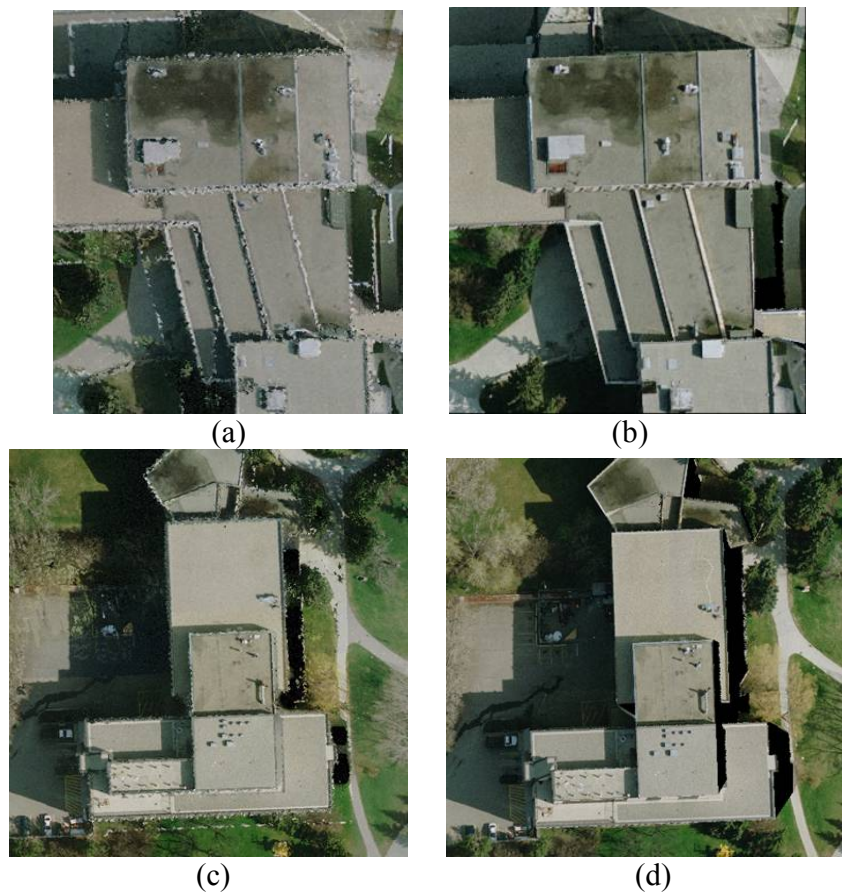


Figure 6.17: Enlarged areas from true orthophotos before (a & c) and after DSM enhancement (b & d).

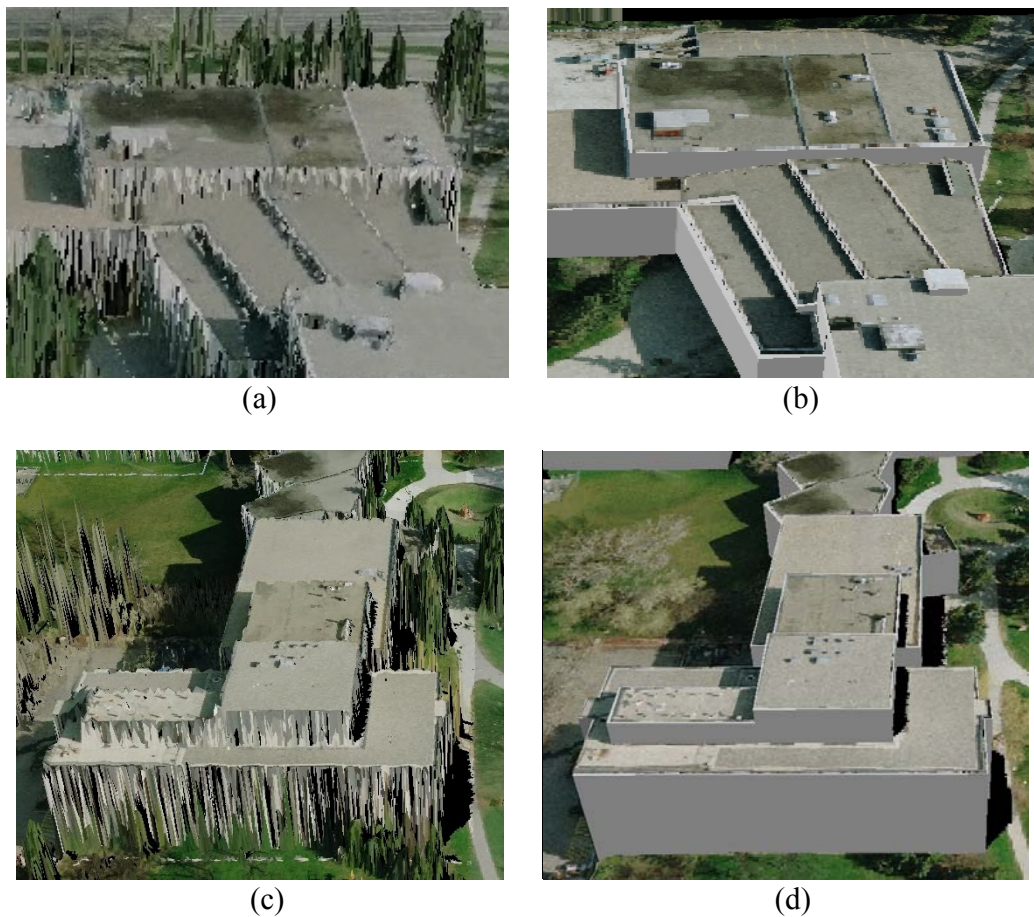


Figure 6.18: Enlarged areas from 3D visualizations before (a & c) and after DSM enhancement (b & d).

6.6 Quantitative Analysis

This part of the experimental results provides a quantitative evaluation of the correctness, completeness, and accuracy of the proposed DBM generation process. One should note that only the automatically-established boundary segments are considered for the quantitative evaluation of the results. The correctness and completeness measures introduced by Heipke et al. (1997) are adopted for this evaluation. The correctness of the

results is defined as the ratio of the number of correctly determined boundary segments to the total number of established boundary segments. In other words, the correctness measure evaluates the percentage of erroneous boundary segments among the established boundary segments. The completeness of the results, on the other hand, is defined as the ratio of the number of correctly established boundary segments to the total number of boundary segments necessary to represent the buildings in the study area. More specifically, the completeness measure gives an indication of the percentage of boundary segments that are missing or erroneous (i.e., those that should be interactively established through the manual editing procedure). The study area has a total of 40 building primitives, which are represented by 291 boundary segments. The proposed procedure produced 311 boundary segments for all the building primitives. Among the boundary segments produced, 276 boundary segments were correctly established. Based on these numbers, the correctness and completeness ratios for this study area are 89% (276/311) and 95% (276/291), respectively.

As for assessing the accuracy of the established DBM, the coordinates of the DBM corner points are compared with those derived manually using a photogrammetric reconstruction procedure. To get an idea of the quality of the manually derived coordinates, two operators were asked to derive the ground coordinates of the vertices of the building rooftops in the study area. The second column in Table 6.9 shows the means, standard deviations, and Root Mean Squared Error (RMSE) values for the differences between the coordinates derived by each of the two operators. Based on the mean values, one can see that there are no systematic discrepancies between the coordinates derived by

the two operators. The planimetric RMSE values are in the range of six pixels, which is mainly due to the difficulty of accurately pinpointing the corner points in the imagery.

Having established the accuracy expected from a manual operation, the coordinates derived from the proposed procedure were compared with the averages of the coordinates determined by the two operators. The statistics derived from this comparison are reported in the third column of Table 6.9. It should be noted that the comparison did not involve any of the vertices that are partially or fully defined through the manual mono-plotting procedure (i.e., only corner points between automatically-established boundary segments were considered). The reported planimetric means, standard deviations, and RMSE values in the third column are quite close to the results provided by the two operators, which indicates very high accuracy of the derived coordinates. The standard deviations derived from both of the manual and automatic ways are relatively higher than the expected accuracies addressed in Section 6.2 due to the identification problem of the building corner points. The vertical measures, on the other hand, seem to be much worse. The reason for this deterioration is that most of the buildings in the study area had fences on their rooftops, as seen in Figure 6.19. The heights of these fences range from 0.5m to 1.0m. The operators defined the corners of the DBM on top of the fences (Figure 6.19 shows the points selected by the operators), whereas the proposed procedure placed the corners on the rooftop plane, as defined by the segmented LiDAR data. Therefore, the mean comparison shows a *Z*-bias between the manually and automatically generated vertices (of almost 60cm, which is an indication of the heights of the fences). The standard deviation in the *Z*-direction reveals good compatibility between the manual and automated procedures.

Table 6.9 Statistics derived from the comparison of two manually generated sets of DBM vertices (second column) as well as the comparison of automatically and manually generated DBM vertices (third column)

	Manual DBM	Automated DBM
No. of vertices	116	78
Mean (X), m	-0.086	-0.040
Mean (Y), m	-0.008	0.003
Mean (Z), m	-0.091	0.553
Std_dev (X), m	± 0.349	± 0.392
Std_dev (Y), m	± 0.364	± 0.407
Std_dev (Z), m	± 0.239	± 0.237
RMSE (X), m	0.357	0.392
RMSE (Y), m	0.362	0.405
RMSE (Z), m	0.255	0.601

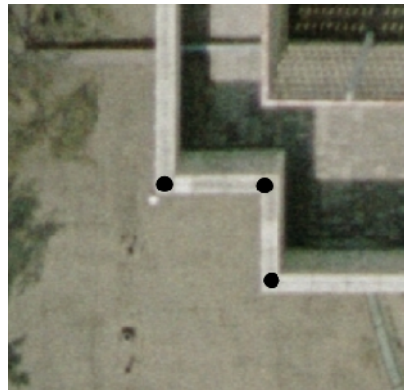


Figure 6.19: A building with protruding fences with manually selected corner points.

6.7 Summary

This chapter presented the experimental results from real LiDAR and imagery data to validate the feasibility and evaluate the performance of the proposed methodologies. First, the datasets utilized in the experiments were described briefly. The datasets include stereo images and LiDAR data over the area of interest including terrain, trees, and buildings (which are complex and connected). Co-registration process provided reliable results with high precision of EOP and without correlation among the parameters. Afterwards, building hypothesis and primitive generation procedures were carried out using LiDAR data only.

The initial boundaries of the building primitives were projected onto the corresponding imagery to verify their quality of the products. The initial boundaries of the building primitives followed overall trend of building shape but did not represent accurate details. This is due to the irregular and sparse nature of LiDAR data. Hence, the boundary refinement process based on the integration of photogrammetric and LiDAR data was conducted to acquire precise boundary segments. Moreover, the occlusion problem where the higher buildings are hiding lower buildings in large scale imagery was resolved by hierarchically projecting the constructed boundary segments of the higher building primitives to the neighbouring lower ones when these primitives share common vertical walls. Additionally, the boundary refinement procedures based on the intersection between the neighbouring primitives and regularization using the initial building boundaries helped to acquire precise boundary segments. The descriptions, values, and justifications for the thresholds used for these procedures were briefly

addressed. The erroneous boundary segments acquired from the automated building reconstruction process were inspected to figure out the reasons. Shadows around the building boundaries and edge lines with uniform textures on both sides caused negative effects on the boundary determination process. The erroneous or missing boundary segments were corrected by manual mono-plotting process. Then, the enhanced DSM (created by adding the derived DBM to the DTM) together with the corresponding imagery were utilized to generate true orthophotos and 3D visualizations. To check the quality improvement, the visualization products after the DSM enhancement were compared with these before the DSM enhancement.

Finally, qualitative and quantitative evaluations were carried out for the experimental results derived from the automated building reconstruction procedures (without involving manual mono-plotting procedure). Qualitative evaluation for the performance of the proposed building reconstruction procedures was conducted by visually inspecting the constructed boundary results for four building primitives with different levels of building complexity. The visual inspection proved that the proposed building reconstruction procedure works well for complex and connected buildings. Quantitative analysis was also carried out based on the completeness, correctness, and RMSE analysis for 40 building primitives which are represented by 291 boundary segments. The correctness and completeness ratio for the study area were 89% and 95%, respectively. Also, the coordinates of the DBM corner points were compared with those derived manually using a photogrammetric reconstruction procedure for assessing the accuracy of the established DBM. The RMSE values for planimetric accuracy were quite

close to those results derived manually. However, discrepancy of vertical accuracies between the automated and manual ways was detected. The reason was that most of the buildings in the study area had fences on their rooftops.

Chapter 7 : Conclusions and Recommendations for Future Work

7.1 Conclusions

Rapid urban growth is one of the important worldwide issues currently, as the United Nations predicted that roughly 62% of the estimated global population will dwell in urban areas in 2030. To successfully control social and environmental situations that might arise from this rapid urbanization, accurate and up-to-date geo-spatial information should be provided to decision makers in various fields. There is, hence, a growing need for tools to assist these decision makers by providing accurate and realistic 3D visualizations of urban environments. Although 3D visualizations are available using well-known tools, such as Google earth, NASA's World Wind, and Microsoft Virtual Earth, their level of accuracy is not high enough for urban planning, urban management, and other applications. For example, the accurate geo-spatial information is essential for sidewalk construction, enforcement of right to light, visibility analysis for military operations, line of sight analysis for telecommunication, and control information for geo-referencing of images from various data sources (e.g., a camera mounted on a Unmanned Aerial Vehicle (UAV), cell phone camera, surveillance camera, etc). To be truly useful for the applications mentioned above, an accurate and realistic 3D visualization of a real-world area should allow a civil engineer or land surveyor to be able to make on-screen measurements from one building corner to another, without having to visit the actual site. For this reason, the aim of the research presented here is to develop a new framework for the accurate reconstruction and visualization of urban environments. The procedures used to reach this goal encountered many difficulties due to the complexity of urban

environments and the nature of the datasets utilized (e.g., the irregularity and sparseness of LiDAR data and the ill-posed matching problem with photogrammetric data). This research provided solutions for these issues and accurate final products. This chapter will summarize the problems that this research encountered, the solutions developed for the problems, and relevant contributions of the research.

To produce accurate visualizations, two main concerns should be considered: 1) the correct relation of LiDAR positional information and imagery spectral information and 2) the completeness of the surface models. As prerequisite steps, quality assurance and quality control procedures were carried out for the photogrammetric and LiDAR data to ensure the high quality of the datasets utilized. Once the quality assurance and control of the photogrammetric and LiDAR data have been conducted, both datasets can be used with confidence for this research. Then, the co-registration of the two datasets was carried out by utilizing the LiDAR data as the source of control for photogrammetric georeferencing, and highly reliable results were attained.

Once the photogrammetric dataset has been aligned to the reference frame of the LiDAR data, the image spectral information and LiDAR positional information from the two datasets are ready to be linked to one another in the true orthophoto generation process. Two angle-based true orthophoto generation methods were proposed to relate the image spectral and LiDAR positional information correctly. The proposed methods overcome problems, such as false visibility and false occlusions that arise from the use of the Z-buffer method. Moreover, these methods do not require the incorporation of the

internal characteristics and attitude of the imaging sensor for visibility analysis. In other words, only the position of the perspective center and the object space (i.e., DSM) are necessary for this analysis without involving any other information related to the image space. In addition, their performance does not depend on the relationship between the DSM cell size and the GSD of the imaging sensor. For 2D visualization, true orthophotos were produced using the angle-based methods. Then, the true orthophotos were draped over the DSM to create a 3D visualization. The degradation in the quality of the products, especially near building boundaries and small features above ground, was reported. Regardless of which true orthophoto generation method is used, the results are affected by the quality of the surface model, in terms of the representation of features. The irregular and sparse nature of LiDAR data leads to a lack of representation of certain features in surface models. Since the degradation in the visualization products occurred mainly along the building boundaries, there was a need to enhance the surface models through the introduction of precise building models.

DBM generation is usually performed in two steps: 1) building detection and 2) building reconstruction. At this stage, the target of this process was buildings with planar rooftops, which are bounded by straight lines. Since elevation data is acquired directly by a LiDAR system, the degree of automation in building detection using this type of data is higher when compared to that using imagery (Brenner, 2005). Hence, building detection was carried out through the manipulation of LiDAR data only. Building hypotheses and primitives (i.e., the individual planar patches constituting each building rooftop) were generated through the building detection process. Building hypothesis and primitive

generation begins with terrain and off-terrain classification of LiDAR data. The proposed angle-based approach for true orthophoto generation was extended to create this procedure. In contrast to the occlusion detection procedure, which focused on the identification of occluded points, the proposed terrain/off-terrain point classification procedure focused on the identification of occluding points (i.e., the points causing the occlusions), which were hypothesized to be off-terrain points. Synthesized projection centers and a tracking procedure were introduced in order to identify occluding points. In addition, false off-terrain hypotheses arising from the noise and high frequency components of the surface (e.g., cliffs and tunnels) were corrected using a statistical filtering procedure. Building hypotheses were then produced by further classifying the off-terrain points as points belonging to planar surfaces and those belonging to rough surfaces. Neighbouring points belonging to planar surfaces were grouped according to their three-dimensional proximity. The resulting groups were then used to identify instances of buildings (i.e., building hypotheses) by considering the area of each group and the heights of the groups relative to neighbouring terrain points. Once the building hypotheses have been generated, a segmentation procedure is applied to each of the building hypotheses to cluster its point cloud into several groups corresponding to the individual planar patches comprising the building (i.e., the building primitives). The segmentation procedure was designed based on a voting scheme. A neighbourhood definition that considers both the three-dimensional relationships among the LiDAR points and the physical shapes of the surfaces was adopted to increase the homogeneity of the derived attributes. After introducing two origins, the magnitudes of the two normal vectors from the origins were utilized as attributes. The level of efficiency, in terms of

computational load, of the process was increased more by introducing two origins than the increase attained by using more than two attributes in other methods. However, the utilization of two origins might lead to ambiguities when points belonging to different planes have the same attribute values. The proposed segmentation method sought to avoid ambiguities by moving the locations of the origins whenever ambiguities arose. After resolving the ambiguity problem, the clustering process was conducted by assessing the local attributes of all the points in the parameter space, together with the proximity of the points in the object space, simultaneously. After this segmentation procedure had been carried out, each cluster represented a building primitive. The initial boundaries of the building primitives were then generated using the points belonging to the primitives by adopting the modified convex hull algorithm. The quality of the initial boundaries produced was investigated by comparing them to the actual building boundaries. The irregular and sparse nature of the LiDAR data led directly to the generation of irregular initial boundaries. Hence, the need for improvement in the quality of the initial boundaries arose at this stage.

The building reconstruction procedure, which refines the initial boundaries of the building primitives, begins by intersecting neighbouring planar patches to represent ridge lines, if any exist. For this scenario, the plane parameters computed through the building primitive generation process and the 3D adjacency analysis of the primitives were utilized to produce precise boundary segments. A different boundary segment refinement procedure, on the other hand, was proposed for use with all the remaining boundary portions for which both LiDAR and photogrammetric data can be utilized. The two

datasets were integrated and the resulting synergistic properties were utilized in the procedure. Warped imagery, a new concept in the integration of LiDAR data and imagery, was introduced instead of using the original imagery. The warped imagery was used to relate the LiDAR data and imagery in one step. This was carried out through the simple projection of the original images onto the corresponding building primitive planes generated using the LiDAR data. This integration eliminated geometric differences between the warped images along the building primitive; hence, the direct comparison of the spectral information in these images was made possible without analyzing the geometric distortions that exist in the original imagery. It is for this reason that this integration is referred to as the object-based integration. Since the target of this research is buildings with planar rooftops, which are bounded by straight lines, straight lines were derived directly from the warped images. The matching process was carried out on the LiDAR plane (i.e., warped image plane) of each building primitive using the straight lines derived. The matching problem (i.e., the ill-posed nature of the image matching problem, particularly for large scale imagery over urban areas) was solved by incorporating the LiDAR data as a constraint in the matching process. The matching process provided precise matched 3D lines. These matched 3D lines were then divided into groups of non-overlapping line segments that were believed to be competing for the same boundary segment of the building primitive in question. Finally, a spectral similarity measure was used to select the precise building boundary segment from the members of each group. At this stage, one should note that this research focuses on urban environments with complex and connected buildings, while utilizing large scale imagery acquired through traditional photogrammetric data acquisition mission (i.e., 20% sidelay

and 60% overlap). Hence, there might be significant occlusions in the imagery. In this case, conjugate features cannot be derived from the occluded areas; the matching process cannot be applied for this case. As a result, portions of the affected building boundary will be missing. A solution for this problem was provided through the projection of the boundary segments constructed for higher building primitives onto lower, neighbouring primitives with shared vertical walls. Even after these three different boundary refinement approaches have been applied, some portions of building boundaries may still be missing. This situation arises when part of a building primitive is hidden by another building primitive in either one or both warped images. In this case, boundary segments corresponding to the missing boundary portions were derived by regularizing the initial boundaries of the building primitives. Then, building reconstruction was finalized by producing closed-polygons using all the derived boundary segments, followed by the simultaneous alignment of all the closed-polygons. So far, an automated boundary refinement procedure has been carried out using LiDAR and image data. For situations in which there is weak image contrast, shadow, and/or uniformity of texture around line segments, the results of the procedure may have missing and/or erroneous boundary segments. To compensate for these situations, a mono-plotting procedure was introduced, in which the operator interactively deletes or adds boundary segments.

Once the building models were acquired through the proposed building reconstruction procedure, the enhanced DSM was generated by combining the corresponding DTM and DBM. To avoid the decrease in quality of the visualization products around small features above ground, it was decided to add the DBM to a DTM

instead of to the original DSM. 2D and 3D visualizations were produced by relating the spectral information from the corresponding imagery and the positional information from the enhanced DSM.

To verify the performance of the proposed methodology, qualitative and quantitative analyses were then carried out for the experimental results derived through the automated building reconstruction procedures (without involving the manual mono-plotting procedure). Qualitative analysis was performed by visually inspecting the constructed boundary results for four building primitives with different levels of building complexity. The visual inspection proved that the proposed building reconstruction procedure performs well for complex and connected buildings. Quantitative analysis was also carried out based on the completeness, correctness, and RMSE analysis derived for 40 building primitives, which were represented by 291 boundary segments. The correctness and completeness ratios for the study area were 89% and 95%, respectively. In addition, the coordinates of the DBM corner points were compared with those derived manually using a photogrammetric reconstruction procedure to assess the accuracy of the established DBM. The RMSE analysis found that the DBM produced was quite close to the results obtained manually. The qualitative evaluation of the final visualization products also showed that this research provided more realistic and more appealing visualization products for buildings and small features above ground, respectively. In summary, this research provided a new framework for the accurate reconstruction and visualization of urban environments. The major contributions of this research are summarized as follows:

Contribution 1:

This research takes advantage of the integration of photogrammetric and LiDAR data, and an object-based integration process was proposed. By utilizing warped imagery derived through the object-based integration process, the image matching problem was resolved, since the incorporated LiDAR data worked as a constraint. In addition, spectral similarity transitions over the matched line segments extracted from the warped imagery were investigated to select precise boundary segments.

Contribution 2:

The hierarchical projection approach was proposed to reconstruct boundary segments in the occluded areas. This approach successfully worked for the building primitives which share a vertical wall but have different elevations. The reconstruction procedure was performed by projecting the boundary segments constructed for higher building primitives onto the lower and neighbouring ones.

Contribution 3:

Two angle-based true orthophoto generation methods were developed to overcome problems, such as false visibility and false occlusions that arise when the current, commonly used methodology is employed. These methods do not require the incorporation of the internal characteristics and attitude of the imaging sensor for visibility analysis. Furthermore, the performance of the proposed methods does not depend on the relationship between the DSM cell size and the GSD of the imaging sensor.

Contribution 4:

A terrain and off-terrain LiDAR point classification procedure was developed by extending the angle-based occlusion detection approach, which was utilized for true orthophoto generation. For the segmentation procedure, which is based on a voting scheme, two attributes derived from two origins were introduced to increase the level of efficiency, in terms of computational load. Reliable segmentation results were obtained by assessing the similarity of all point attributes in the parameter space, and the proximity of the points in the object space, simultaneously.

7.2 Recommendations for Future Work

Recommendations for future work include the alleviation of the effects of shadow on the selection of precise boundary segments. In other words, more investigation into the removal of shadow effects caused by fences around building boundaries should be conducted. On the other hand, the precise boundary segment selection procedure does not work properly when there are uniform textures on both sides of a boundary segment. Future work should investigate solutions for this problem. The areas that need to be edited manually by an operator should also be investigated further to improve the correctness and completeness of the DBM products. Also, when the building reconstruction procedure is expanded to incorporate more than two images, the matching and the precise boundary selection procedures will have to be modified to handle multiple images. The warped imagery generation procedure can also be extended beyond the use of aerial photos to utilize satellite imagery.

Another approach, based on region growing in the warped imagery using colour segmentation, will be considered here to solve the fence problem and the non-matching problem. Figure 7.1 illustrates the concept of roof region detection based on region growing using colour segmentation. Each of the warped images generated over a building with high fences on its rooftop will contain rooftop areas that are partially hidden because of the fences. In this case, the full rooftop area can be acquired by aggregating the region growing results obtained from the two warped images. As for visualization, the missing texture on the walls should be recovered by utilizing oblique/terrestrial images or artificial texturing. Also, the addition of street furniture will improve the quality of the 3D visualization, especially when small features such as cars, trees, and light poles are added (see Figure 7.2). The proposed research focused on planar rooftops bounded by straight line segments. This approach will be extended to manipulate non-straight lines and/or non-planar surfaces. More testing and evaluation will be conducted with various datasets.

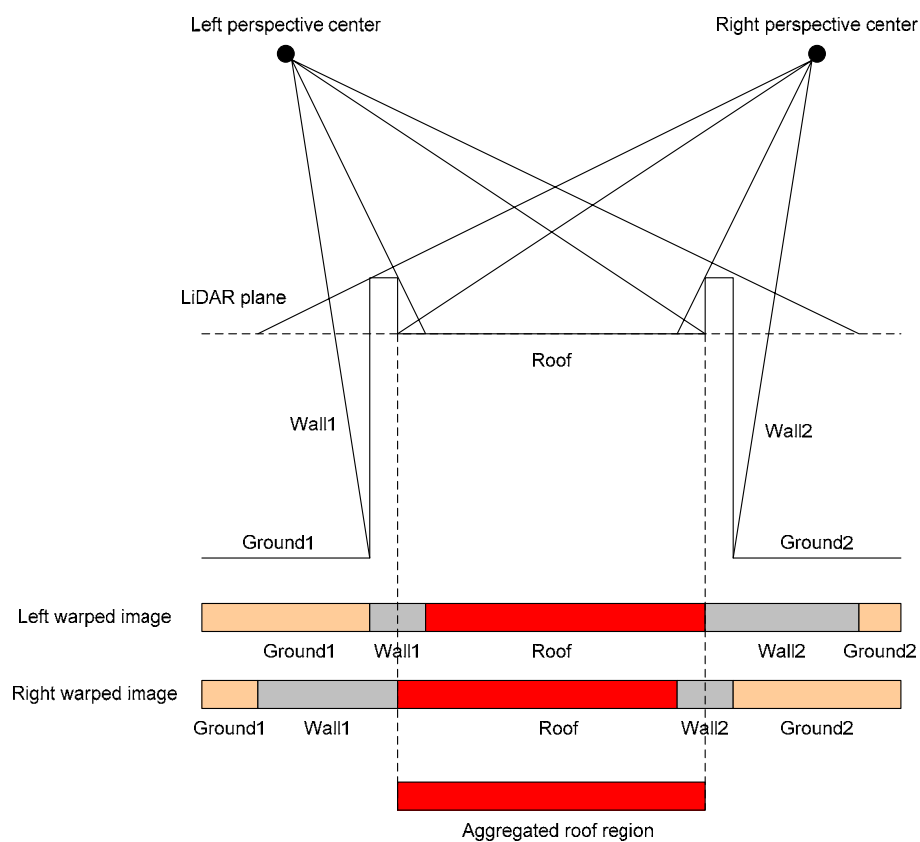


Figure 7.1: The concept of roof region detection based on region growing using colour segmentation.



Figure 7.2: Samples of the street furniture available in ArcGIS.

References

- Ackermann, F., 1999. Airborne laser scanning—present status and future expectations. *ISPRS Journal of Photogrammetry and Remote Sensing*, 54: 64–67.
- Akel, N. A., S. Filin, and Y. Doytsher, 2007. Orthogonal polynomials supported by region growing segmentation for the extraction of terrain from LiDAR data, *Photogrammetric Engineering and Remote Sensing*, 73(11): 1253– 1266
- Al-Durgham, M. M., 2007. Alternative Methodologies for the Quality Control of LiDAR Systems. Thesis UCGE Reports Number 20259, University of Calgary, AB, Canada.
- Alharthy, A., 2003. Airborne Laser Scanning: System Evaluation and Building Extraction. Ph.D. dissertation. Purdue University.
- Amhar, F. and R. Ecker, 1996. An integrated solution for the problems of 3D man-made objects in digital orthophotos, *International Archives of Photogrammetry and Remote Sensing*, 31(Part B4): 84-89.
- Amhar, F., J. Josef, and C. Ries, 1998. The generation of true orthophotos using a 3D building model in conjunction with a conventional *DTM*, *International Archives of Photogrammetry and Remote Sensing*, 32(Part 4): 16-22.
- Axelsson, P., 1999. Processing of laser scanner data – algorithms and applications. *ISPRS Journal of Photogrammetry and Remote Sensing*, 54(2-3): 138-147.
- Axelsson, P., 2000. DEM generation from laser scanner data using adaptive TIN models, *International Archives of the Photogrammetry and Remote Sensing*, 33 (B4/1): 110– 117.
- Baillard, C., and A. Zisserman, 1999. Automatic line matching and 3D reconstruction of buildings from multiple views, *International Archives of Photogrammetry and Remote Sensing*, 32(Part 3-2W5).

- Baltsavias, E. P., Mason, S. O., Stallmann, D., 1995. Use of DTMs/DSMs and orthoimages to support building extraction. http://e-collection.ethbib.ethz.ch/ecol-pool/inkonf/inkonf_81.pdf (accessed April 2008).
- Baltsavias, E., 1999. Airborne laser scanning: existing systems and firms and other resources, *ISPRS Journal of Photogrammetry and Remote Sensing*, 54(2-3), pp. 164-198.
- Besl, P.J. and Jain, R.C., 1998. Segmentation Through Variable Order Surface Fitting. *IEEE Transactionson Pattern Analysis and Machine Intelligence*, 10(2):167-192.
- Brenner, C., 2005. Building reconstruction from images and laser scanning, *International Journal of Applied Earth Observation and Geoinformation*, 6: 187-198.
- Briese, C., N. Pfeifer, and P. Dorninger, 2002. Applications of the robust interpolation for DTM determination, *International Archives of Photogrammetry and Remote Sensing*, 34(3A): 55–61.
- Brovelli, M. A., M. Cannata, and U.M. Longoni, 2002. Managing and processing LiDAR data within GRASS. *Proceedings of the Open source GIS - GRASS Users Conference*, 11 – 13 September. Trento, Italy, pp. 1-29.
- Canny, J., 1986. A computational approach to edge detection. *IEEE Transactions on Pattern Analysis and Machine Intelligence*, 8, pp. 679–690.
- Catmull, E., 1974. A Subdivision Algorithm for Computer Display of Curved Surfaces, Ph.D. dissertation, Department of Computer Science, University of Utah, Salt lake city, Utah.
- Charaniya, A. P., 2005. 3D Urban Reconstruction from Aerial LiDAR data. <http://www.soe.ucsc.edu/~amin/research/proposal.pdf> (accessed April 2008).
- Chen, L., T. Teo, J. Rau J. Liu and W. Hsu, 2005. Building reconstruction from LiDAR data and aerial imagery, *Geoscience and Remote Sensing Symposium*, 4: 2846-2849.

- Chen, Liang-Chien, Tee-Ann Teo, Yi-Chen Shao, Yen-Chung Lai, Jiann-Yeou Rau, 2004. Fusion of LiDAR data and optical imagery for building modeling, *International Archives of Photogrammetry and Remote Sensing*, 35(B4): 732-737.
- Cramer, M., Stallmann, D., and Haala, N., 2000. Direct Georeferencing Using GPS/Inertial Exterior Orientations for Photogrammetric Applications, *International Archives of Photogrammetry and Remote Sensing*, 33(B3): 198-205.
- Dony, R.D., and S. Wesolkowski, 1999. Edge detection on colour images using RGB vector angles, *Proceedings of the 1999 Canadian Conference on Electrical and Computer Engineering*, Edmonton, Alberta, Canada, pp. 687-692.
- Douglas, D.H., and T.K. Peucker, 1973. Algorithms for the reductions of the number of points required to represent a digitized line or its caricature, *The Canadian Cartographer* 10(2), pp. 112-122.
- Elaksher, A. F., and Bethel., J. S., 2002. Reconstructing 3D buildings from Lidar data. *International Archives of the Photogrammetry and Remote Sensing*, Vol. XXXIV, part 3A/B, ISSN 1682-1750, pp102-107.
- Elmqvist, M., E. Jungert, F. Lantz, A. Persson, and U. Soderman, 2001. Terrain modelling and analysis using laser scanner data, *International Archives of the Photogrammetry and Remote Sensing*, 34 (3/W4): 219– 227.
- Faig, W. and T. Widmer, 2000. Automatic building extraction from aerial images, *Proc. Of IAPRS*, Vol.33, B7, Amsterdam, Netherlands, pp.1708-1715.
- Filin, S., 2002. Surface clustering from airborne laser scanning data. In: *ISPRS Commission III, Symposium 2002* September 9 - 13, 2002, Graz, Austria, pp. A– 119 ff (6 pages).
- Filin, S., Pfeifer, N., 2005. Neighborhood Systems for Airborne Laser Data. *Photogrammetric Engineering and Remote Sensing*, 71(6): 743-755.

- Filin, S., Pfeifer, N., 2006. Segmentation of airborne laser scanning data using a slope adaptive neighbourhood. *ISPRS Journal of Photogrammetry and Remote Sensing*, 60: 71–80.
- Förstner, W., 1999. 3D-City Models: Automatic and semi-automatic acquisition methods. <http://www.ifp.uni-stuttgart.de/publications/phowo99/foerstner.pdf>. (accessed 1 Apr. 2008).
- Ghanma, M., 2006. Integration of Photogrammetry and LIDAR, Ph.D. thesis: University of Calgary, Calgary, Canada.
- Grün, A., Dan, H., 1997. TOBAGO – a topology builder for the automated generation of building models. In: Grün, A., Baltsavias, E., Henricsson, O. (Eds.), *Automatic Extraction of Man-Made Objects from Aerial and Space Images (II)*. Birkhauser, Basel, pp. 149–160.
- Grün, A., Wang, X., 1998. CC-modeler: a topology generator for 3- D city models. In: Fritsch, D., English, M., Sester, M. (Eds.), *International Archives of Photogrammetry and Remote Sensing*, 32(4): 188–196. Stuttgart.
- Haala, N. and Hahn, M., 1995. Data fusion for the detection and reconstruction of buildings. In *Automatic Extraction of Man-Made Objects from Aerial and Space Images*.
- Haala, N., C. Brenner, and K. Anders, 1998. 3D Urban GIS from laser altimeter and 2D map data, *International Archives of Photogrammetry and Remote Sensing*, 32: 339-346.
- Habib, A., and T. Schenk, 1999. New approach for matching surfaces from laser scanners and optical sensors, *International Archives of Photogrammetry and Remote Sensing*, 32: 55–61.
- Habib, A., Quackenbush, P., Lay, J., Wong, C., and Al-Durgham, M., 2006a. Camera calibration and stability analysis of medium-format digital cameras. *Proceedings of SPIE – 6312, Applications of Digital Image Processing XXIX*, 11 pages.

- Habib, A., Shin, S., Kim, C., Al-Durgham, M., 2006b. Integration of Photogrammetric and LIDAR Data in a Multi-Primitive Triangulation Environment. *International Workshop on 3D Geo-Information*, Kuala Lumpur, Malaysia, August 7 – 8, 2006, 17 pages, Un-paginated CD Rom.
- Habib, A., Bang, K., Aldelgawy, M., and Shin, S., 2007. Integration of Photogrammetric and LiDAR Data in a Multi-primitive Triangulation Procedure, *Proceedings of the ASPRS 2007*, Tampa, Florida.
- Habib, A., Bang, K., Kersting, A., Lee, D., 2008a. Error Budget of LiDAR Systems and Quality Control of the Derived Data. *Photogrammetric Engineering and Remote Sensing*, Accepted for Publication.
- Habib, A., Y. Chang, and D. Lee, 2008b. Occlusion-based methodology for the classification of LiDAR data, *Photogrammetric Engineering and Remote Sensing*, Accepted for publication.
- Habib, A., Jarvis, A., Kersting, A., Alghamdi, Y., 2008c. Comparative Analysis of Georeferencing Procedures Using Various Sources of Control Data, *XXIst ISPRS proceedings*, 3-11 Jul, 2008, Beijing, China, 27: 1147 – 1152.
- Haugerud, R.A., and D.J. Harding, 2001. Some algorithms for virtual deforestation (VDF) of LiDAR topographic survey data, *International Archives of Photogrammetry and Remote Sensing*, 34 (3/W4): 211 –218.
- Henricsson, O., Bignone, F., Willuhn, W., Ade, F., Kubler, O., Baltasavias, E., Mason, S. and Gruen A., 1996. Project AMOBE: Strategies, current Status and Future Work. *In Proceedings of 18th ISPRS Congress*, Vienna, Austria. B3, pp. 321-330.
- Heipke, C., Mayer, H., Wiedemann, C. and Jamet, O., 1997. Evaluation of Automatic Road Extraction. In: *International Archives of Photogrammetry and Remote Sensing*, Vol.32, pp. 47-56.

- Hoover, A., Jean-Baptiste, G., Jiang, X., Flynn, P.J., Bunke, H., Goldgof, D.B., Bowyer, K., Eggert, D.W., Fitzgibbon, A., Fisher, R.B., 1996. An Experimental Comparison of Range Image Segmentation Algorithms. *IEEE Transactions on Pattern Analysis and Machine Intelligence* 18 (7): 673-689.
- Hough, P.V.C., 1962. Methods and Means for Recognizing Complex Patterns, U.S. Patent 3,069,654.
- Hu, J., S. You, U. Neumann, and K. Park, 2004. Building modeling from LiDAR and aerial imagery, *ASPRS'04*, Denver, Colorado, USA.
- Huertas, A. and Nevatia, R., 1988. Detecting Buildings in Aerial Images. *Computer Vision, Graphics, and Image Processing*, 41(2), pp. 131-152.
- Jacobsen, K. and P. Lohmann, 2003. Segmented filtering of laser scanner DSMs, *International Archives of Photogrammetry and Remote Sensing*, 34 (3/W13).
- Jarvis, R. A., 1977. Computing the shape hull of points in the plane, *Proceedings of IEEE Computer Society Conference Pattern Recognition and Image Process*, pp.231-261.
- Kilian, J., N. Haala, and M. English, 1996. Capture and evaluation of airborne laser scanner data. *International Archives of Photogrammetry and Remote Sensing*, 31(B3), pp. 383-388.
- Kim C., Habib A., and Mrstik P., 2007. New Approach for Planar Patch Segmentation using Airborne Laser Data. *Proceedings of the ASPRS 2007*, Tampa, Florida.
- Kim, Z., A. Huertas, and R. Nevatia, 2001. Automatic description of buildings with complex rooftops from multiple images, *Computer Vision and Pattern Recognition*, Kauai, pp. 272-279.
- Konecny, G., 1979. Methods and possibilities for digital differential rectification. *Photogrammetric Engineering and Remote Sensing*, 45(6): 727-734.

- Kraus, K. and N. Pfeifer, 1998. Determination of terrain models in wooded areas with airborne laser scanner data, *ISPRS Journal of Photogrammetry and Remote Sensing*, 53:193–203.
- Kraus, K. and N. Pfeifer, 2001. Advanced DTM generation from LiDAR data, *International Archives of Photogrammetry and Remote Sensing*, 34(3/W4): 23–30.
- Kuzmin, P., A. Korytnik, and O. Long, 2004. Polygon-based true orthophoto generation, *XXth ISPRS Congress*, 12-23 July, Istanbul, pp. 529-531.
- Lee, D., K. Lee, and S. Lee, 2008. Fusion of LiDAR and imagery for reliable building extraction, *Photogrammetric Engineering and Remote Sensing*, 74(2): 215-225.
- Lee, I., Schenk, T. 2001. Autonomous extraction of planar surfaces from airborne laserscanning data, *Proc. ASPRS annual conference*, St. Louis, MO, USA.
- Lin Ch., Huertas, A., and Nevatia, R., 1995. Detection of buildings from monocular images. In *Automatic Extraction of Man-Made Objects from Aerial and Space Images*.
- Ma, R., 2004. Building Model Reconstruction from LIDAR Data and Aerial Photographs, Ph.D. dissertation, The Ohio State University.
- Maas, H. and G. Vosselman, 1999. Two algorithms for extracting building models from raw laser altimetry data, *ISPRS Journal of Photogrammetry and Remote Sensing*, 54: 153 – 163.
- Maas, H.G., 1999. The potential of height texture measures for the segmentation of airborne laserscanner data. In: *Proceedings of the Fourth International Airborne Remote Sensing Conference*, Ottawa, Canada. pp. 154- 161.
- Masaharu, H., and K. Ohtsubo, 2002. A Filtering Method of Airborne Laser Scanner Data for Complex Terrain, *International Archives of the Photogrammetry, Remote Sensing and Spatial Information Sciences, Commission III*, 09–13, September, Graz, Austria, 34 (3B): 165–169.

- McGlone, J.Ch. and Shufelt, J. A., 1994. Projective and object space geometry for monocular building extraction. *Proceedings of IEEE Computer Society Conference on Computer Vision and Pattern Recognition*, pp. 54 -61.
- McIntosh, K. and Krupnik, A., 2002. Integration of laser-derived DSMs and matched image edges for generating an accurate surface model, *ISPRS Journal of Photogrammetry and Remote Sensing*, 56: 167-176.
- Mikhail, E., 2001. Introduction to modern photogrammetry, John Wiley & Sons, Inc., New York, 479p.
- Nevatia, R., Lin, Ch., and Huertas, A., 1997. A system for building detection from aerial images. In Automatic Extraction of Man-Made Objects from Aerial and Space Images (II).
- Noronha, S., Nevatia, R., 2001. Detection and modeling of buildings from multiple aerial images. *IEEE Transactions on Pattern Analysis and Machine Intelligence*, 23 (5), pp. 501– 518.
- Novak, K. 1992. Rectification of digital imagery, *Photogrammetric Engineering and Remote Sensing*, 58(3): 339-344.
- Pfeifer, N., P. Stadler, and C. Briese, 2001. Derivation of digital terrain models in the SCOP++ environment, *Proceedings of OEEPE Workshop on Airborne Laserscanning and Interferometric SAR for Detailed Digital Terrain Models*, 1–3 March, Stockholm, Sweden.
http://www.ipf.tuwien.ac.at/publications/np_stockholm.pdf.
- Rau, J., N. Chen, and L. Chen, 2000. Hidden compensation and shadow enhancement for true orthophoto Generation, *Proceedings of Asian Conference on Remote Sensing 2000*, 4-8 December, Taipei, unpaginated CD-ROM.
- Rau, J., N. Chen, and L. Chen, 2002. True orthophoto generation of built-up areas using multi-view images, *Photogrammetric Engineering and Remote Sensing*, 68(6): 581-588.

- Roggero, M. 2001. Airborne laser scanning: clustering in raw data, *International Archives of the Photogrammetry and Remote Sensing*, 34 (3/W4): 227– 232.
- Rottensteiner, F., and Ch. Briese, 2002. A new method for building extraction in urban areas from high-resolution LiDAR data, *International Archives of Photogrammetry and Remote Sensing*, 34(3A): 295-301.
- Roux, M., McKeown, D. M., 1994. Feature matching for building extraction from multiple views. In: *Proceedings of the 1994 IEEE Conference on Computer Vision and Pattern Recognition*. Seattle, WA.
- Sampath, A. and J. Shan, 2007. Building boundary tracing and regularization from airborne LiDAR point clouds, *Photogrammetric Engineering and Remote Sensing*, 73(7): 805-812.
- Schenk, T., and B. Csatho, 2002. Fusion of LIDAR data and aerial imagery for a more complete surface description. In: *IAPRSIS 32(3A)*: 310.
- Seo, S., 2003. Model Based Automatic Building Extraction from LIDAR and Aerial Imagery, Ph.D. dissertation, The Ohio State University.
- Sheng, Y., P. Gong, and G. Biging, 2003. True orthoimage production for forested areas from large-scale aerial photographs, *Photogrammetric Engineering and Remote Sensing*, 69(3): 259-266.
- Sithole, G., and G. Vosselman, 2004. Experimental comparison of filter algorithms for bare-earth extraction from airborne laser scanning point clouds, *ISPRS Journal of Photogrammetry and Remote Sensing*, 59 (1-2): 85–101.
- Skarlatos, D., 1999. Orthophotograph production in urban Areas, *Photogrammetric Record*, 16(94): 643-650.
- Sohn, G., and I. Dowman, 2002. Terrain surface reconstruction by the use of tetrahedron model with the MDL Criterion, *International Archives of the Photogrammetry and Remote Sensing*, 34 (3A): 336– 344.

- Sutherland, I., R. Sproull, and R. Schumacker, 1974. A characterization of ten hidden-surface algorithms, *ACM Computing Surveys*, 6:1–55.
- Suveg, I., Vosselman, G., 2004. Reconstruction of 3D building models from aerial images and maps. *ISPRS Journal of Photogrammetry and Remote Sensing*, 58, pp. 202–224.
- Vosselman, G, 2000. Slope based filtering of laser altimetry data, *International Archives of Photogrammetry and Remote Sensing*, 33(B3): 935–942.
- Vosselman, G. and S. Dijkman, 2001. 3D building model reconstruction from point cloud and ground plans, <http://www.isprs.org/commission3/annapolis/pdf/Vosselman.pdf> (accessed April 2008).
- Vosselman, G., 1999. Building reconstruction using planar faces in very high density height data. *In ISPRS Conference on Automatic Extraction of GIS Objects from Digital Imagery*, Munich, Germany.
- Vosselman, G., 2004. Strip Offset Estimation Using Linear Features, <http://www.itc.nl/personal/vosselman/papers/vosselman2002.columbus.pdf> (accessed 15 Nov. 2007).
- Vosselman, G., Gorte, B.G.H., Sithole, G., Rabbani, T., 2004. Recognising structure in laser scanner point clouds. *International Archives of Photogrammetry and Remote Sensing*, 36(8/W2): 33-38.B32.
- Wack, R., and A. Wimmer, 2002. Digital terrain models from airborne laser scanner data—a grid based approach, *International Archives of Photogrammetry and Remote Sensing*, 34 (3B): 293–296.
- Wang, Y., S. Schultz, and F. Giuffrida, 2008. Pictometry’s proprietary airborne digital image system and its application in 3D city modeling, *International Archives of Photogrammetry and Remote Sensing*, Vol. XXXVII, Part B1, Beijing, pp.1065-1070.

- Wang, Zh., 1999. Surface reconstruction for object recognition, Ph.D. dissertation, The Ohio State University, 1999.
- Weidner, U., 1996. An approach to building extraction from digital surface models. *Proc. 18th ISPRS Congress, Wien. IAPRS*, 31(Part B3): 924–929.
- Zhang, K., S.C. Cheng, D. Whitman, M. L. Shyu, J. Yan, and C. Zhang, 2003. A progressive morphological filter for removing non-ground measurements from airborne LiDAR data, *IEEE Transactions on Geoscience and Remote Sensing*, 41(4):872–882.
- Zhou, G., 2005. Urban Large-scale Orthoimages Standard for National Orthophoto Program, *XXVth IEEE International Geoscience and Remote Sensing Symposium Proceedings*, 25-29 July, Seoul, Korea, unpaginated CD-ROM.
- Zuxun, Z., Jun, W., Jianqing, Z., 2004. A method for straight line extraction based on line space, *Geomatics and Information Science of Wuhan University*, 29(3): 189-194.